

**Proceedings of Short Term-Stay Program of Shizuoka University
(Shizuoka University and Changwon National University)**



From January 5, 2012 to January 11, 2012

Faculty of Engineering, Shizuoka University

(Hamamatsu Campus)

Proceedings creator & Japanese-side student leader: Yasuyuki Nagami

1st-year master degree student, Saito Laboratory, Shizuoka University

Korean-side student leader: Jong-Min Kim

3rd-year Bachelor's degree student, Shin Laboratory, Changwon National University

Contents

- 1. Purposes of the Short Term-Stay Program of Shizuoka University
..... 2

- 2. Agenda of the Short Term-Stay at Shizuoka University
..... 3

- 3. List of Participants
..... 5

- 4. Report on Short Term-Stay Program of Shizuoka University
..... 7

- 5. Productive international exchange between Shizuoka University and Changwon National
University
..... 15

- 6. Proceedings of Japanese Students Technical Program
..... 17

- 7. Proceedings of Korean Students Presentation
..... 58

- 8. Acknowledgment
..... 94

1. Purposes of the Short Term-Stay Program of Shizuoka University

This project is promoted by Japan Student Services Organization (JSSO). The main purpose is a student-based international exchange between a laboratory and a laboratory. In order to achieve the productive international exchange for both sides' students, the preparation and the progression managed by the students.

8th January, DAY 4

a.m. Saito Laboratory's research presentation (5 students)

Launch

p.m. Saito Laboratory's research presentation (2 students)

Korea side students' report creating

9th January, DAY 5

a.m. Shopping at the huge shopping mall

Launch

p.m. Shopping at the huge shopping mall

Japan VS Korea bowling game

Farewell party (Korean-style grilled beef Restaurant)

10th January, DAY 6

Traveling:

Hamamatsu Station → (Shinkansen) → Shin-Osaka Station

Tour in Kyoto

11th January, DAY 7

Tour in Kajishima Laboratory (Graduate School of Engineering, Osaka University)

Traveling:

Kansai International Airport → (Airplane) → Busan → (Bus) → Changwon

3. List of Participants

Guest: Shin Laboratory, Changwon National University, Korea

Name	Status	Affiliation
Byeongrog Shin	Professor	Department of Mechanical Engineering Changwon National University
Kyeongrock Jang	3rd-year Bachelor's degree student	
Jongmin Kim		
Heesung Lee		
Chunggi Moon		
Jeonghoon Song		

Host: Saito Laboratory, Shizuoka University, Japan

Name	Status	Affiliation
Takayuki Saito	Professor	Graduate School of Science and technology, Shizuoka University
Rintarou Tachibana	2nd-year Master's degree student	Graduate School of Engineering, Shizuoka University
Masahiko Toriu	1st-year Master's degree student	
Yasuyuki Nagami		
Yuki Mizushima		
Taikan Mori		
Masahiro Yamada		
Ryosuke Motoyoshi	4th-year Bachelor's degree student	Faculty of Engineering, Shizuoka University
Masanobu Tsukamoto		
Yuta Nakamura		
Hajime Furuichi		
Daisuke Shinohara	3rd-year Bachelor's degree student	
Yuki Masumoto		

Other Participants

Name: Keisuke Noba

Affiliation: Fukuta Laboratory, Faculty of Engineering, Shizuoka University, Japan

Name: Kazuhide Matsushita

Affiliation: Sanada Laboratory, Faculty of Engineering, Shizuoka University, Japan

Name: Takuya Tanaka

Affiliation: Sanada Laboratory, Faculty of Engineering, Shizuoka University, Japan

Name: Shintaro Hiragi

Affiliation: Shizuoka University Motors, Shizuoka University, Japan

4. Report on Short Term-Stay Program of Shizuoka University



Opening ceremony: Prof. Saito's speech



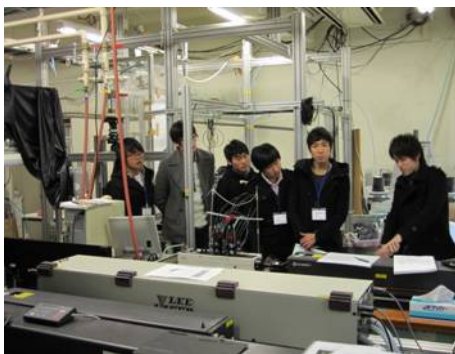
Opening ceremony: Prof. Shin's speech



Korean student self-introduction



Japanese student self-introduction



Tour in Saito Laboratory (4th floor)



Tour in Saito Laboratory (5th floor)



Tour of Shizuoka University Motors



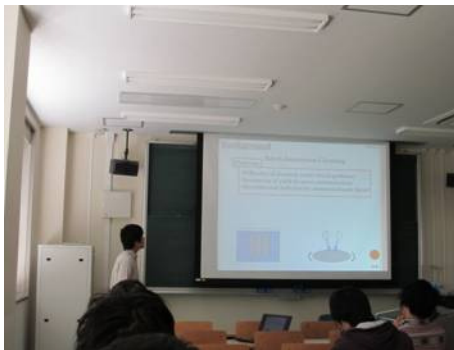
Tour of Shizuoka University Motors



Korean student presentation (Shin Lab.)



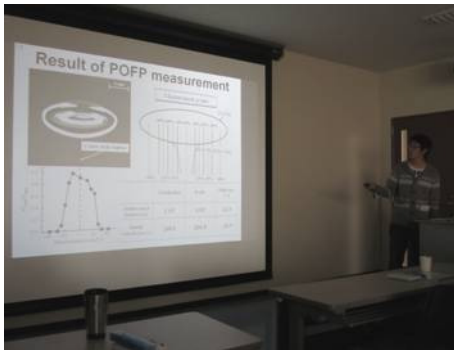
Korean student presentation (Shin Lab.)



Japanese student presentation (Sanada Lab.)



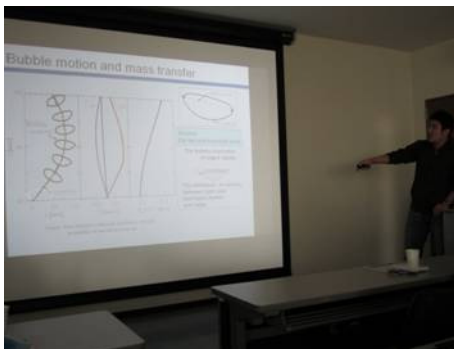
Japanese student presentation (Fukuta Lab.)



Japanese student presentation (Saito Lab.)



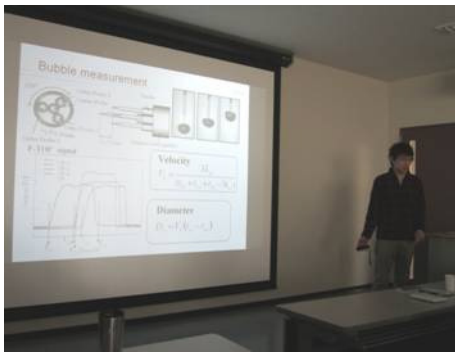
Japanese student presentation (Saito Lab.)



Japanese student presentation (Saito Lab.)



Japanese student presentation (Saito Lab.)



Japanese student presentation (Saito Lab.)



Japanese student presentation (Saito Lab.)



Free talks during coffee break



Korean student report creating



Japanese-Korean mixed bowling game



Japanese select team VS Korean select team



Farewell party
(Korean-style grilled beef Restaurant)

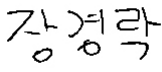


Farewell party
(Korean-style grilled beef Restaurant)

Report 1

Date(D.M.Y) 8th Jan, 2012

Name Jang Kyoungrock

Signature 

University Changwon National University

Country Korea

I went to Shizuoka University in 5 January 2012. I was surprised at Japanese culture. Because Shizuoka University's student(Nagami) and professor(Saito) went early at Station.

And Nagami bring to our hotel. So i think to kind japanese.

Next day, we went to Shizuoka University with Nagami. And we reason about Saito lab.

We was very surprised to laboratory's scale. For example, each student looked to specialist, laboratory had expensive device(high speed video camera, HPTS ets) and very clean in university. Saito's lab researched about bubble motion and variety optical fiber probes (OFP).

It's very interested in me. Because my lab research about fluid mechanics.

We went to hanabasi station for welcome party. We ate meat and Sake. It was similiary to Korea's Soju. We broken up at PM. 8.

I thought similar theme but many element is different. So it's a little diffcult that Shizuoka university's student say about bubble to me.

And our laboratoty's student say about vertical and horizontal axis wind turbine and Magus effect in presentation. Japanese student ask about our theme. It was very thanks.

This course is very beneficial to us. This course is Japan-Korea International Exchange Program. We was good communicatation Though main language was English. Sometime communication was hard. Because japaness used vocabulary is differnt in Korea.

I hope to get the more information about bubble. For example, how to make OFP, measuring bubble's velocity and motion. I know why Japanese education is high quality.

I'm pleased to make new friend. I want to get in touch with Shizuoka university's student.

Thang you..

Report 2

Date(D.M.Y) 8th Jan, 2012

Name KIM JONGMIN

Signature 

University Changwon national University

Country Korea

I write it classify by subject.

future development of the research : I think subject. beforehand we are plan ahead that 'student exchange support program' in detailed. of course, from this program, we are make preparations arrangement. but we are only prepare that it. that is ppt, announcement data. then next time, I hope that. that is actually experimentation accomplishment. of course this present also very interest. in conclusion, if it is possible, that is a help to me.

understanding Japanese culture : In this time, learned to various Japanese culture. ordinary times, I'm very interested in Japanese culture. for instance, the first day in dining together, new food culture come in contact. specially each pay a charge pay it. that is food charge. of course I know little Japanese culture. and this part is originality. in conclusion, each country has merits and faults, important point is comprehend it. that is diversity each culture.

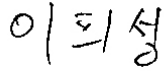
importance foreign study : 'student exchange support program' on the way, Naver had I realized my ignorance more keenly than at this time. I did not need foreign language in the Korea. But That's needed immediately in this place. because to according to circumstances, I must express my intention clearly. Result in, I know from learn by experience. that is 'importance foreign study'

I would like to get in touch with between Changwon National University and Shizuoka National University.

Report 3

Date(D.M.Y) 8th Jan, 2012

Name LEE HEE SUNG

Signature 

University Changwon National University

Country Korea

Thank you for invite Shizuoka university and i`m happy participate in Korea and Japan exchanged program and cultural and scholarship exchange between Korea and Japan

I heard Shizuoka University is very excellent university and top level so i`m a glory

Our laboratory is computational fluid dynamic engineering

Our lab studied wind turbine the other side Saito` lab studied (I think) bubbles, optical fiber probe then different subject between Shin lab and Saito lab thus scholarship exchange between Shin lab and Saito lab is very important and helpful

Saito laboratory are studied very interesting but i`m felt a little difficult so i`m many learned

So Thank you for giving me a chance the listening the presentation the Saito laboratory

Saito lab has very expensive experiment equipment so we just laboratory tour time is very interesting and exciting

Moreover we obtain English speech, listening ability during the get ready presentation

I think this era is international relationship is very important so Korea and Japan exchanged program is very important thus I hope this program is maintenance

I am heard and watching just Japan culture from a television broadcast and comic books and movie but this program through obtain directly experience so i`m delightful

Japan and Korea cultural have some similarity also food

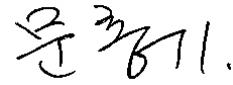
I am hope the this program is more extension and we would like to get in touch with between Changwon National University and Shizuoka National University .

Report 4

Date(D.M.Y) 8th Jan, 2012

Name Moon Chung Gi

Signature



University Changwon National University

Country Korea

Thank you for invite me in Shizuoka university.

I travel Japan in first my life. I saw many different culture, food, house, shop....

I impress the food because Korea food similar. And Japan is very clean street, toilet...

This program is studied good culture in Japan.

We get through discussion in Shizuoka University of professor saito laboratory student.

They present subject in make use of Bubble. I know that Bubble is development possibility.

And I realize that basic theory fluid dynamics. And I see vary experiment equip in professor Saito laboratory. This equip is interested and novelty. Specially pipe cut equip is best Small pipe see through telescope and the combination two pipe is very delicacy.

My English ability is nice the better friendship in Shizuoka University students. It leaves has something to be desired because communication is not very well.

And thank you for giving me a chance the listening the presentation the professor Saito Laboratory.

If my Return to korea very hard study English. I hope japans friend better than friendship.

Get in touch with between Cangwon National University and Shizuoka University

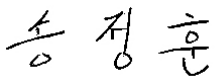
I hope see we again.

Thank you.

Report 5

Date(D.M.Y) 8th Jan, 2012

Name Song Jeong Hoon

Signature 

University Changwon National University

Country Korea

first of all , thank you for granting me Shizuoka university .

I am very interesting in Japanese culture. During the 5days , I am very impressed by Japanese students research and citizen`s ceremony. For examples , a city is very clear and people is kindhearted. Specially Saito`s lab people is very kind and enthusiastic.

Their research is professional. Such as s-top , t-top is rare information . I have not seen ever korea. This opportunity is very important experience. Also I realize necessity about importance of foreign study. This opportunity is very rare, but I realize that Cultural interchange between korea and Japan is very important. After this cultural interchange,if we enlarge cultural interchange between Korea and Japan , So many advantage is existed.

Their experiment equipment is very expensive I have not seen that in Korea.

I will tell Korean that these sensation , Japanese culture , fluid dynamics study, and many others. In order to development in Korea.

Thank you for valuable experience for us. Taking this opportunity ,We would like to get in touch with between Changwon National University and Shizuoka Natiouniversity.

In order to each other`s development,I think that each other`s continuous relationship is very important. So ,after this chance ,we must get in touch with each other.

And I feel that my a basic knowledge about fluid dynamics is very insufficient.

So I am encouraging , I would like to study hard after return the Korea. I am put feel inconvenience about Japanese separation.

Thank you.

5. Future Framework International Exchange between Shizuoka University and Changwon National University

Host teacher's report on Short Term-Stay Program in Shizuoka University

Takayuki Saito, Prof. and Dr. Eng.

Graduate School of Science and Technology

Shizuoka University

The Short-term Stay Program in Shizuoka University, that is a student program between Saito's laboratory of Shizuoka University and Shin's laboratory of Changwon National University (Korea), promoted by Japan Student Service Organization (JASSO) was successfully performed. The students who participated in this program have exchanged their friendships and built a new relationship between the two countries. Furthermore, for these three months from October to December, by themselves, they discussed how to carry out this student program, through a lot of e-mail in English, and prepared meetings that should be held at Hamamatsu campus. Prof. Shin and me gave them only aims of the program and did not direct the details. In spite of the first experience for them, they perfectly prepared it and successfully performed it.

They now know that "open mind" is essential to build friendship and to understand each other. This is the great success which is impossible to describe in a thin report.

I thank Prof. Shin heartily for his acceptance to my proposal regarding this student program and his visit to Shizuoka University.

6. Proceedings of Japanese Students Technical Program

In order to achieve meaningful discussions about presentations with Korean students, under Prof. Saito's supervision, Japanese students made the proceedings of the research content.

Relation between Wake and Zigzag Motion of a Single Bubble

Rintarou Tachibana

Graduate school of Engineering,
Shizuoka University
3-5-1 Johoku, Naka-ku, Hamamatsu,
Shizuoka, Japan

Takayuki Saito

Graduate school of Science and Technology,
Shizuoka University
3-5-1 Johoku, Naka-ku, Hamamatsu,
Shizuoka, Japan

Keywords: Zigzag motion, Wake, Lift force, Shape deformation

Abstract: In the present study, a transition mechanism to explain the change in the motion of a single ascending bubble from linear to zigzag was investigated experimentally. We focused on the relationship between bubble motion (gravity-center motion and shape deformation) and hairpin-like vortex motion. First, these motions were visualized using the infrared shadow technique (IST) and the laser induced fluorescence using HPTS (LIF/HPTS) method. Based on the visualization, the relationship was discussed qualitatively. Second time-series fluctuations of the bubble motion and the vortex motion were quantified. Furthermore, the lift force acting on the bubble was calculated from the displacement of the gravity-center. Finally, the close relation between the wake, the lift force and the shape deformation was discussed quantitatively. We concluded that the wake instability induced by the initial shape deformation observed just after the launch was the dominant factor for the zigzag motion.

1. Introduction

Bubbles are frequently employed in a great variety of industrial process such as CO₂ dissolution process in the environmental plant (Saito *et al.*, 2001), transportation of oil by employing bubble buoyancy driven flows, oxygen supply in the bio reactor and so on. For the safe and efficient operation of the plants, the accurate and adequate modeling of the bubbly flow is essential. To clarify the bubbly flow structure (coherent structure), a lot of researches have been conducted both experimentally and numerically (Mudde, 2005; Darmana *et al.*, 2009). A step-by-step understanding of the bubbly flows is important because there are mutual correlations between the hierarchical structures (Higuchi and Saito, 2010). The size of a single bubble has a great effect on the motion or formation of the bubbly flow (Azbel, 1981). However, even if the knowledge of a single bubble, the smallest unit in the bubbly flow, such as a motion mechanism and its relations with mass transfer have not been yet completely understood. It is well known that the bubble size is a dominant factor for characterizing the bubble motion (Clift *et al.*, 1978). In particular, bubbles with 1.3 – 4.2 mm diameter have interesting characteristics such as zigzag/spiral motion in a rest water column (Magnaudet and Eames, 2000), wake structure so called hairpin-like vortex (Lunde and Perkins, 1997) and the unsymmetrical shape deformation (Saito *et al.*, 2010) and so on. Because of their deep correlation with the mass transfer, researches bases on a discussion with their relationship have been spiritedly conducted (Fan and Tsuchiya, 1990; Koynov *et al.*, 2005). Intriguingly the bubble in the range takes the highest mass transfer coefficient κ_L (Motarjemi and Jameson, 1978).

Many researchers have been investigating the motion mechanism of the bubble by employing various experimental methods and reported some noteworthy results. For an instance, a bubble wake structure is closely related to bubble shape deformation (Sanada *et al.*, 2007; Brücher, 1999). Sanada first visualized the standing eddy on the bubble rear

surface by using photochromic dye. Brücher visualized pseudo wake structure by employing DPIV. They consistently concluded the bubble shape deformation is closely related to the structure or shedding of the hairpin like vortex. However, to obtain or clarify the more precise relationship between them, the detailed description of the bubble shape is required. In fact the bubble surface deformations can not be perfectly described by the fluctuation of the aspect ratio (Miyamoto and Saito, 2005). Furthermore a relationship between the wake instability and the path instability was reported (De Vries *et al.*, 2002; Zenit and Magnaudet, 2009). De Vries *et al.* visualized the wake by employing schlieren method with slight temperature gradient. They concluded the zigzag motion is triggered by periodical replacement of two streamwise vortices. Zenit and Magnaudet employed 2-dimensional PIV measurement for the purpose of calculating force acting on the bubble from circulation in the wake. They experimentally identified that the existence of the two vortices took a significant role in the path instability, namely the wake generates the lift force on the bubble.

Researches based on DNS have been devoted to the good understanding of the zigzagging motion (Magnaudet and Mougin, 2007; Gaudlitz and Adams, 2009). Magnaudet and Mougin investigated the difference between the stable path and unstable path in terms of the relationship between the bubble shape deformation (aspect ratio) and the wake instability. They concluded the wake instability induces the lift force on the bubble; therefore, the bubble path oscillates. Gaudlitz reported the existence of two surface waves on the bubble surface leads to the periodical deformation of bubble shape. Also, he suggested the relationship between the bubble shape and the shedding of a horse-shoe-like vortex.

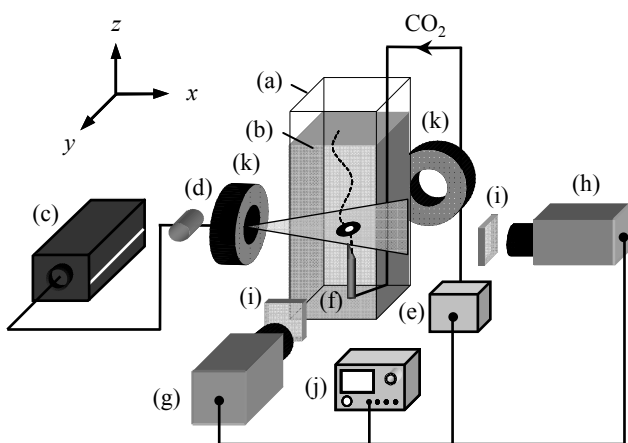
As mentioned above, a lot of researchers focused on the representative three factors, namely, the bubble surface deformation, the wake instability and the Lift force. However the answer for the open question, which is the dominant factor for the motion mechanism so called “egg or chicken”, is still unspecific.

The purpose of the present study is to experimentally clarify a transition mechanism of a single bubble motion in terms of a close relationship among the bubble motion (gravity center motion and the lift), the bubble deformation (not aspect ratio but left-right asymmetry at the bubble edge) and the bubble wake motion. We simultaneously visualized the bubble shape and the bubble wake by employing the Laser induced Fluorescence using HPTS (LIF/HPTS) combined with Infrared Shadow Technique (IST). First we qualitatively discuss a relationship between the bubble motion and the wake motion (PPHVL, Position of the point of the hairpin-like vortex leg). Second the quantitative relationship between them is discussed. Based on the results we discuss a mechanism of the bubble zigzagging motion. Finally we tentatively concluded that the bubble zigzag motion was triggered and maintained by the wake instability which was induced by the unsymmetrical liquid motion near the bubble surface.

2. Experimental setup

Figure 1 shows a schematic diagram of an experimental setup employed in the laser induced fluorescence using HPTS (LIF/HPTS) combined with infrared shadow technique (IST) method. By employing LIF/HPTS method, the dynamical dissolution process and the structure of the part of the bubble wake can be visualized (Hanyu and Saito, 2010). Also the IST method was employed for the clear visualization of the bubble shape; e.g. the interface between the bubble and its surrounding liquid (Tokuhiro *et al.*, 1998).

An acrylic water vessel (a) ($100 \times 100 \times 300 \text{ mm}^3$) was filled with degassed clean water (produced with a Millipore system, specific water resistance was $18.2 \text{ M}\Omega \text{ cm}$ and organic particles were less than 5 p.p.b.), and a very small amount of HPTS (0.0001 [mol/l]) was dissolved into the water (b). The temperature of the water during all experiments was $25 \pm 0.5 \text{ }^\circ\text{C}$. An argon ion laser (Innova 70C-3, COHERENT) (c) was used to excite the HPTS. The laser beam was sheeted by a rod lens (d). The thickness of the laser sheet was 1 mm.



(a) Water Vessel, (b) Clean water & HPTS, (c) Ar ion laser, (d) Rod lens, (e) Bubble-launch device, (f) Hypodermic needle, (g) High-speed video Camera A, (h) High-speed video Camera B (i) Sharp cut filter, (j) Function generator, (k) Red LED (633 nm)

FIGURE 1. Schematic of Experimental setup used in LIF/HPTS combined with IST method.

To obtain a high reproducibility of the bubble condition and the perfect 2-D zigzag trajectory, a special-made bubble-launch device (e) (Saito *et al.*, 2010) with hypodermic needle (f) was employed. High-speed video cameras (Photoron, Fastcam) (g), (h) were mounted on 6 axes optical stages for the precise adjustment (the smallest unit of the regulation was $1.0 \mu\text{m}$ for x, y, z and 0.01 deg for α, β, θ). The camera A was for the visualization in x - z plane; i.e. zigzag plane. The camera B was for the confirmation of the linear trajectory in the y - z plane and the positional relationship between the laser sheet and the bubble. Horizontal transition of the bubble for the y - z plane was 0.1 mm . On the other hand, the transition for the x - z was 10 mm ; therefore the bubble infallibly shows perfect 2-D motion in the x - z plane. All bubbles launched from the device were inevitably within the same plane; i.e. the bubbles passed the same position in the laser sheet. The uncertainty for the average value of the bubble gravity-center was within 2 %. These cameras were equipped with a zoom lens ($f=105\text{mm}$: Nikon) and bellows (Bellows Focusing attachment pb-6: Nikon) to obtain high spatial resolution: $12 \text{ } [\mu\text{m}/\text{pixel}]$. The uncertainty of the bubble shape mainly due to pixel error was within $\pm 1 \%$. A sharp-cut filter (512 high-pass, SIGMA KOKI) (i) inserted between the lens and the vessel cuts scattering light from the bubble surface. The bubble launch-device and the high-speed video camera were synchronized through a function generator (SG-4105, IWATSU) (j). The single bubbles were filmed at any given location and at any given timing. In order to obtain clear images of the bubble shape (contour), IST method using a red LED lights (wave length of 630 nm , LDR-140, NISSIN ELECTRONIC) (k) was employed. Hence, the simultaneous measurements of both IST images and LIF images were performed.

3. Results and discussion

3.1 Bubble motion

A bubble with critical Weber number ranging from 3 to 3.5 shows zigzag trajectory (Hartunian and Sears, 1957; Moore, 1965). More recently, some researchers focused on not only Reynolds number and Weber number but also aspect ratio because the detailed description of the bubble shape is essential for a good understanding of the zigzag motion mechanism (Ellingsen & Risso, 2001; Magnaudet and Mougin, 2007; Zenit and Magnaudet, 2008). Furthermore, the bubble oscillates in its own surface at mode 2,0 or mode 2,2 (Lunde and Perkins, 1998; Pozrikidis, 2004).

The properties of our examined bubble were $D_{eq} = (a^2 \cdot b)^{1/3} = 2.8 \text{ mm}$, $Re_B = 849$, $We = 3.4$, $Mo = 2.6 \times 10^{-11}$ and $Eo = 1.2$ respectively. All dimensionless numbers were calculated base on the bubble just after its launch where the shape can be assumed oblate ellipsoid. The error for the calculation of the D_{eq} was within 1% (Miyamoto and Saito, 2005 for a comprehensive review).

In the image analysis for the bubble motion, we calculated the coordinates of bubble contours from the bubble images processed by binarization and a Sobel filter, and also the coordinates of the bubble gravity centers were obtained. Furthermore, the coordinates were transformed to polar-coordinate system ($r; \theta$) with its origin at the gravity

center (See Fig. 3). The bubble contours were expressed as follows (Duineveld, 1995);

$$r(\theta) = A_0 + \sum_{n=1}^N (A_n \cos n\theta + B_n \sin n\theta),$$

where A_n and B_n were calculated by FFT with mode order N of 8. The major axis D_1 of the bubble image was calculated as the maximum value (i.e. $D_1|_{\theta=\theta_1}$), and the minor axis D_2 was calculated as $r(\theta_1 + \pi/2) + r(\theta_1 + 3\pi/2)$. The aspect ratio was calculated by D_1/D_2 . The ratio has been used in many former researchers (Ellingsen and Risso, 2001); however it is insufficient for the purpose of discussing left-right asymmetry of the bubble shape. Therefore we introduce right and left edge curvatures, $\kappa_R(\theta)|_{\theta=\theta_1}$ at the right edge and $\kappa_L(\theta)|_{\theta=\theta_1+\pi}$ at the left edge in order to quantitatively discuss the time-series shape asymmetry (Saito *et al.*, 2010; Miyamoto and Saito, 2005). They are calculated by

$$\kappa = \frac{|r^2 + 2(dr/d\theta) - r(d^2r/d\theta^2)|}{[r^2 + (dr/d\theta)^2]^{2/3}},$$

here, $\theta = \theta_1$ for κ_R , $\theta = \theta_1 + \pi$ for κ_L .

Figures 2 show the bubble zigzag trajectory with bubble shape (left figure) and the dimensionless curvatures of the edge (center and right figure), respectively. The dominant frequency, wavelength and amplitude of the zigzag motion were 7 Hz, 39.6 mm and 3.0 mm, respectively. The dominant frequencies of the edge dimensionless curvatures were 70.0 Hz. At first, a single bubble ascends linearly, and then the bubble shape was axisymmetric [$t = 0$ [s] - $t = 0.075$ [s]]. Near the first inversion point, the symmetric property collapsed; e.g. the magnitude of the shape deformation at the right edge (κ_R) was larger than that of the left edge (κ_L). However, after the middle point between the inversion points (0.12[s]), the tendency collapsed: i.e. magnitude of the shape oscillation of the left edge gradually increased, while that of the right edge decreased. Near the second inversion point, the κ_L took maximum value. After the point, the magnitude of the shape

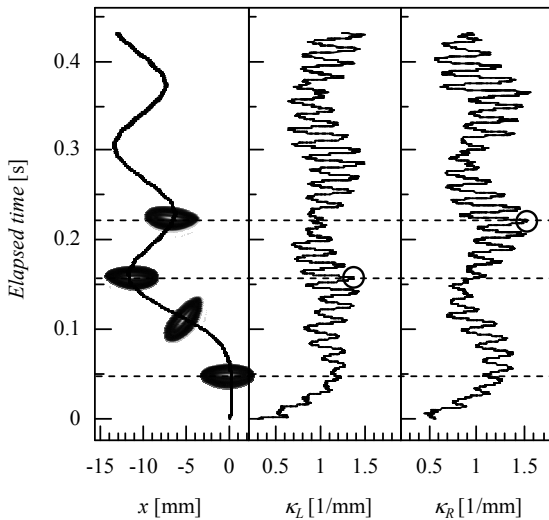


FIGURE 2. A relation between trajectory and bubble shape.

deformation at right edge increased again and took maximum value near the third inversion point. These asymmetrical and periodical deformations of the bubble edge characterize the zigzag motion. The zigzag motion is closely related to the bubble shape (surface) deformation.

3.2 Wake structure and its motion

The wakes behind a hard sphere or bubble are one of the fascinating phenomena in the fluid mechanics field. The formation and shedding frequency of vortices from a sphere highly depends on the Reynolds number (Sakamoto and Haniu, 1994). In terms of the bubble wake, the key factors which describe the wake are not only the Reynolds number but also the bubble shape because millimeter size bubble oscillates its own surface periodically (Lunde and Perkins, 1998). Some researchers tightly focused on the wake instability, because the transition of the bubble gravity center for horizontal direction coincides with the stability of the wake (Magnaudet and Mougín, 2007).

Figure 3 shows time-series growth process of the wake behind a single zigzag bubble near the first inversion point. A standing vortex developed from the center of the bubble rear is observed in Fig. 3 (a), and during this section the bubble rose vertically. Furthermore, the bubble shape is axisymmetric and the major axis of the bubble is horizontal. The symmetric property is gradually collapsing with the bubble ascent and the major axis is gradually leaning to the left. Just before the first inversion point, at (b), the hairpin-like vortex is shed. The bubble changes its orientation and the direction of the motion. After this, the vortex is periodically shed from the bubble rear (c)-(d), and each time the bubble changes its direction of the motion. As marked by a black allows in Fig. 3, a position of the point of the hairpin-like vortex leg (PPHVL) fluctuates at the rear of the bubble. Before the first inversion point, Fig. 3 (a), PPHVL was positioned just at the minor axis of the bubble. At this time, the fluctuations of curvature were gentle. However, when the curvature changed its balance (i.e. the magnitude of the curvature fluctuation at right edge increased), PPHVL shifted toward the right edge [(b)-(c)]. When the bubble shape became axisymmetric again, PPHVL shifted toward the center [(c)-(d)]. The deep correlation between the bubble shape and the wake motion emerges.

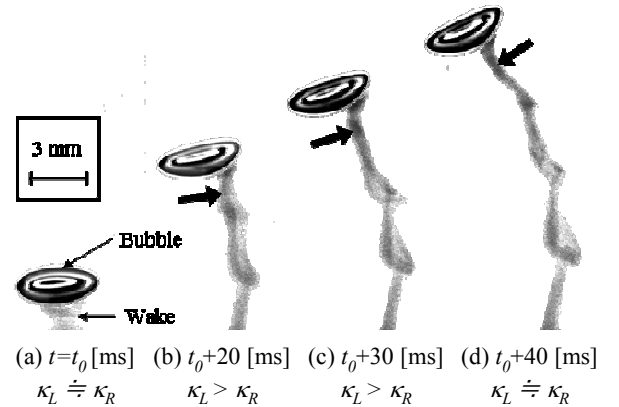


FIGURE 3. Wake behind a single zigzag bubble around the first inversion point.

3.3 Relation between the bubble motion and the wake motion

3.3.1. Shape deformation and the wake

A lot of researchers focused on the relationship between the wake and the bubble shape deformation (Brücker, 1999; Magnaudet and Mougin, 2007; Gaudlitz and Adams, 2009). Their researches are very interesting and valuable to understand the motion mechanism of the zigzag bubble, however, to deeply understand the mechanism, more detailed discussions based on the micro phenomena are essential. As discussed in the 3.2, the wake legs shift its attaching position at the bubble rear. To quantitatively discuss the relationship, we defined the leg position (Figure 4).

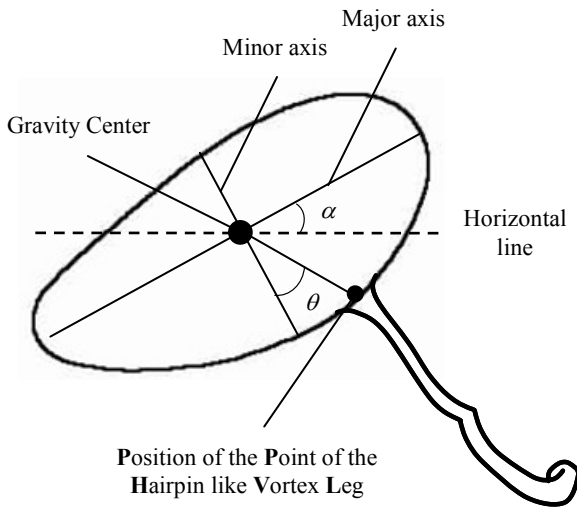


FIGURE 4. Definition of PPHVL, α and θ .

Figure 5 shows the time-series fluctuation of the gravity-center, the shape deformation and the wake leg position. Obviously wave form of each profile was very similar. The dominant frequency for the θ was 70 Hz. When the bubble ascends linearly (0.02 [s] ~ 0.05 [s]), no time lags are observed between each fluctuation. However the fluctuation of the θ became slightly faster than that of the

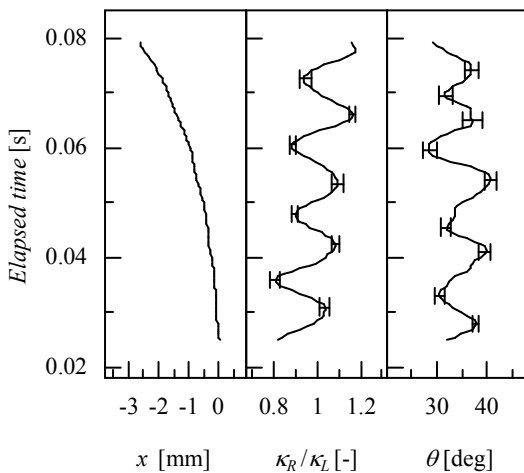


FIGURE 5. Time-series fluctuation of x position, curvature and the vortex leg position.

κ_R/κ_L . After the first inversion point (0.075[s] ~), the lag was π [rad]. The shape deformation was accompanied by the wake instability. This quantitatively means the wake motion dominates the bubble zigzag motion.

3.3.2 Lift force and the wake

Some researchers reported that the wake motion is closely related to lift force acting on the bubble (de Vries *et al.*, 2003; Mougin and Magnaudet, 2006; Zenit and Magnaudet, 2009). They reported that the path instability of the zigzagging bubble was triggered by the instability of the bubble wake.

In this study we estimated the lift from the x -direction displacement of the gravity-center of the bubble, $F_x = \rho V d^2x/dt^2$. This estimation was adequate according to a previous study (Zenit and Magnaudet, 2009).

Figure 6 shows the time-series fluctuation of the lift. The dominant frequency of the lift force fluctuation was 70 Hz. This value is almost as same as that of the wake motion and the shape deformation of the bubble. The lag between θ and F_x was $\pi/4$ [rad.]. This implies the wake instability induced the lift force acting on the bubble. On the other hand, the lag between F_x and κ_R/κ_L was also $\pi/4$ [rad.]. It is considered that bubble gravity-center transition toward horizontal direction increases the asymmetry property between the bubble and the liquid; therefore the bubble shape became axisymmetric.

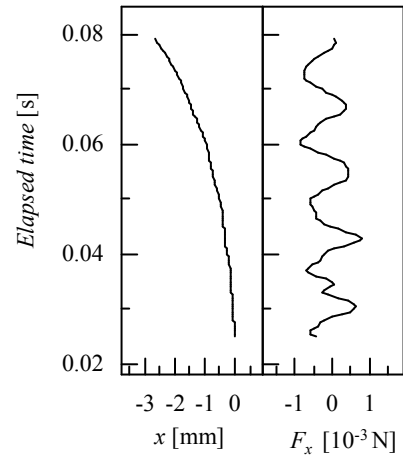


FIGURE 6. Time-series fluctuation of the lift force acting on the bubble.

3.4 Primary cause of the wake instability

Initial shape deformation just after launch characterizes the motion of the bubble (Tomiya *et al.*, 2002). In the present study we control the drift angle of the bubble trajectory by employing an unsymmetrical-shape hypodermic needle. Furthermore the reproducibility of the bubble was so high that the initial shape deformation will be always the same. Therefore the trajectory will also be the same. Figure 6 shows the visualization results of the interface deformation just after bubble was launched from the needle. As marked gray broken line in the figure, a ripple with high curvature propagates the bubble surface in the counterclockwise direction. On the other hand, no noticeable deformation was observed at the left edge. Because of this left-right symmetry, the production amount of the vortex at each edge (right and left) should not be the same

as reported by the numerical study (Magnaudet and Mougin, 2007). Therefore the stagnation points at the front and the rear were differing from that of the linear trajectory (Saffman, 1956). In our characteristic however reliable experimental setup, the trigger for the zigzag motion was the initial shape deformation which induces the asymmetric properties for the surrounding liquid, namely, wake instability. The detailed discussion on the primary instability is the most important future work.

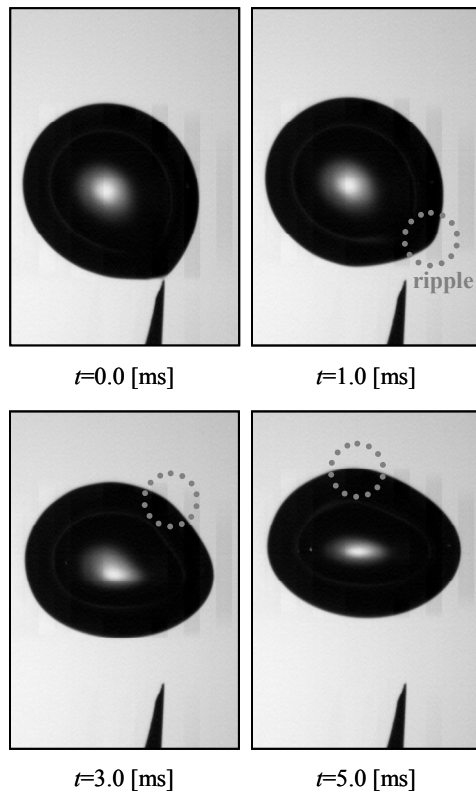


FIGURE 7. Bubble surface deformation observed just after the bubble launch.

4. Concluding remarks

In the present study, a transition mechanism to explain the change in the motion of a single ascending bubble from linear to zigzag was investigated experimentally. The following conclusions were obtained:

- Fluctuation of the wake motion (vortex leg motion), the Lift force and the shape deformation showed same tendency; i.e. the dominant frequencies of the each fluctuation were the same.
- The wake motion was the dominant factor for the bubble zigzag motion.
- The shape deformation observed just after bubble launch have a great effect on the zigzag trajectory (drift angle) and the wake instability.

5. Acknowledgements

The present study was promoted and financially supported by Category "A" of the Grants-in-Aid for Scientific Research, Japan Society for the Promotion of Science. We thank JSPS for its help in the financial support.

6. Reference

- Azbel, D. 1981 Two-phase flows in chemical engineering, Cambridge.
- Brücker, C. 1999 Structure and dynamics of the wake of bubbles and its relevance for bubble interaction. *Phys. Fluids* 11, pp. 1781-1796.
- Clift, R., Grace, J.R. & Weber, M.E. 1978 Bubbles, Drops and Particles, New York: Academic.
- Darmana, D., Deen, N. G., Kuipers, J. A. M., Harteveld, W. K. & Mudde, R. F. 2009 Numerical study of homogeneous bubbly flow: Influence of the inlet conditions to the hydrodynamic behavior, *Int. J. Multiphase. Flow* 35, pp. 1077-1099
- De Vries, A.W.G., Biesheuvel, A. & Van Wijngaarden, L. 2002 Notes on the path and wake of a gas bubble rising in pure water, *Int. J. Multiphase. Flow* 28, pp. 1823-1835.
- Duineveld, P. C. 1995 The rise velocity and shape of bubbles in pure water at high Reynolds number. *J. Fluid Mech.* 292, pp. 325-332.
- Ellingsen, K. & Risso, F. 2001 On the rise of an ellipsoidal bubble in water: oscillatory paths and liquid-induced velocity. *J. Fluid Mech.* 440, pp. 235-268.
- Fan, L.S. & Tsuchiya, K. 1990 Bubble wake dynamics in liquids and liquid-solid suspensions, *Butterworth-Heinemann Series in Chemical Engineering*.
- Gaudlitz, D. & Adams, Nikolaus A. 2009 Numerical investigation of rising bubble wake and shape variations. *Phys. Fluids* 21, pp. 122102.
- Hartunian, R. A. & Sears, W. R. 1957 On the stability of small gas bubbles moving uniformly in various liquids. *J. Fluid Mech.* 3, pp. 27-47.
- Higuchi, M. & Saito, T. 2010 Quantitative characterizations of long-period fluctuations in a large-diameter bubble column based on point-wise void fraction measurements. *Chem. Eng. J.* 160, pp. 284-292.
- Hanyu, K. & Saito, T. 2010 Dynamical mass-transfer process of a CO₂ bubble measured by using LIF/HPTS visualization and photoelectric probing. *Can. J. Chem. Eng.* 88, pp. 551-560.
- Koynov, A., Khinast, J. & Tryggvason, G. 2005 Mass Transfer and Chemical Reactions in Bubble Swarms with Dynamic Interfaces, *AIChE J.* 51, pp. 2786-2800.
- Lunde, K. & Perkins, R.J. 1997 Observations on wakes behind spheroidal bubbles and particles. *ASME Fluids Engineering Division Summer Meeting*, paper 3530.
- Lunde, K. & Perkins, R.J. 1998 Shape Oscillation of Rising Bubbles. *Appl. Scientific Research* 58, pp. 387-408.
- Magnaudet, J. & Eames, J. 2000 The motion of high-Reynolds-number bubbles in inhomogeneous flows. *Annu. Rev. Fluid Mech.* 32, pp. 659-708.
- Magnaudet, J. & Mougin, G. 2007 Wake instability of a fixed spheroidal bubble. *J. Fluid Mech.* Vol. 572, pp. 311-337.
- Miyamoto, Y. & Saito, T. 2005 Relationship between interface motion of an isolated bubble and its zigzagging motion of the center of gravity. *Transaction of Japan Society of Mechanical Engineers Series B* 71, pp. 1307-1313.
- Moore, D. W. 1965 The velocity of distorted gas bubbles in a liquid of small viscosity. *J. Fluid Mech.* 23, pp. 749-766.

- Motarjemi, M. & Jameson, G.J. 1978 Mass transfer from very small bubble -The optimum bubble size for aeration-. *Chem. Eng. Science* 33, pp. 1415-1423.
- Mougin, G. & Magnaudet, J. 2006 Wake-induced forces and torques on a zigzagging/spiraling bubble. *J. Fluid Mech.* 567, pp. 185-194.
- Mudde, R.F. 2005 GRAVITY-DRIVEN BUBBLY FLOWS. *Annu. Rev. Fluid Mech.* 37, pp. 394-423.
- Pozrikidis, C. 2004 Three-dimensional oscillations of rising bubbles. *Engineering Analysis with Boundary Elements* 28, pp. 315-323.
- Saffman, P. G. 1956 On the rise of small air bubble in water. *J. Fluid Mech.* 1, pp. 249-275.
- Saito, T., Kosugi, S., Kajishima, T. & Tsuchiya, K. 2001 Characteristics and Performance of a Deep-Ocean Disposal System for Low-Purity CO₂ Gas via Gas Lift Effect. *Energy & Fuels* 15, pp. 285-292.
- Saito, T., Sakakibara, K., Miyamoto & Y., Yamada, M. 2010 A study of surfactant effects on the liquid-phase motion around a zigzagging-ascent bubble using a recursive cross-correlation PIV. *Chem. Eng. J.* 158, pp. 39-50.
- Sakamoto, H., Haniu, H. 1994 the formation mechanism and shedding frequency of vortices from a sphere in uniform shear flow. *J. Fluid Mech.* 287, pp. 151-171.
- Sanada, T., Shirota & M., Watanabe, M. 2007 Bubble wake visualization by using photochromic dye. *Chem. Eng. Science* 62, pp. 7264-7273.
- Tokuhiro, A., Maekawa, M., Iizuka, K., Hishida, K. & Maeda, M. 1998 Turbulent flow past a bubble and an ellipsoid using shadow-image and PIV techniques. *Int. J. Multiphase Flow* 24, pp. 1383-1406.
- Tomiya, A., Celeta, G.P., Hosokawa, S., Yoshida, S. 2002 Terminal velocity of a single bubbles in surface tension force dominant regime, *Int. J. Multiphase Flow* 28, pp. 1497-1519
- Zenit, R. & Magnaudet, J. 2008 Path instability of rising bubbles: A shape-controlled process. *Phys. Fluids* 20, pp. 061702.
- Zenit, R. & Magnaudet, J. 2009 Measurement of the streamwise vorticity in the wake of an oscillating bubble. *Int. J. Multiphase Flow* 35, pp. 195-203.

An effect of zigzag and surface motions of a CO₂ bubble on the mass transfer from the bubble to the surrounding

Masahiko Toriu
Graduate School of Engineering,
Shizuoka University
Hamamatsu, Shizuoka, Japan

Takayuki Saito
Graduate School of Science and Technology,
Shizuoka University
Hamamatsu, Shizuoka, Japan

Keywords: CO₂, mass transfer coefficient; zigzag motion.

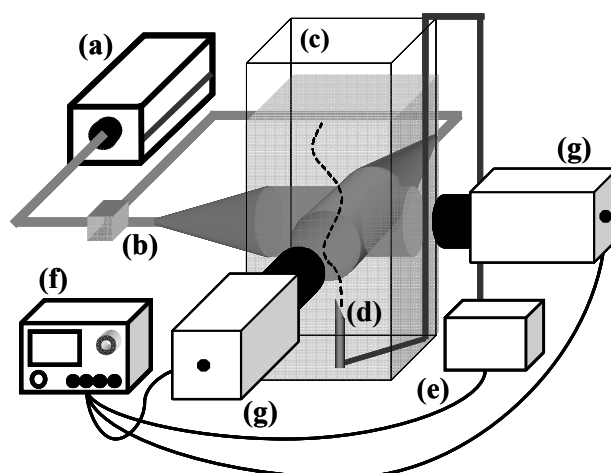
Abstract: A bubbly flow is very useful for aeration, agitation and an enhancement of chemical reaction, etc. in industrial processes. In order to improve the efficiency of the industrial plants, we should acquire the knowledge of a bubbly flow: e.g. bubble motion, mass transfer and surrounding liquid motion. Using a single CO₂ bubble well-controlled in its zigzag motion and surface oscillation, we discuss a relation between the bubble motion and the mass transfer. For this particular purpose, we precisely measured the bubble volume and the surface area, using two high-speed cameras and mirrors. By image processing, a 3D-bubble shape was reconstructed based on the projected bubble images. We regarded the volume/surface area of 3D-model as the volume/surface area of the examined bubble. In addition, instantaneous mass-transfer coefficients were calculated from these results. The mass transfer of the bubble was enhanced when the bubble trajectory shifted from the linear mode to the zigzag mode.

1. Introduction

Bubbles of 2-3 mm diameter take the highest mass transfer coefficient K_L (Motarjemi & Jameson, 1978). The physical phenomena of those bubbles are far more complex than those of the small spherical bubbles due to the following reasons; they can be approximated as a oblate ellipsoid with surface oscillation (Miyamoto & Saito, 2005, Saito, et al., 2010); they rise zigzagging or spiraling in a rest water column; in addition it is known that the zigzagging bubbles shed a characteristic wake (i.e. horse-shoe-like vortex). The effects of the vortex shedding on the mass transfer and the relation between the bubble motion and the mass transfer are still unknown. In this paper, we discuss a relation between the instantaneous mass transfer and the bubble motions, based on the highly precise measurement of the bubble volume. For this particular purpose, we visualized the zigzagging motion and the surface oscillation 3-dimensionally and simultaneously, using two high-speed cameras and mirrors. Finally, we discuss dominant factors that affect the mass transfer from the bubble to the ambient liquid by comparison of the instantaneous mass transfer, the bubble motions and the bubble dynamics.

2. Experimental setup

Fig. 1 shows a schematic diagram of experiment setup. An acrylic water vessel (c) was filled with ion-exchanged and degassed water. An Ar ion laser system (a) was used as backlights. The laser beams were split by a half mirror, and the beams were expanded/collimated by a beam expander and illuminated an observed area. A highly-reproducible bubble was launched from a bubble generator (e); the device consists of a hypodermic needle (d), an audio speaker and two precise pressure controllers, and controls the zigzag motion, size, surface oscillations, position and orientation (Saito et al, 2010). The bubble generator and high-speed cameras (exposure time 10 μ s, resolution 1024 \times 1024 pixels, and spatial resolution 6.01 μ m/pixel) were synchronized with a function generator; i.e. launching and filming the single bubbles at the



(a)Ar⁺ laser, (b)Half mirror, (c)Water vessel, (d)Hypodermic needle, (e)Bubble-launch device, (f)Function generator, (g)High-speed cameras

FIGURE 1. Schematic of experimental setup.

same timing were realized. As a result, the zigzag motion of the bubble and the bubble surface oscillation were visualized from two directions simultaneously. Moreover, for the verification of bubble shape, the projected bubble geometry was visualized from vertical direction by using a high speed camera (exposure time 10 μ s, resolution 1024 \times 1024 pixels, and spatial resolution 8.46 μ m/pixel) and mirrors.

3. Calculation of the bubble volume

3.1. Bubble shape

In preparation for the bubble-volume calculation, we verified the shape of a bubble with the zigzag motion and periodical surface oscillations. The projected bubble image was visualized from two directions intersecting at right angles

each other (the x-z plane is called “front”; the y-z plane is called “side”). The bubble showed the perfect 2-D zigzag motion on the front and the linear ascent motion on the side. Fig. 2 shows the projected bubble geometry. The projected bubble geometry was a symmetrical about a minor axis on the front and symmetrical about zigzag-motion plane on the side/top. From these characteristic bubble geometries, we made the following assumptions; 1) the projected bubble geometry on a top is fairly circle or ellipse, 2) the bubble geometry is nearly circle or ellipse in each cross-section which is parallel to the major axis on front/side and perpendicular to the minor-axis of the bubble.

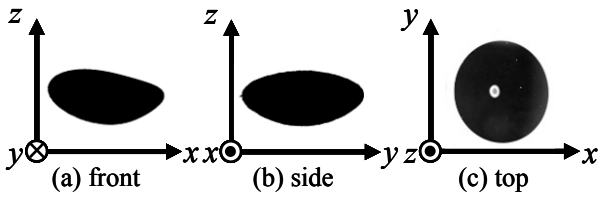


FIGURE 2. Bubble geometry on each plane.

3.2. Algorithm for reconstruction of a 3D-bubble from the projected bubble images

We propose a method for accurate calculation of a bubble volume and surface area by image processing. The bubble volume was calculated from the projected bubble images from two directions and the geometric assumptions described above. This calculation composed of three processes as described below: (1) the extraction of bubble geometry on the front/side, (2) the construction of 3D-bubble model (Fig. 3), (3) the calculation of volume and surface area of the 3D-bubble model.

(1) The extraction of bubble geometry.

The bubble geometries were extracted by the edge extraction by zero-crossing method and the binary process. In addition, the position of bubble centroid and major/minor axis, etc. are calculated from the bubble image.

(2) The formation of rough bubble shape.

Fig. 3 shows the algorithm for the construction of 3D-bubble model. First, we define a cubic model which is larger than bubble and composed of a lot of micro cubes $6.01\mu\text{m}$ on a side. This size of micro cube is determined from the spatial resolution of the bubble image. We construct a 3D-bubble model from the cubic model. At first, the cubic model is cut away some fat that don't fit the bubble image on the front/side by checking a model shape from the bubble geometries on the front/side. Next, we apply the above presumptions of bubble-shape characteristics to the bubble model for the construction in minute detail of 3D-bubble model. The presumptions which are No.1 and No.2 shave the extra part of bubble model on the each layer which is parallel to the major axis on front/side and perpendicular to the minor-axis of bubble.

(3) The calculation of volume and surface area.

To begin with, we calculate the bubble volume. We obtain a number of layer-by-layer micro cubes by counting micro

cubes at each layer of the bubble model and multiply a micro-cube volume. Then, we integrate numerically all layer-by-layer volume by Simpson's rule. Next, we calculate the bubble surface area. It is counted the faces, which compose the gas-liquid interface, of a micro cube. And then, we obtain the bubble surface area by multiplying the total number of face by the lateral area of micro cube.

3.3. Evaluation of the bubble volume calculation

Fig. 4 shows the air-bubble volume of both the calculation by image processing and the actual measurement. The bubble image was taken in the section which is from the tip division of hypodermic needle to above the needle (i.e. $z=0-3[\text{mm}]$). In a section from $z=2[\text{mm}]$ to $3[\text{mm}]$, the bubble shape is assumed oblate ellipsoid from the bubble geometries on front/side. It was verified that the difference between air-bubble volume of actual measurement and calculation by image processing is within $\pm 0.4[\%]$. In a section from $z=0$ to $2[\text{mm}]$, It was verified that the difference between air-bubble volume of actual measurement and calculation by image processing is up to $1.4[\%]$. Why the difference in a section in $z=0-2[\text{mm}]$ is larger than in $z=2-3[\text{mm}]$, the bubble deformation is excited when the bubble is away from hypodermic needle. So, the bubble shape doesn't match with the presumptions of bubble-shape characteristics. Also, in other section, there are the differences by the discriminative bubble deformation. So, we need to correct for the influence of bubble deformation against calculation result. For the revision of bubble-volume values, we accurately measured the air/ CO_2 bubble volume at the same position and timing. We decided that the volume change of the air bubble is due to the influence of bubble deformation, because the Air bubble is least soluble compared to the CO_2 bubble. So, we corrected for the differences by the bubble deformation, based on a result of air-bubble volume measurement.

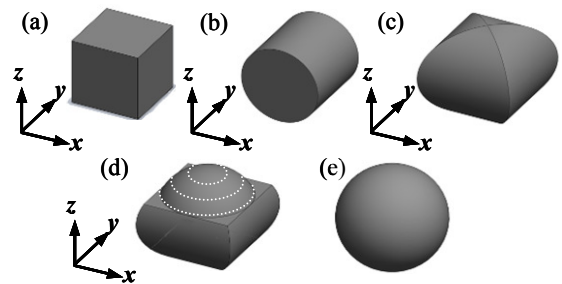


FIGURE 3. Algorithm for the construction of 3D-bubble model.

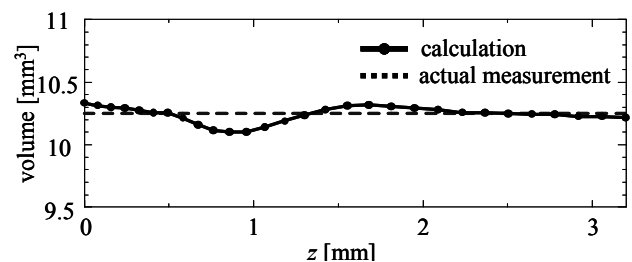


FIGURE 4. Actual measurement/calculation values of the air-bubble volume.

4. Results and discussion

Figures 5 show (a) a bubble trajectory, (b) a bubble volume, (c) a bubble surface area, (d) an instantaneous mass-transfer coefficient, and (e) a bubble rise velocity during the bubble ascent motion from the tip of the hypodermic needle to the second-inversion point, respectively. We calculated the instantaneous mass-transfer coefficient k_L by the following formula,

$$k_L = \Delta V / (S \cdot \Delta t), \quad (1)$$

where ΔV is the value of volume shrinkage in Δt seconds, S is the averaged surface area in Δt . k_L clearly increases at the sections of $0 \text{ mm} < z < 15 \text{ mm}$ (just after the bubble launch) and $35 \text{ mm} < z < 50 \text{ mm}$ (around the second-inversion point of zigzag trajectory). At the section of $0 \text{ mm} < z < 15 \text{ mm}$, the bubble was accelerated rapidly (Fig. 5 (e)); i.e. the relative velocity of the surrounding liquid became high rapidly. The surrounding liquid on the bubble surface was quickly renewed, and hence the mass transfer from the bubble to liquid is enhanced by the effect of a heightened concentration gradient in the interface. On the other hand, at the section of $35 \text{ mm} < z < 50 \text{ mm}$, the bubble reached its terminal velocity and moved at a constant velocity (Fig. 5 (e)). Therefore, there is no effect of the increase in a renewal speed on enhancement of the mass transfer. However, in this section, shedding hairpin vortices are induced, and the vortices are transported and defused by a strong upward flow behind the bubble. These promote the mass transport from the bubble to the surrounding liquid.

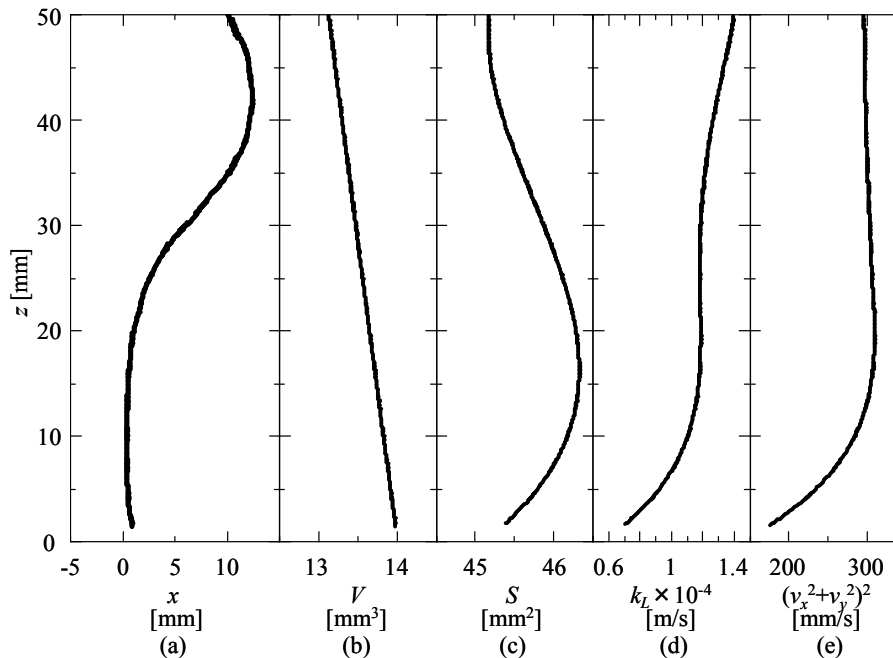
5. Conclusion

In this study, we discussed a relation between the instantaneous mass transfer and the bubble motion. For this particular purpose, we obtained the instantaneous mass-transfer coefficient, based on the accurate and precise bubble volume measurement.

As a result, k_L clearly increased at the sections near the bubble launch and the second inversion point. In these sections, the bubble made the increase in a relative velocity, the induction of shedding vortices, and the strong upward flow behind the bubble. Hence, the concentration gradient in the interface was increased by the high renewal speed of liquid on the interface and the enhancement of mass transport and diffusion. Consequently the mass transfer from bubble to liquid is enhanced. We conclude that the characteristic bubble motion affects the mass transfer from bubble to liquid.

6. References

- Motarjemi, M. & Jameson, 1978, G. J. Mass Transfer from Very Small Bubbles-The Optimum Bubble Size for Aeration, *Chem. Eng. Sci.*, **33**, 1415-1423.
- Miyamoto, Y. & Saito, T., 2005, Relationship between Interface Motion of an Isolated Bubble and its Zigzagging Motion of the Center of Gravity., *J. Soc. Mech. Eng.*, B71-705, 1307-1313.
- Saito, T, et al. 2010, A study of surfactant effects on the liquid-phase motion around a zigzagging-ascent bubble using a recursive cross-correlation PIV, *Chem. Eng. J.*, **158**, 39-50.



An Experimental Study of Gas-liquid Interaction in Decaying Turbulence Formed in a Water Vessel Equipped with an Oscillating-grid

Yasuyuki Nagami
Graduate School of Engineering,
Shizuoka University
Hamamatsu, Shizuoka, Japan

Takayuki Saito
Graduate School of Science and Technology,
Shizuoka University
Hamamatsu, Shizuoka, Japan

Keywords: Gas-liquid two-phase flow, Gas-liquid interaction, Oscillating-grid decaying turbulence, Bubble.

Abstract: Gas-liquid interaction is essential to deeply understand the complicated mechanism and structures of a gas-liquid two-phase flow. The purpose of the present study is to clearly extract modulation of the bubble-liquid interaction and to discuss the relations between the bubble and liquid-phase motions through experiments. We employed a completely controlled bubble (with high reproducibility of size, a trajectory and a surface oscillation) and oscillating-grid decaying turbulence (grid frequency: 4 Hz, grid stroke: 40 mm). We found out that the transition of the 2D zigzagging motion to the 3D motion was enhanced in the oscillating-grid decaying turbulence. In the area of the transition start, we measured liquid-phase motion with PIV/LIF and simultaneously filmed bubble images with infrared shadow bubble technique (IST). We discussed the modulation of the bubble motion and ambient liquid-phase motion and considered the dominant factor for the transition of the bubble motion from 2D to 3D.

1. Introduction

The interaction between the gas and liquid-phase plays a significant role in gas-liquid two-phase flows (e.g. Boden et al. 2008, Vlasogiannis et al. 2002, Saito et al. 1999, 2010). Quantitative discussion of the gas-liquid interaction is important to understand their complicated structures and mechanisms. The objective of this paper is to discuss the bubble-liquid interaction in the gas-liquid two-phase flows through experiments.

Although many researches about the bubble motion, liquid-phase motion, and the interaction between the bubble and liquid-phase motion numerically and/or experimentally, a knowledge of the interaction is still insufficient in particular for bubbly flows. The bubble examined in the present study was an oblate ellipsoid of 2.9 mm in equivalent diameter; the bubbles ascend zigzag or spirally (Clift et al. 1978) accompanying with the drift motion (Brücker 1999) and surface oscillation (Fan & Tsuchiya 1990). Thompson & Turner (1975) quantified oscillating-grid turbulence in a rest water column. Hopfinger et al. (1982) applied an oscillating-grid to a rotating tank experiment, and discussed an interaction between the homogeneous isotropic turbulence and the vortex produced by the rotation. Bröder & Sommerfeld (2003) described a measurement system to acquire bubble sizes, bubble velocities and liquid velocities the decaying turbulence, resulted in the enhancement of the transition of the bubble motion from 2D motion to 3D motion.

2. Experimental setup

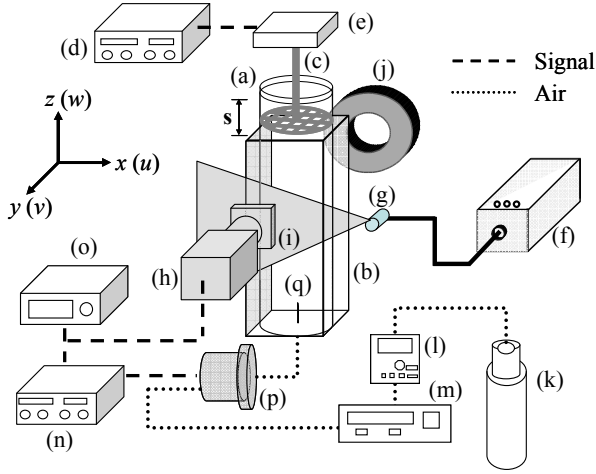
2.1. Oscillating-grid decaying turbulence

The schematic view of the employed experimental setup is illustrated in Fig. 1. The oscillating-grid decaying turbulence was formed in an acrylic cylindrical vessel (diameter: 149 mm, height: 600 mm) covered with a square-section acrylic water jacket to remove refraction and a deformation of a bubble

allowed in a bubbly two-phase flow by combining images obtained via PIV and PTV. Zenit & Magnaudet (2009) measured the steamwise vorticity in the wake of a bubble with oscillating motion and reported the bubble wake motion becomes unstable when the bubble aspect ratio exceeds a critical value.

Morikawa & Saito (2008) described a turbulence modulation induced by an interaction between flow produced by bubble swarms and liquid-phase ambient isotropic turbulence, by using a LDA system. Imaizumi & Saito (2010) advanced that standard deviation of liquid-phase motion was increased by a bubble swarm. In order to more deeply understand the relation between the bubble motion and the liquid-phase motion, we employed IST (Infrared Shadow Technique) for capturing the bubble motion, and PIV/LIF for obtaining the liquid-phase motion. Furthermore, we visualized the bubble-wake motion with LIF/HPTS in order to discuss the relation between the bubble motion and the bubble-wake motion. We found out the transition of the bubble motion from 2D zigzagging motion to 3D motion was enhanced in the oscillating-grid decaying turbulence. The initial bubble motion was not influenced by the surrounding decaying turbulence. The asymmetry of the standard deviation of the liquid-phase velocity and the irregular fluctuation of the bubble wake motion, which were influenced by image. The origin of the coordinate system (x, y, z) was set at the center of the vessel bottom. The vessel was filled with purified water (ion-exchanged and degassed tap water). The grid (mesh size: 18 mm, bar thickness: 4 mm) was driven by computer-controlled servomotor (frequency: 4 Hz, stroke: 40 mm). The neutral position of the grid oscillation was positioned at $z = 392$ mm. The oscillating-grid was stopped after worked for 60 seconds. The decaying turbulence was formed after stopping the oscillating grid. The measurements were performed under two experimental conditions; the first

one was the bubble launched into the stagnant water (Condition-B), the second one was the bubble launched into the oscillating-grid decaying turbulence (Condition-OB).



(a) Cylindrical vessel, (b) Water jacket, (c) Grid, (d) Controller, (e) Servomotor, (f) YAG Laser, (g) Rod lens, (h) High-speed video camera, (i) Sharp cut filter, (j) LED, (k) Cylinder of pure air, (l) Pressure controller 1, (m) Pressure controller 2, (n) Function generator, (o) Power amplifier, (p) Audio speakers, (q) Hypodermic needle

FIGURE 1. Schematic diagram of experimental setup.

2.2. Bubble launch device

The bubble was launched via the in-house specially-made bubble launch device equipped with a hypodermic needle; hence uniform bubble was repeatedly formed and launched at controllable launch timing (Saito et al. 2010). Pure air from a cylinder was adjusted by two pressure controllers for coarse-range adjustment and precise-range adjustment, and was inputted to the narrow space between the audio speaker and pressure vessel. The audio signals were sent to the speaker from a function generator through a power amplifier. The bubble launch interval was arbitrarily controlled by the function generator. The bubble was launched into the water through the hypodermic needle (outer diameter: 0.65 mm, inner diameter: 0.40 mm) which set at the bottom and center of the vessel. The edge of hypodermic needle was set toward x -direction. The needle was able to repeatedly release the bubble of the same initial shape. In addition, the trajectory was also highly controlled (Saito et al. 2010). We visualized the bubble motion via IST (Infrared Shadow Technique with a high-speed video camera). In order to extract a clear contour of the bubble, a ring-shaped continuous red-LED array (wavelength: 660 nm) was placed at the opposite side of the camera and a sharp cut filter (wavelength 560 nm) was set in front of high-speed camera in order to remove scattering noise from the bubble surface. The spatial resolution was 1024×1024 pixel² (19.1 $\mu\text{m}/\text{pixel}$), and the frame rate was 1000 fps. The valuation method of the bubble motions were shown in the Fig. 2.

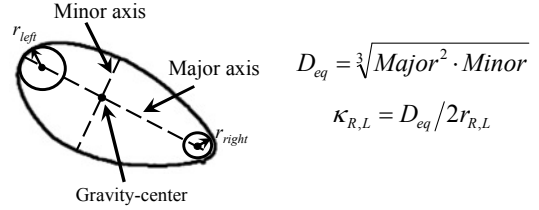


FIGURE 2. The valuation method of the bubble motion.

3. Results and discussions

3.1. Bubble motion

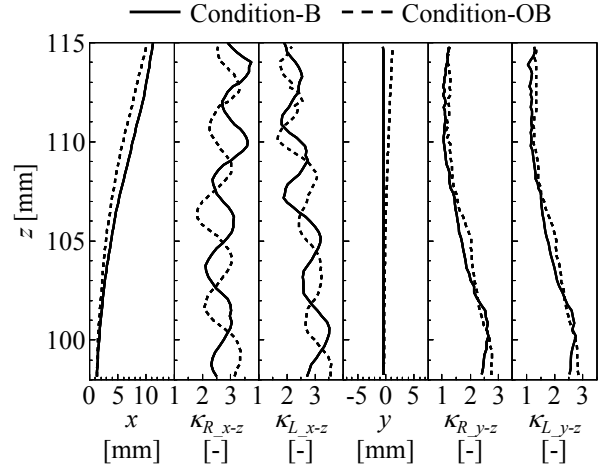


FIGURE 3. The gravity-center motion and the surface oscillation.

In the past study, we already meticulously confirmed the initial condition of the bubble motions (gravity-center motion and surface oscillation) were not influenced by the ambient decaying turbulence (Nagami & Saito 2011). The trajectories of the gravity-center and the surface oscillation in $z = 95 - 115$ mm are plotted in Fig. 3. This is the area where the bubble reached to the first inversion point from the rectilinear rise. Considering these results, under Condition-B, the trajectory was rectilinear on the y - z plane. The bubble motion in the stagnant water was 2D motion in the examined area. On the other hand, the difference in the trajectory under Condition-OB appeared obviously in the area near $z = 95$ mm. This indicates the point at which the transition from 2D motion to 3D motion started. Comparing the bubble gravity-center motion with the bubble surface motion, the region at which the former motion was modulated well corresponded with the region at which the phase difference of the curvature fluctuation occurred. In this area, the amplitude of right-side and left-side curvature fluctuations is almost the same under Condition-B and Condition-OB. However, in a height near to $z = 105$ mm under y - z plane, the largest difference of the right-side and left-side curvature was appeared. This result corresponded to the standard deviation of liquid-phase deviation which described in the next section.

3.2. Liquid-phase motion

An Nd: YAG laser (wavelength: 532 nm), and laser fluorescence particles (average diameter: 8 μm , excitation wavelength: 532 nm, emission wavelength: 570 nm) completely dispersed in the water were used. The interrogation area was illuminated with the laser sheet through a rod lens. We calculated the standard deviation of liquid-phase motion from the original PIV images. Because the condition of the decaying turbulence is inability to predict in each time, we separately compared the experimental result in each time, based on the spatial and time average results calculated from all of data sets. The contour maps of the horizontal and vertical standard deviation of liquid-phase velocity components calculated from one data set are shown in Fig. 4.

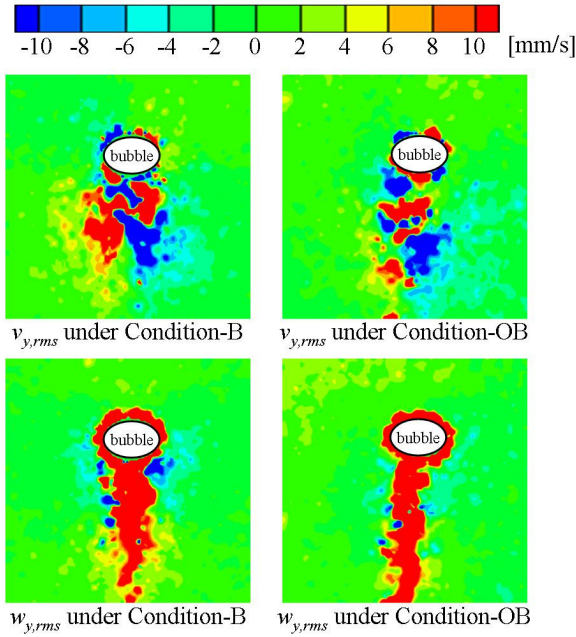


FIGURE 4. A set of typical contour figures standard deviation of liquid-phase velocity components on the y - z plane.

Yoshimoto & Saito (2010) measured a single bubble motion (shape oscillation and zigzag motion) and the surrounding liquid motion around the bubble by using Stereo-PIV method near the first inversion point. They considered that the asymmetry of shape oscillation resulted in the velocity difference between left-side and right-side of the bubble. In the Fig. 4, the areas of the negative standard deviation under Condition-B were reduced or disappeared under Condition-OB. The asymmetry and imbalance of the standard deviation of liquid-phase velocity was influenced by the decaying turbulence and the bubble surface oscillation. Based on these result, we consider that the bubble surface motion is related to the enhancement of the transition of bubble motion from 2D motion to 3D motion. In fact, the amplitudes of the curvature fluctuations observed in the y - z plane modulated in the decaying turbulence as shown in Fig. 3.

3.3. Bubble wake motion

In the present study, we employed LIF/HPTS (8-hydroxypyrene-1, 3, 6-trisulfonic acid) method in order to visualize the CO_2 transportation from the bubble surface to the oscillating-grid decaying turbulence. An argon-ion laser system (wavelength: 488 nm) was used to excite the HPTS (excite wavelength: 488 nm, emission wavelength: 532 nm). HPTS changes its emission intensity depending on pH of the solvent. A CO_2 gas (CO_2 : 99.9%, N_2 : 0.9ppm, O_2 : 0.9ppm) was supplied from a gas cylinder through the bubble launch device. During the ascent of the CO_2 bubble in HPTS solution, the emission intensity decreases in the regions in which the CO_2 included in the bubble is dissolved. The CO_2 -rich regions are easily distinguished from the other regions of no dissolution of CO_2 due to the brightness differences. A set of typical original images is shown in Fig. 5.

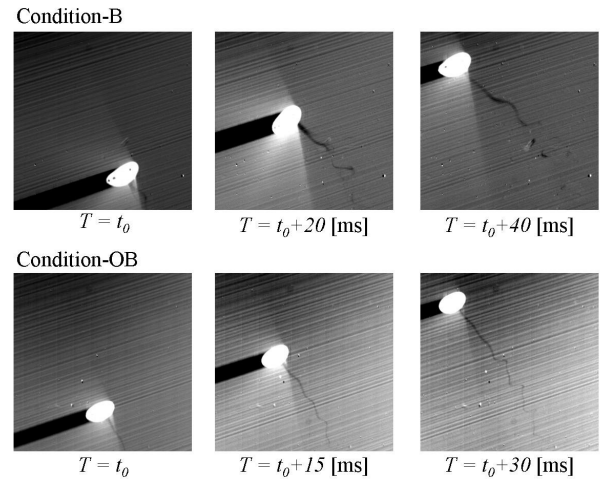


FIGURE 5. A set of typical image of the bubble wake motion.

Tachibana & Saito (2011) experimentally investigated a single bubble motion translated from linear motion to zigzag motion induced by the fluctuations of the position of the point of the hairpin like vortex leg on the bubble rear surface. In this paper, because the measurement area is where the bubble motion started to translate from 2D motion to 3D motion, the growth process of the dynamic vortexes and the position of the point of the hairpin-like vortex leg were considered to have been influenced by the ambient decaying turbulence. As a result, the gauge of the bubble wake under Condition-OB was thinner than that under Condition-B. Influenced by the ambient decaying turbulence, the irregular fluctuation of the bubble wake motion is another significant factor for the enhancement of the transition of the bubble motion from 2D motion to 3D motion.

4. Conclusions

In the present study, we employed oscillating-grid decaying turbulence and an in-house specially-made bubble launch device in order to systematically and experimentally investigate the interaction between the bubble motion and the ambient liquid-phase motion. The modulations of the bubble gravity-center motion, bubble surface oscillation, the standard deviation of the liquid-phase velocity and the bubble wake

motion were discussed by comparing those in the decaying turbulence with those in the rest water. By combining these results, we pinpointed the area where the transition of the bubble motion from 2D to 3D was enhanced in the decaying turbulence compared with that in the rest water. In the y - z plane, the asymmetry and imbalance of the standard deviation of liquid-phase velocity was influenced by the decaying turbulence and the bubble surface oscillation. We considered the two-way interaction is one of the dominant factors in the enhancement of the transition of the bubble motion from 2D motion to 3D motion. In addition, we successfully captured the bubble wake motion in the decaying turbulence. We considered the irregular fluctuation of the bubble wake motion influenced by the ambient decaying turbulence is another significant factor for the enhancement of the transition of the bubble motion from 2D motion to 3D motion.

5. References

- Boden, S., Bieberle, M. & Hampel, U. 2008 Quantitative measurement of gas hold-up distribution in a stirred chemical reactor using X-ray cone-beam computed tomography. *Chem. Eng. J.* 139, pp 351-362.
- Bröder, D. & Sommerfeld, M. 2003 Combined PIV/PTV-measurement for the analysis of bubble interactions and coalescence in a turbulent flow. *The Canadian Journal of Chemical Engineering*, Vol. 81, pp. 756-763.
- Brücker, C. 1999 Structure and dynamics of the wake of bubbles and its relevance for bubble interaction. *Physics of Fluids* Vol. 11(7), pp 1781-1796.
- Clift, R., Grace, J. R. & Weber, M. E. 1978 *Bubbles, Drops and Particles* New York: Academic.
- Fan, L. S. & Tsuchiya, K. 1990 Bubble wake dynamics in liquids and liquid-solid suspensions. *Butterworth-Heinemann Series in Chemical Engineering*.
- Hopfinger, E. J., Brow, F. K. & Gagen, Y. 1982 Turbulence and waves in a rotating tank. *Journal of Fluid Mechanics*, Vol. 125, pp. 505-535.
- Imaizumi, R. & Saito, T. 2010 Bubble and liquid-phase motion in a decaying turbulence field of oscillating-grid turbulence. *7th ICMF*, in usb.
- Morikawa, K., Urano, S., Sanada, T. & Saito, T. 2008 Turbulence modulation induced by bubble swarm in oscillating-grid turbulence. *Journal of Power and Energy Systems*, Vol. 2(1), pp. 330-339.
- Nagami, Y and Saito, T 2011 The motion of a bubble swarm in decaying oscillating-grid turbulence and the modulation of the liquid-phase motion. *ASME-JSME-KSME Joint Fluids Engineering Conference 2011*
- Saito, T., Sakakibara, K., Miyamoto, Y. & Yamada, M. 2010 A study of surfactant effects on the liquid-phase motion around a zigzagging-ascent bubble using a recursive cross-correlation PIV. *Chemical Engineering Journal*, Vol. 158, pp. 39-50.
- Saito, T., Kajishima, T. & Tsuchiya, K. 2010 Deep ocean CO₂ sequestration via GLAD (Gas-Lift Advanced Dissolution) system. *J. of Environment and Engineering*, Vol. 6(2), pp. 412-415.
- Tachibana, R. & Saito, T. 2011 A relation between the wake and zigzag Motion of a single bubble. *Transactions of the Japan Society of Mechanical Engineers series B*, accepted, in Japanese.
- Thompson, S. M. & Turner, J. S. 1975 Mixing across an interface due to turbulence generated by an oscillating grid. *Journal of Fluid Mechanics*, Vol. 67, pp. 349-368.
- Tomiyama, A., Celata, G. P., Hosokawa, S. & Yoshida, S. 2002 Terminal velocity of single bubbles in surface tension force dominant regime. *International Journal of Multiphase Flow*, Vol. 28, pp. 1497-1519.
- Vlasogiannis, P., Karagiannis, G., Argyropoulos, P. & Bontozoglou, V. 2002 Air-water two-phase flow and heat transfer in a plate heat exchanger, *Int. J. Mult. Flow* Vol. 28, pp. 757-772.
- Yamamoto, M., Masato Y., Koichi M. & Saito, T. 2008 Coupling mechanism between liquid phase motion and mass transfer around single rising bubbles by using PIV/LIF. *In 14th Int Symp on Applications of Laser Techniques to Fluid Mechanics*.
- Zenit, R. & Magnaudet, J. 2009 Measurements of the streamwise vorticity in the wake of an oscillating bubble. *International Journal of Multiphase Flow*, Vol. 35, pp. 195-203.

A simple yet powerful technique to detect the pierced position by using a pre-signal in bubble measurement with a Single-Tip Optical fiber Probe

Yuki Mizushima

Graduate School of Engineering,
Shizuoka University, 3-5-1 Johoku, Hamamatsu,
Shizuoka, Japan

Takayuki Saito

Graduate School of Science and Technology,
Shizuoka University, 3-5-1 Johoku, Hamamatsu,
Shizuoka, Japan

Keywords: Single-Tip Optical fiber Probe, Bubbly flow, Measurement accuracy, Pre-signal.

Abstract: The Optical Fiber Probe (OFP) measurement is generally used for gas-liquid two phase flow measurements. The OFP enables researchers to measure the diameters and the velocities of the bubbles/droplets simultaneously, in real time. One of the authors originally developed a Single-Tip Optical fiber Probe (S-TOP) with a wedge-shape tip. The S-TOP can measure the properties of the bubbles/droplets with only the single-tip. Due to the simple but smart structure, the S-TOP is specialized for measurement of a sub-mm or μm order bubble/droplet. However, this advantage of the single-tip inevitably brings a bottleneck problem: i.e. an unknown factor of a touch position between the S-TOP and the bubble/droplet. The bubble diameter is calculated with the S-TOP's piercing chord length. Hence, the chord length greatly depends on the touch position; however, the touch positions are different in every bubble. As a result, the bubble diameter obtained by the S-TOP has uncertainty. This uncertainty is difficult to be quantified and removed. The purpose of this study is improving the accuracy of the S-TOP bubble measurement. To realize this, we overcome the bottleneck with a pre-signal. The pre-signal appears when the OFP tip shapes wedge, and just before the tip pierces the bubble. Its amplitude is the largest of all touch-conditions, when the S-TOP touches the center of the bubble, perpendicularly: this is the best touch-condition that the S-TOP can measure the properties of the bubbles with high degree of accuracy. Utilizing this phenomenon, we propose a pre-signal threshold method. By using this, we can easily discriminate whether the touch-condition is needed, or is not. In this paper, we have demonstrated the effectiveness of the method, empirically. Consequently, as for the bubble chord length measurement, the difference of the results between the visualization and the S-TOP is remarkably improved from -42% to -21%.

1. Introduction

Gas-liquid two phase flows widely appear in the industrial processing, such as the bioreactor, the chemical plants, and so on. However, the flow structure is very complicated; hence, the description for the bubbly flow is still non-committal. It is because that there are no reasonable measurement techniques for the two phase flows. The visualization, PIV (Particle Image Velocimetry) (Brücker, 1999), PTV (Particle Tracking Velocimetry) (Ortiz-Villafuerte *et al.*, 2000), and so on, is useful measurement method; however, visualizing bubbles quantitatively and individually is impossible. It causes that we seem to overlook the important facts, the bubble diameters/velocities and the local void fraction. As a result, the measurement results from the visualization stay rough. The optical fiber probe (OFP) (Miller *et al.*, 1970, Abuaf *et al.*, 1978, Cartellier, 1990, Mudde and Saito, 2001, Higuchi and Saito, 2010) is one of the novel measurement techniques for the two phase flows. The OFP directly measures the diameters and the velocities of the bubbles/droplets intrusively but successfully, even though in a high number of density. One of the authors newly developed a Single-Tip Optical fiber Probe (S-TOP) (Saito, 2000, Matsuda *et al.*, 2009, Ozawa *et al.*, 2009, Saito *et al.*, 2010). The S-TOP can measure the diameters and the velocities of bubbles/droplets with its single wedge-shape tip.

In this study, we aim at establishing a correction method for the S-TOP measurement. The S-TOP measurement is the point-wise measurement; therefore, the piercing position on

the bubble is quietly important. When the S-TOP detects the bubble, a chord length of piercing is obtained. The length is equal to the minor axis of the bubble, when the S-TOP pierces the center of the bubble vertically. In this case, the S-TOP measurement is accurate; however, this is the rare case. The bubbles in the bubbly flow move with various orientations. The S-TOP often pierces the bubbles imperfectly. The S-TOP grazes the bubbles, pierces the edge of the bubbles, or so on. As a result, the results from the S-TOP have uncertainty. N. N. Clark *et al.* have attempted to quantify this uncertainty from the numerical approach (Clark and Turton, 1988, Liu and Clark, 1998); however, it has never been a radial solution. Consequently, this problem always follows the OFP measurement, and is considered as two sides of the coin.

To break out this problem, using a pre-signal is very effective (Mizushima and Saito 2011). The pre-signal appears when the tip shapes wedge. It occurs just before the S-TOP's touching on the bubble, and intensively when the S-TOP is positioned at the center region of the bubble, vertically. In this paper, we propose a newly developed correction method, a pre-signal threshold method for the S-TOP bubble measurement. Then, we demonstrate the effectiveness of the method empirically.

2. Single-Tip Optical fiber Probe (S-TOP)

2.1 Optics

The optics employed in this study is illustrated in Fig. 1. A Laser diode (1) (wavelength 635 nm) is

used for the light source of the S-TOP. The laser beams pass lens (3). The focused laser beams enter an optical fiber, and reach the S-TOP sensing tip (4). The laser beams reaching the tip surface are returned/emitted at/from the tip, depending on the Snell's law. The returned beams enter a photomultiplier (6) through a polarizer (5). Hence, we obtain electrical signals outputted from the photomultiplier. In succession, we analyzed the raw signals, and simultaneously obtained the velocities, diameters and the number density of the bubbles.

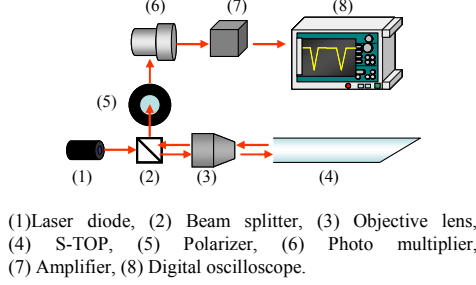


FIGURE 1 Optics.

2.2 Structure of the S-TOP

The schematic of the S-TOP employed in this study is shown in Fig. 2. The S-TOP is made from the optical fiber (synthetic quartz; step index type; the core diameter: 190 μm ; the clad thickness: 5 μm). The sensing tip is smoothly ground into a wedge-shape with an angle of 35 degrees. The fiber is fixed by the stainless capillary and the stainless tube

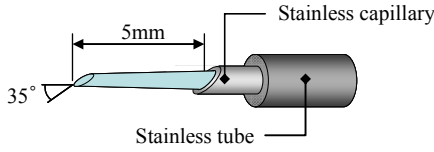


FIGURE 2 S-TOP configuration.

2.3 Signal processing of the S-TOP

Typical output signal delivered from the S-TOP in the single-bubble measurement (main signal) is shown in Fig. 3.

First, the output signals are smoothed by 25-points moving average.

Second, V_{Gas} (gas-phase output level) and V_{Liquid} (liquid-phase output level) are obtained using the histogram-method (Sakamoto and Saito, 2006).

Third, the high threshold level V_{thh} and the low threshold level V_{thl} are determined from the V_{Gas} and V_{Liquid} .

Finally, we obtain g_{rd} as the line of intersection of P_1 and P_2 ,

$$g_{rd} = \left(\frac{dV}{dt} \right) \frac{1}{(V_{Gas} - V_{Liquid})} \quad (1)$$

g_{rd} is proportional to the gas-liquid interface velocity. By using the α , a coefficient of the proportionality between the interface velocity and g_{rd} , U_b , the bubble velocity, is calculated from Eq. (2),

$$U_b = \alpha \cdot g_{rd} \quad (2)$$

through a beam splitter (2) and are focused by an objective lens (3). As a result, the bubble diameter is calculated from Eq. (3),

$$L_b = U_b \cdot (t_e - t_s) \quad (3)$$

where $(t_e - t_s)$ is the residence time of the S-TOP tip covered completely with the bubble. The event time, t_s (start time of S-TOP tip touching the bubble frontal surface) and t_e (end time of the S-TOP tip departures from the bubble at the bubble rear surface), is detected by using the thresholds, V_{Liquid} , and V_{Gas} .

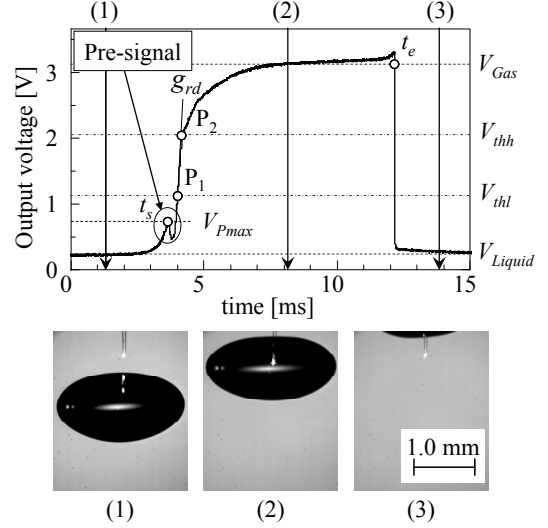


FIGURE 3 Signal processing of the S-TOP.

3. Pre-signal Threshold Method

3.1 Properties of the pre-signal

A temporal peak occurs just before the main signal. We call this ‘‘a pre-signal’’. The pre-signal is caused by the surface reflection on the bubble; the discharged beams from the S-TOP are reflected at the bubble frontal surface. It appears intensively, only when the tip shapes wedge. Its intensity is the largest of all conditions, when the S-TOP touches the center region of the bubble. This is attributed to the touch-angle (ϕ [degree]) between the S-TOP and the bubble surface (Fig. 4).

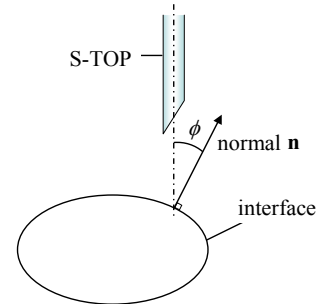
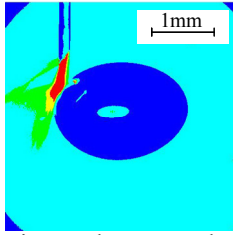


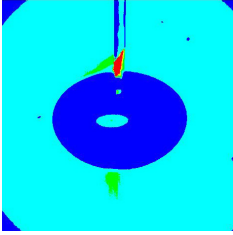
FIGURE 4 Touch-angle between the S-TOP and the bubble.

When the S-TOP touches the center region of the bubble, the ϕ is small, and the reflected beams at the bubble surface re-enter the S-TOP tip: the pre-signal appears strongly. On the other hand, when the S-TOP touches the outer edge of the

bubble, the ϕ is large, and the reflected beams are head to the other direction of the S-TOP axis: the pre-signal becomes very feeble. Fig. 5 clearly indicates this tendency.



(a) The S-TOP pierces the outer edge of the bubble.

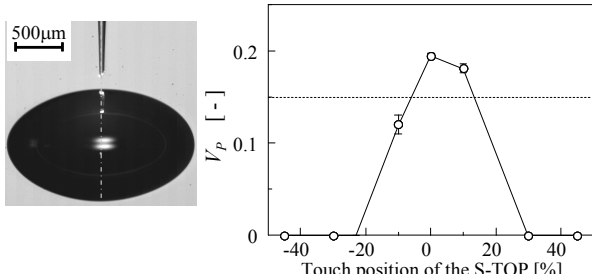


(b) The S-TOP pierces the center of the bubble.

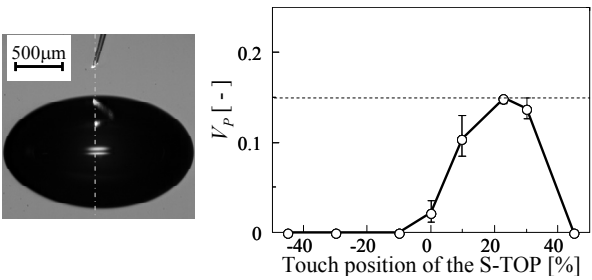
FIGURE 5 Visualization of the discharged beams from the S-TOP tip (pseudo-colored images: the red color means bright, the blue color means dark).

3.2 Pre-signal threshold method

Fig. 6 is some of the results, the relationship between the touch position/angle and the pre-signal intensity, V_p .



(a) The S-TOP pierces the bubble, vertically.



(b) The S-TOP pierces the bubble, tilting by 15 degrees.

FIGURE 6. Comparison of output voltage of the pre-signal

The touch position is defined L/L_m , where L is the distance from the minor axis of the bubble, L_m is the length of the major axis.

We already quantified the relationship in many touch conditions, and concluded that “the S-TOP touches the center

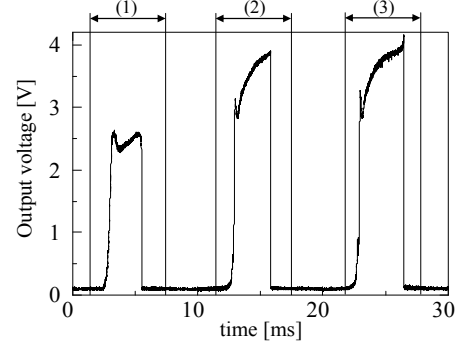
region of the bubble perpendicularly, when the V_p is larger than 0.15”.

Based on this, we propose a pre-signal threshold method. The schematic view is illustrated in Fig. 7.

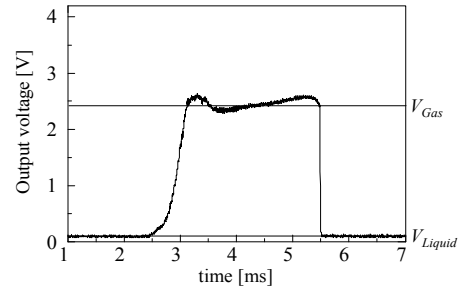
First, all signals delivered from the S-TOP is obtained.

Second, we extract main signals when V_p exceeds 0.15.

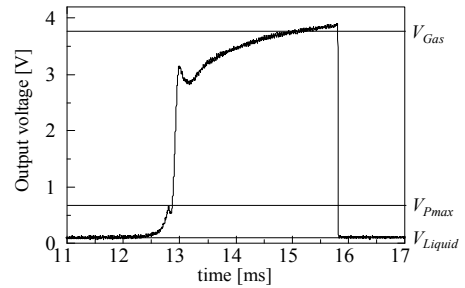
At last, we bring out the velocity and the diameter of the bubble, only by using the extracted signals.



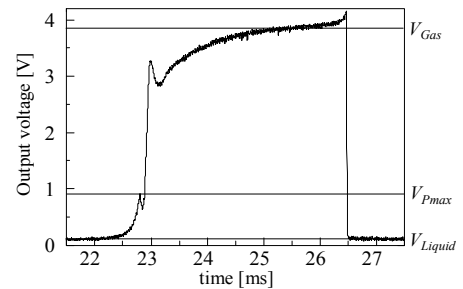
(a) Examples of signals delivered from the S-TOP.



(b) Signal 1 (Pre-signal does not occur).



(c) Signal 2, $V_p=0.13$ (<0.15) ($V_{Gas}=3.70$ [V], $V_{Liquid}=0.10$ [V], $V_{Pmax}=0.60$ [V])



(d) Signal 3, $V_p=0.21$ (>0.15) ($V_{Gas}=3.85$ [V], $V_{Liquid}=0.10$ [V], $V_{Pmax}=0.9$ [V])

FIGURE 7 Schematic of the pre-signal threshold method.

According to this, we can clearly identify the S-TOP-bubble interaction.

In Fig. 7 (b), signal 1 is obtained when the S-TOP pierces the outer region of the bubble: the pre-signal does not appear. Due to the incomplete penetration of the S-TOP tip into the bubble, V_{gas} becomes instable. As a matter of course, this signal is not suit to the S-TOP measurement.

In Fig. 7 (c), signal 2 is obtained when the S-TOP touches the halfway region of the bubble with some touch-angles: the feeble pre-signal appears. The piercing seems to be complete and successful; however, signal 2 is an inappropriate to the S-TOP measurement. V_p in signal 2 is about 0.13. From Fig. 6, it indicates that the S-TOP has touched the bubble within 20% to 40%.

These signals incur miscalculations of the bubble properties; hence, we shall remove them.

In Fig. 7 (d), signal 3 is obtained when the S-TOP touches the center region of the bubble, vertically: the intensive pre-signal comes out, whose V_p is about 0.21. This is what we have to extract.

Thus, we can choose only the desirable signals by using pre-signal. The effectiveness of the pre-signal method is discussed below.

4. Experiment

We examine the bubbles in a bubbly flow by using the S-TOP. The experimental setup is illustrated in Fig. 8. The vessel is made of an acrylic pipe (149 mm in inner diameter and 600 mm in height) covered with a rectangular acrylic water jacket to remove refraction and deformation of the image. The bubble swarms are grown and launched from hypodermic needles (0.40 mm in inner diameter); using a bubble launch device (Saito et al, 2010) that forms repeatedly uniform bubbles at controllable launch timing. The device consists of a function generator and audio speakers. The bubble launch interval is arbitrarily controlled by function generator. The high-speed video camera is settled at the front of the vessel, and visualizes the bubbles. The S-TOP is placed above the needles.

Thus, we make the uniform-size bubbles touch the S-TOP with various orientations. We calculate the bubble properties from the results of the visualization, the S-TOP raw data, and the S-TOP data processed by the pre-signal method. And then, the results are compared with each other.

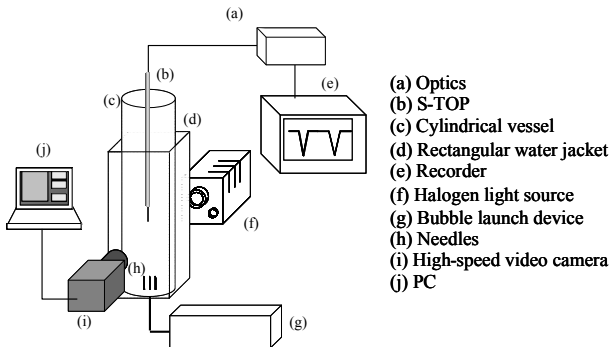


FIGURE 8. Experimental setup.

5. Results and Discussion

5.1 Velocity measurement result

The results of the velocity measurements are shown in Fig. 9. These figures evince the effectiveness of the pre-signal method. In Fig. 9, the white bar indicates P.D.F obtained from the visualization. The dashed lines are the results from the S-TOP (unprocessed by the pre-signal method). The measurement results are summarized in Table 1. The P.D.F of the visualization takes a peak only at 300 mm/s, while that of the S-TOP (unprocessed) is broad. The average velocity from the visualization is 295 mm/s, while that of the S-TOP (unprocessed) is 258 mm/s. The difference in the average velocities is about -13 %. These are caused by counting signals of incomplete piercing of the S-TOP; i.e. the S-TOP touches the edge area of the bubbles and the S-TOP scratches the bubbles; however, it is very difficult to distinguish the situation of the S-TOP touching a bubble; hence, usual signal processing cannot eliminate the unpleasant signals. As a result, the values of the S-TOP (unprocessed) have a widespread distribution.

In order to solve this serious problem in data processing, we employed the newly developed pre-signal method for processing of the raw S-TOP signals. The solid line, in Fig. 8, represents P.D.F of the velocity obtained from the S-TOP (processed by the pre-signal method).

Obviously, the degree of precision of the S-TOP is significantly improved. Further, the average velocity is 319 mm/s; hence, the difference between the visualization and the S-TOP result is also reduced to 8 %.

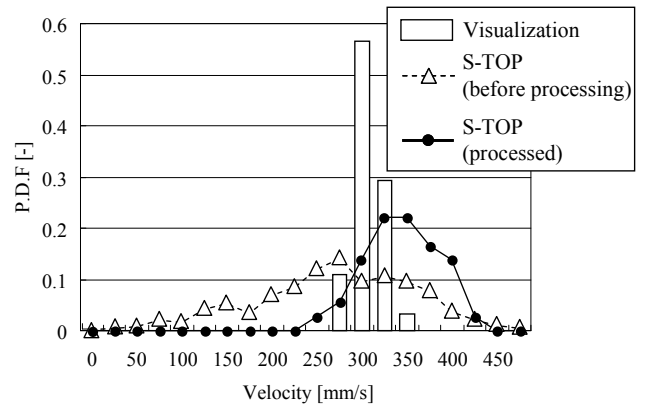


FIGURE 9. Velocity measurement results.

TABLE 1. Velocity measurement results

(a) Visualization vs. S-TOP (unprocessed)

Visualization [mm/s]	S-TOP (unprocessed) [mm/s]	Difference [%]
295	258	-13

(b) Visualization vs. S-TOP (processed)

Visualization [mm/s]	S-TOP (processed) [mm/s]	Difference [%]
295	319	8

5.2 Chord length measurement result

Fig. 10 shows the differences of the chord length between the visualization and the S-TOP (unprocessed/processed). Each average value is listed in Table 2. The pre-signal method remarkably improved the accuracy of the chord length measurement, because the method successfully removed the needless signals. The difference in the results of the visualization and S-TOP was significantly decreased from -42% to -21%.

In particular, it is obvious that the P.D.F of the visualization and that of the S-TOP (processed) are very similar. That is, the precision of the S-TOP measurement is greatly improved. Previously, the OFP measurement is only able to measure whole bubbles “statistically”, due to the problem of the measurement uncertainty.

By contrast, our OFP technique is able to probe the bubbles “individually”. Although the difference between the S-TOP results and the visualization results remains, these are bias errors.

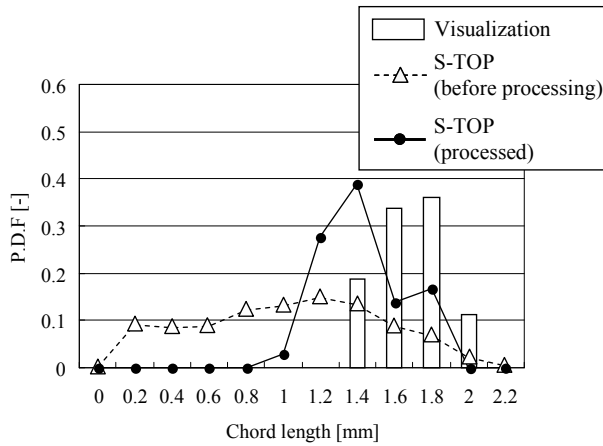


FIGURE 10. Chord length measurement results.

TABLE 2. Chord length measurement results.

(a) Visualization vs. S-TOP (unprocessed).

Visualization [mm]	S-TOP (unprocessed) [mm]	Difference [%]
1.59	0.93	-42

(b) Visualization vs. S-TOP (processed).

Visualization [mm]	S-TOP (processed) [mm/s]	Difference [%]
1.59	1.25	-21

6. Conclusions

The OFP measurements, particularly the S-TOP, include the inevitable problem; the touch positions between the OFP and the bubbles. This problem causes that the accuracy of the OFP measurement declines, and is a longtime issue for the OFP researchers. To overcome this difficulty, we focus on the

tip shape of the OFP, the wedge-shape tip. The S-TOP with wedge-shape tip has latency, to proofread its measurement accuracy. That is the pre-signal. It peaks when the S-TOP touches the center of the bubble. By using this phenomenon, we establish the pre-signal threshold method. Finally, it is found that this method greatly improve the measurement accuracy of the S-TOP. As for the bubble chord length measurement, the difference of the results between the visualization and the S-TOP is remarkably improved from -42% to -21%. The pre-signal method is not only simple but also powerful to process the OFP signals.

7. Nomenclature

- g_{rd} = gradient from water to air in the signals (/s)
- U_b = bubble velocity (m/s)
- L_b = piercing chord length of the bubbles (m)
- L = distance between the bubble center and the S-TOP (m)
- L_m = half length of the bubble major axis (m)
- t_s = time which the S-TOP starts touching the bubbles (s)
- t_e = time which the S-TOP's contact ends (s)
- V_{Pmax} = largest value in each pre-signal (V)
- V_P = normalized value of the pre-signal (-)
- V_{gas}, V_{liquid} = voltage which indicates that S-TOP tip is in the bubble and water (V)
- V_{thb}, V_{thl} = voltage as a threshold (V)
- Greek letters*
- α = coefficient of the proportionality between the interface velocity and g_{rd} (m)
- ϕ = touch-angle between the S-TOP and the bubble surface (degree)

8. Reference

- Brücker, C. 1999 “Structure and dynamics of the wake of bubbles and its relevance for bubble injection” *Physics of fluids*, Vol. 11, pp. 1781-1796.
- Ortiz-Villafuerte, J. , Schmidl, W. D., Hassan, Y. A. 2000 “Three-dimensional PTV study of the surrounding flow and wake of a bubble rising in a stagnant liquid” *Experiments in fluids*, Vol. 29, Supplement 1, S202-S210.
- Miller, N. & Mitchie, R. E. 1970 “Measurement of local voidage in liquid/gas 2-phase flow systems using a universal probe” *J. Brit. Nucl. Energy Soc.*, Vol. 2, pp. 94-100.
- Abuaf, N., Jones, O. C. Jr., Zimmer, A. 1978 “Optical probe for local void fraction and interface velocity measurements” *Rev. Sci. Instrum.*, Vol. 49, pp. 1090-1094.
- Cartellier, A. 1990 “Optical probes for local void fraction measurements; characterization of performance” *Rev. Sci. Instrum.*, Vol. 61, pp. 874-886.
- Mudde, R. F. & Saito, T. 2001 “Similarities between bubble column and pipe flow” *J. Fluid Mech.*, Vol. 437, pp. 203-228.
- Higuchi, M., & Saito, T. 2010 “Quantitative characterizations of long-period fluctuations in a large-diameter bubble column based on point-wise void fraction measurements” *Chem. Eng. J.*, Vol. 160, pp. 284-292.
- Saito T. 2000 Japanese patent, No. 3018178.

- Matsuda, K., Ozawa, Y., Oishi, S., Aoshima, S., Saito, T. 2009 "Measurement of surface tension using a Single-Tip Optical fiber Probe (S-TOP)" *The review of laser engineering*, Vol. 37, pp. 528-534.
- Ozawa, Y., Sanada, T., Oishi, S., Aoshima, S., Saito, T. 2009 "Measurement technique of micro-droplets using an Optical Fiber Probe" *The review of laser engineering*, Vol. 37, pp. 535-539.
- Saito, T., Matsuda, K., Ozawa, Y., Oishi, S., Aoshima, S. 2009 "Measurement of micro-droplets using a newly developed optical fibre probe microfabricated by femtosecond pulse laser" *Measure. Sci. Tech.*, Vol. 20, pp. 114002.
- Clark, N. N. & Turton, R. 1988 "Chord length distributions related to bubble size distributions in multiphase flows" *Int. J. Multiphase Flow*, Vol. 14, pp. 413-424.
- Liu, W. & Clark, N. N. 1998 "Relationship between Bubble Size Distributions and Chord Length Distribution in Heterogeneously Bubbling Systems" *Chem. Eng. Sci.*, Vol. 53, pp. 1267-1276.
- Mizushima Y. & Saito T. 2011 "A Discrimination Method of Touched Positions by Using A Pre-Signal in Bubble Measurement with An Optical Fiber Probe". *The review of laser engineering*, Vol. 39, pp. 528-534.
- Saito, T. Sakakibara, K., Miyamoto, Y., Yamada, M. 2010 "A study of surfactant effects on the liquid-phase motion around a zigzagging-ascent bubble using a recursive cross correlation PIV" *Chem. Eng., J.*, Vol. 158, pp. 39-50.

Compartmentalization of forces at an acoustic cavitation bubble by numerical simulation and by visualization of sonoluminescence

Taikan Mori

Graduate School of Engineering,
 Shizuoka University
 Hamamatsu, Shizuoka, Japan

Takayuki Saito

Graduate School of Science and Technology,
 Shizuoka University
 Hamamatsu, Shizuoka, Japan

Keywords: Acoustic cavitation, Sonoluminescence, Bjerknes force

Abstract: Forces (gravity force, buoyancy force, drag force, added mass force, history force, primary Bjerknes force, secondary Bjerknes force) at an acoustic cavitation bubble are compartmentalized by numerical simulation and by visualization of sonoluminescence. Numerical simulation is employed Runge-Kutta-Fehlberg method and bubble velocity and the forces are calculated. In contrast, sonoluminescence is visualized by I.I. unit (ICCD). In this study, in order to compartmentalize the 7 forces, the bubble rising velocity is calculated by numerical simulation and by image analysis. On the numerical simulation, a bubble terminal velocity in static fluid is 1.2 mm/s. In contrast, a bubble velocity calculated by visualization of sonoluminescence is faster than the velocity. Then, the dominant of force at an acoustic cavitation bubble is acoustic radiation force (primary Bjerknes force and secondary Bjerknes force). In the future study, we will compartmentalize the forces by relating with the results of numerical simulation and image analysis.

1. Introduction

Cavitation is phenomenon of phase transition from liquid phase to gas phase. Cavitation generates on a surface on pumps and screws and it is disputed as erosion at the impeller. However, processing and cleaning techniques applied cavitation are developed in industry. Especially, cavitation which generated by radiating acoustic in liquid is applied in cleaning and chemical fields.

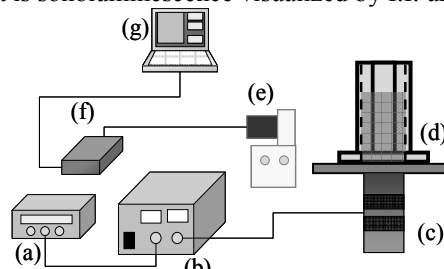
Acoustic cavitation bubbles which generated by acoustic expand and contract in synchronization with period of acoustic. Furthermore, the bubble is collapsed by rapid compression. At this time, the bubble radiates faint light and this phenomenon is called sonoluminescence. In the past study, it is reported that a profile of acoustic cavitation bubbles correlates strongly with a profile of sonoluminescence.

The acoustic cavitation bubble motion is forced on 7 forces (gravity force, buoyancy force, drag force, added mass forces, history force, primary Bjerknes force, and secondary Bjerknes force). Primary and secondary Bjerknes force is force by acoustic radiation pressure. In this study, forces at an acoustic cavitation bubble are compartmentalized by numerical simulation and by image analysis. Numerical simulation employs Runge-Kutta-Fehlberg method. In contrast, the genesis location of sonoluminescence is assumed the genesis location of acoustic cavitation bubble, and multi-bubble sonoluminescence (MBSL) is visualized. The primary Bjerknes force is calculated by analyzing the image.

2. Experimental setup

Fig. 1 shows a schematic diagram of an experimental setup to visualize MBSL. Acoustic is generated by bolt-clamped Langevin type transducer. The transducer is driven by the output voltage signal from function generator amplified by high output amplifier. The experimental parameters are listed in Tab. 1. To visualize with a high accuracy, an acrylic vessel, outer wall is right octagon and inner wall is round, is applied in experiment. The liquid which

is applied in experiment is ultrapure water made by ultrapure water production equipment (Millipore). Sonoluminescence is visualized by Image Intensifier unit (C9546, Hamamatsu Photonics K.K.). Furthermore, the signal from I.I. unit is recorded in PC through camera adaptor. To calculate bubble rising velocity by image analysis, the vertical sectional image of sonoluminescence is visualized by I.I. unit. Fig. 2 shows the vertical sectional image of MBSL visualized by I.I. unit. The white part is sonoluminescence visualized by I.I. unit.



(a)Function generator, (b)Power amplifier, (c)BLT, (d)Water Vessel, (e)Image Intensifier unit, (f)Camera adaptor, (g)PC

FIGURE 1. Schematic diagram of experimental setup.

TABLE 1. Experimental parameters.

Voltage [mV]	Frequency [kHz]	Volume [ml]
630	20	200
Exposure time [ms]	Resolution [$\mu\text{m}/\text{pixel}$]	
16.7	75.2	

3. Numerical simulation

We will consider the motion equation of acoustic bubble as follows:

$$m_b \frac{du_b}{dt} = F_G + F_B + F_D + F_{AM} + F_H + F_{PBF} + F_{SBF} \quad (1)$$

where m_b is the mass of a bubble, u_b the rising velocity of a bubble, F_G the gravity force, F_B the buoyancy force, F_D the drag force, F_{AM} the added mass force, F_H the history force, F_{PBF} the primary Bjerknes force, F_{SBF} the secondary Bjerknes force. In this study, the primary Bjerknes force and the secondary Bjerknes force aren't considered. The rising velocity of spherical bubble in static fluid is calculated. Runge-Kutta-Fehlberg method is applied to numerical simulation. The parameters of the numerical simulation are listed in Tab. 2.

TABLE 2 Parameters of numerical simulation.

Bubble diameter [μm]	Kinetic viscosity [m^2/s]	Density of water [kg/m^3]
57.3	1.307×10^{-6}	999.69

4. Image analysis

Fig. 3 shows the algorithm for image analysis. We consider the motion of MBSL in one dimension. The brightness wave is formed by the fluctuation of brightness in one dimension. The rising velocity of sonoluminescence is calculated by analyzing the time series waves. This velocity assumes the rising velocity of an acoustic cavitation bubble.

5. Results and discussion

Fig. 4 shows the results of numerical simulation and image analysis. The terminal velocity calculated by numerical simulation is 1.2 mm/s. In contrast, the velocity calculated by image analysis is faster than the terminal velocity. Then, an acoustic cavitation bubble is strongly forced on Bjerknes forces (primary Bjerknes force and secondary Bjerknes force). The primary Bjerknes force on the bubble is expressed below.

$$F_{PBF} = - \langle V \nabla P \rangle \quad (2)$$

where V is a bubble volume, ∇P is a pressure gradient and the bracket $\langle \rangle$ indicates the average over a cycle. In contrast, the secondary Bjerknes force on the bubble is expressed below.

$$F_{SBF} = - \frac{\rho_w}{4\pi d^2} \frac{dV_1}{dt} \frac{dV_2}{dt} \quad (3)$$

where ρ_w is density of water, d is distance between two bubbles. This force is generated by acoustic wave generated from two oscillating bubbles. This force depends on the distance between two bubbles. Hence, if the distance is shorter, the secondary Bjerknes force increases and the bubble velocity is faster.

The bubble rising velocities calculated by visualization of sonoluminescence is 4~500 mm/s. This is because the primary/secondary Bjerknes force forces on a bubble. The primary Bjerknes force depends on the pressure gradient. In addition, the pressure P depends on position in the standing wave. Hence, in the case of one dimension, pressure is expressed as $P(z)$ and the primary Bjerknes force is expressed as $F_{PBF}(z)$. Furthermore, a bubble position in the standing wave z depends on time. Then, a bubble position in the standing wave is expressed as $z(t)$. In the future study, we will model $z(t)$ and calculate the primary Bjerknes force by numerical simulation.

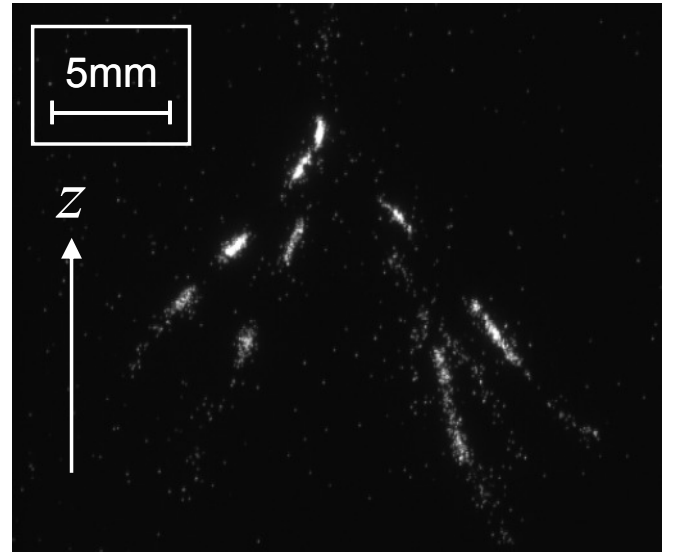


FIGURE 2. MBSL image visualized by I.I. unit.

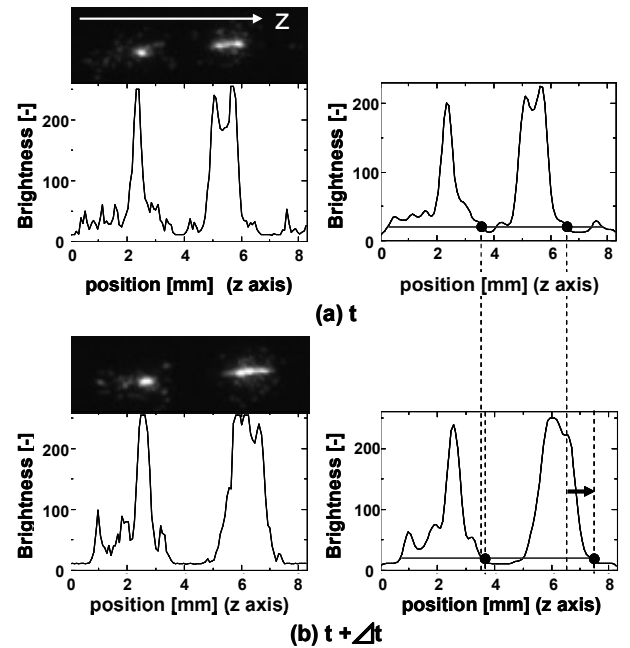


FIGURE 3. The algorithm for image analysis.

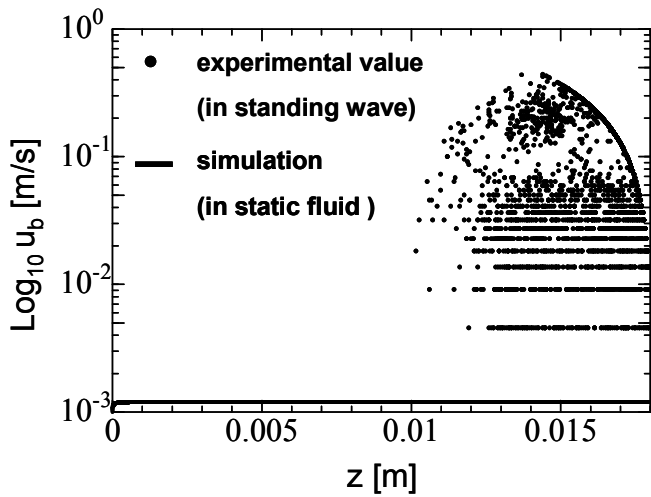


FIGURE 4. The rising velocity of a bubble calculated by numerical simulation and by image analysis

6. Conclusions

In this study, forces at an acoustic cavitation bubble are compartmentalized by numerical simulation and by visualization of sonoluminescence. The bubble rising velocity calculated by image analysis is faster than the terminal velocity in static fluid. This is because the bubble is forced by acoustic radiation forces (primary Bjerknes force and secondary Bjerknes force). In the future study, we will compartmentalize the forces by relating with the results of numerical simulation and image analysis.

7. References

- W. Lauterborn et al, 2007, "Acoustic cavitation, bubble dynamics and sonoluminescence" *Ultraso. Sonochem.*, Vol. 14, 484-491.
- T. Saito, T. Kajishima, F.Kiyono & T. Usami, 1993, "Particle Velocity in the Main Stream Direction of Solid-Liquid Two-Phase Flows in a Swaying Pipe" *Trans. Jpn. Soc. Mech. Eng. (B)*, Vol. 59, Issue 563, pp. 29-34.
- Sueung-Man Yang & L .G. Leal, 1991, "A note on memory-integral contributions to the force on an accelerating spherical drop at low Reynolds number" *Phys. Fluids*, Vol. 3, pp. 1822-1824.
- R. Mei, 1994, "A note on the history force on a spherical bubble at finite Reynolds number" *Phys. Fluids*, Vol. 6, pp. 418-420.
- H. Mitome, 2001, "Micro Bubble and Sonoluminescence" *Jpn. J. Appl. Phys.*, Vol. 40, pp. 3484-3487.

Relations of Void Fractions and Liquid Motions to Dissolved Gas Concentrations in a Large-Diameter Bubble Column

Masahiro Yamada

Graduate school of Engineering, Shizuoka University,
 3-5-1 Johoku, Naka-ku, Hamamatsu, Shizuoka,
 Japan

Takayuki Saito

Graduate school of Science and Technology, Shizuoka University,
 3-5-1 Johoku, Naka-ku, Hamamatsu, Shizuoka,
 Japan

Keywords: Photoelectric optical fiber probe, LDV, Mass transfer, Flow structure.

Abstract: We investigated correlations between the CO₂ concentration transportation and the large-scale flow structure by using a newly developed photoelectric optical fiber probe (POFP) and LDV. The POFP simultaneously measures the bubble characteristics and the CO₂ concentration. Based on the fluctuation characteristics of the void fractions, the flow field in the bubble column was divided into three zones by height. We focused on the spatial cross-correlation coefficient and a thinking of integral length scale in each zone. The integral-length-like scale of the liquid phase motions indicated few change against the height. On the other hand, the similar length scale of the void fraction becomes small toward the upper zone. The similar length scale of the CO₂ concentration exists up to the height of the middle zone. Based on these results, we discuss the relations of spatial-scale of the void fraction and the liquid motion to the CO₂ concentration.

1. Introduction

Gas-liquid two-phase flows are encountered in various industrial plants, such as chemical reactors, bioreactors, and so on. For the purpose of saving energy and improving operation security, the high efficiency of the gas absorption has been strongly demanded in various fields. Hence, we need to clarify the relations between mass transfer mechanism (Komori *et al.*, 1990) and structure of the bubbly flow (Mudde and Saito, 2001). In the past research, Akita and Yoshida indicated the effects of the liquid properties on the gas holdup and the volumetric coefficient for liquid phase mass transfer (Akita and Yoshida, 1973). However, a relationship of the local fluctuation of the liquid-phase motion and the void-fraction to the CO₂ concentration transportation has not been discussed. As the major problem, although there are some devices for detecting the concentration (Maceiras *et al.*, 2008) or bubble characteristics (Mudde and Saito, 2001), there was no instrument to enable the simultaneous measurement.

Thus, we newly developed a photoelectric optical fiber probe (POFP) in order to solve this difficult problem (Hanyu and Saito, 2010). The POFP has two functions of an optical fiber probe and an electric sensor. The optical fiber probe and the electric sensor measures bubble characteristics and concentration, respectively; i.e. we are able to simultaneously obtain the bubble diameter, velocity, time-series void fraction and the CO₂ concentration dissolved in the liquid around the bubbles. Therefore, the new photoelectric optical fiber probe enables researchers to simultaneously measure both mass transfer and the flow structure at the same point in the bubble column. Moreover, we measured the velocities of the liquid phase at the same point by using the laser Doppler velocimetry (LDV).

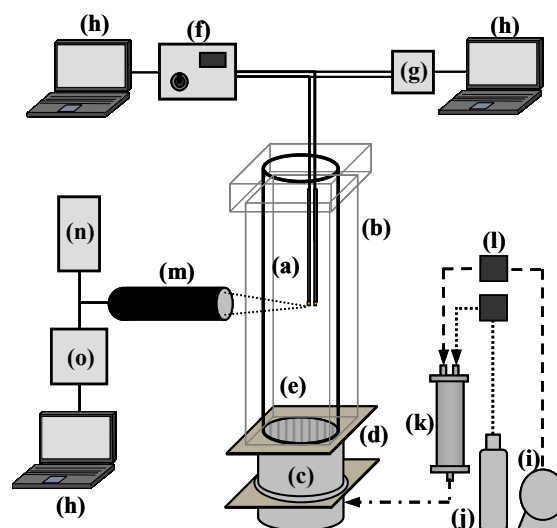
In the present study, we discuss the relations of spatial-scale of the void fraction and the liquid motion to the CO₂ concentration. Therefore, we introduced the thinking of the integral length scale to extract a spatial-scale which has

the similar characteristics. Firstly we calculated the integral-length-like scale for extracting a size of a fluid body. Secondly we adopted a similar way of thinking into a consideration of the length scale to the void fraction and CO₂ concentration in order to evaluate spatial-scale. Finally we discuss the relations of spatial-scale of the void fraction and the liquid motion to the CO₂ concentration from these results.

2. Experimental

2.1 Bubble column

A schematic diagram of the experimental setup employed



(a) Bubble column, (b) Water jacket, (c) Air chamber, (d) Perforated plate, (e) Photoelectric Optical Fiber Probe, (f) Differential amplifier circuit, (g) Optical system, (h) PC, (i) Air compressor, (j) CO₂ gas cylinder, (k) Gas mixer, (l) Mass flow controller, (m) LDV probe, (n) Argon ion laser, (o) LDV measurement unit

FIGURE 1. Experimental setup.

in the present study is shown in Fig. 1. An acrylic bubble column of 380 mm in inner diameter and 1500 mm in height was employed. The bubble column is covered with an acrylic water jacket of 440 mm × 440 mm in square cross section and 1605 mm in height. Both the bubble column and the water jacket were filled with the ion-exchanged water and the degassed tap water, respectively. An air chamber (380 mm in diameter and 200 mm in height) and a perforated plate (diameter of pores: 1.0 mm; equilateral triangular pitch: 10 mm; the number of pores: 1240) were installed at the bottom of the bubble column. A mixture gas of CO₂ and pure air was pumped into the bubble column through them. We adjusted the composition of the mixture gas (1.8×10^{-5} kg/s of CO₂ and 9.7×10^{-4} kg/s of pure air) by using two mass flow controllers. A LDV measurement unit and LDV probe was used for measurement of the liquid motion.

2.2 Measurement points

In this study, we discuss the relations of spatial-scale of the void fraction and the liquid motion to the CO₂ concentration. We focused on the spatial-scale of radial direction at three zones ($z = 300\text{mm}, 700\text{mm}, 1200\text{mm}$). Hence, we simultaneously measured the center of the horizontal section of the bubble column as well as the mobile point to radial direction at each zone.

2.3 Photoelectric optical fiber probe (POFP)

We have newly developed a Photoelectric Optical Fiber Probe (POFP). The POFP has two functions of a concentration measurement by an electric probe (Maceiras, 2007) and a bubble measurement by an optical fiber probe (Mudde and Saito, 2001) (Saito et al., 2009); i.e. we are able to measure the mass transfer and the void fraction simultaneously by a pair of the POFPs. The structure of the POFP is illustrated in Fig. 2. It is made of a quartz optical fiber (external diameter: 230 μm, core diameter: 190 μm, clad thickness: 5 μm, jacket thickness: 15 μm) plated with nickel (SEK-797, Japan Kanigen Co., Ltd.) and platinum. The plating thickness of nickel and platinum are 130 μm and 5 μm, respectively. The plated area of the POFP is an electric sensor, and the tips are an optical fiber probe. A micrograph of this sensor is shown in Fig. 3. The external diameter of the POFP is 500 μm. The axial distance L_P and the clearance R_P between the probes are 1.2 mm and 500 μm, respectively. The tips of the POFP are wedge shaped, with a 35 degree wedge angle.

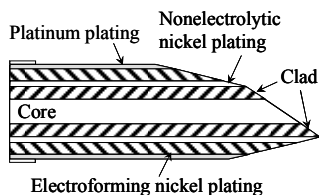


FIGURE 2. Structure of the POFP.

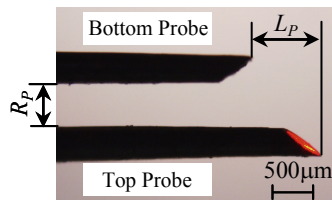


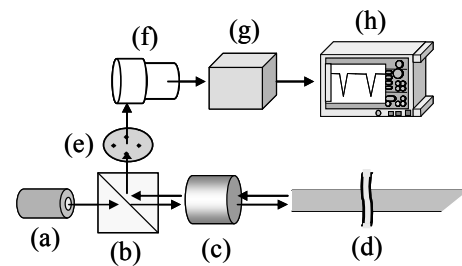
FIGURE 3. Micrograph of the POFP.

2.4 Principle of the optical fiber probe

The optical fiber probe of the POFP utilizes the differences in refractive indexes of gas/liquid phases and optical fiber. The system for the optical sensor is shown in Fig. 4. The laser

beams from a laser diode go straight through a beam splitter, and are focused on the incident tip of the optical fiber through an objective lens. Some of the beams reaching the wedge-shape tip are reflected at the tip surface, and subsequently return into the same fiber. Some of the returned beams input into a photomultiplier through a beam splitter and a polarizer. The output signal obtained from the photomultiplier is recorded at a PC via an A/D converter.

When the tip of the optical sensor is positioned in a gas phase, the amount of the returned beams is larger than that in a liquid phase. As a result, the output voltage becomes high level. On the other hand, when the POFP is positioned in a liquid phase, most of the beams are emitted into the liquid phase. Hence the output voltage becomes low level. We can easily distinguish a change in gas/liquid phases by the difference of the recorded output voltage.

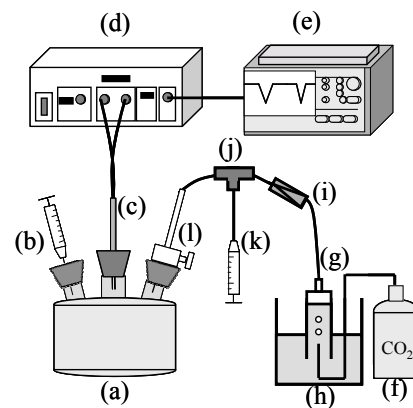


(a) Laser diode, (b) Beam splitter, (c) Objective lens, (d) Optical Fiber Probe, (e) Polarizer, (f) Photomultiplier, (g) A/D converter, (h) Recorder

FIGURE 4. Optical system of the optical fiber probe.

2.5 Principle of the electric sensor, and calibration

By using the function of the electric sensor, we are able to measure local CO₂ concentration indirectly. This concentration measurement utilizes electric conductivity depending on the amount of CO₂ dissolution. An electric differential amplifier circuit was employed to detect the electric conductivity as an output voltage which depends on the amount of dissolved CO₂. To obtain the CO₂



(a) Flask, (b) Syringe, (c) Photoelectric Optical Fiber Probe, (d) Differential amplifier circuit, (e) Recorder, (f) CO₂ cylinder, (g) Cylinder, (h) Beaker, (i) Check valve, (j) Three-way valve, (k) Syringe, (l) Two-way valve

FIGURE 5. Schematic diagram for calibration of the electric probe.

concentration from the output voltage, we preliminarily obtained the relationships between output voltage and CO₂ concentration at some solution temperatures. For this specific purpose, we conducted an experiment for making calibration curves between the CO₂ concentration and the output voltage. The CO₂ solubility depends strongly on the liquid temperature. Therefore, we made the calibration curves with great attention paid to the liquid temperature. Some calibration curves against several temperatures were obtained. The schematic diagram to make the calibration curves is illustrated in Fig. 5. First, a flask (a) was fully filled with ion-exchanged and degassed water. Second, CO₂ gas collected in a cylinder (g) placed in a vessel filled with ion-exchanged and degassed water by downward displacement of the water was suctioned into a precision syringe (k). The CO₂ gas was dissolved in the ion-exchanged water in the flask (a) by mixing with a stirrer chip. During this process, a pressure inside the flask is kept equal to the atmospheric pressure by a syringe (b). Finally, after 5 minutes mixing, the CO₂ gas undissolved in the water was pumped out by using the syringe (k). Then, we calculated the amount of CO₂ dissolution from the relationship between injected amount and recovered amount. We obtained the calibration curves from both the amount of the dissolved CO₂ and the output voltage.

3. Signal analysis

3.1 Processing of the optical fiber probe signals

We employed a method to extract the long-period fluctuations formed in a bubble column from time-series point-wise void fractions (Higuchi and Saito, 2010). Fig.6 shows an outline of the time-series raw data obtained from the optical fiber probe. We analyzed a time-average void fraction at the same time interval T_L . The local time-series void fraction $\alpha(t)$ was calculated by the following equation;

$$\alpha(t) = \frac{1}{T_i} \sum_{j=1}^N t_j \quad (i = 0,1,2,\dots,n) \quad (1)$$

t_i is the interval of time that the tip of the top probe existed in the gas phase.

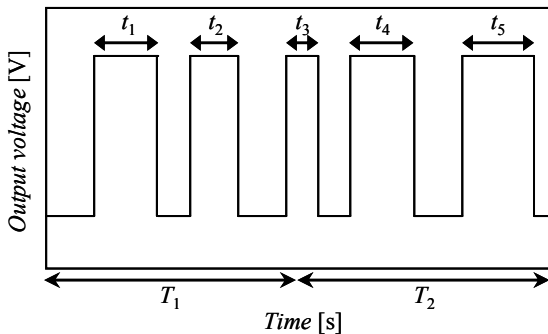


FIGURE 6. A typical signal of the optical fiber probe.

3.2 Processing of the electric sensor signals

The output signals from the electric probe of the POFD include three-type signals as shown in Fig. 7 (a). The first one is signals of the local CO₂ concentration, the second one is noises of the applied AC voltage, and the third is bubble noises. The bubble noises are sharp increases in the output signals owing to the sudden decreases of electric conductivity.

A raw signal of the electric probe is very noisy as shown in Fig. 7 (a). In order to obtain a time-series local CO₂ concentration, we need to remove the noises from the raw signals.

First, we processed the raw signal with FFT, and decided cutoff frequencies in order to remove applied AC component. Second, filtering the raw signal by a low-pass filter and transforming the processed signal by IFFT, we obtained the first-processed data (Fig. 7 (b)). Finally, we removed the bubble noises from the data by a median filter [6] (Fig.7 (c)). Before injection of the CO₂-mixture gas into the bubble column, the indicated value of the initial CO₂ concentration in the bubble column experiments is slightly different from that

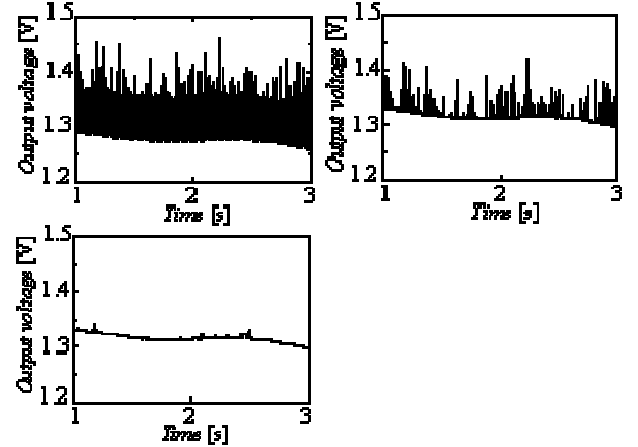


FIGURE 7. Processing of the electric sensor.

of the preliminary calibration (0 mol/m³). The difference of supplied water causes the above; ion-exchanged and degassed water was used in the calibration, while tap water was used in the bubble column experiments. Since the difference in the amount of initial dissolved ions resulted in the difference in the indicated value, we removed the difference as biased error.

3.3 Processing of the LDV data

In this study, we applied LDV to gas-liquid two-phase flows. Hence, we removed laser beam scattered from the bubble surfaces from the raw data by the following procedure (Higuchi and Saito, 2010). The mean μ and standard deviation σ are calculated from the raw data. The raw data was processed by applying $\mu \pm 3\sigma$, and almost the bubble-scattered noises were removed from the raw data. Since the processed data was intermittent, the velocity defects were interpolated by a liner interpolation method.

3.4 Integral-length-like scale

The integral length scale is usually employed for the evaluation of eddy scale in investigations of single-phase turbulent flows (H. Belmabrouk, M. Michard, 1998). The integral length scale is defined by the following equation;

$$L(x) = \int_0^{\infty} R(\Delta x) dx \quad (2)$$

$R(\Delta x)$ is the correlation coefficient and given by the following equation;

$$R(\Delta x) = \frac{1}{N} \sum \frac{[f(A) - f_{ave}(A)][f(A + \Delta x) - f_{ave}(A + \Delta x)]}{f_{rms}(A) \cdot f_{rms}(A + \Delta x)} \quad (3)$$

Δx is a distance between the fixed measurement point in the center of the horizontal section of the bubble column and the mobile point in the radial direction.

In this study, we introduced the thinking of the integral length scale to extract a spatial-scale which has the similar characteristics. We investigate spatial-scale of a liquid-phase motion, the void fraction and CO₂ concentration transportation by introducing the similar way. Firstly, we calculated the integral-length-like scale for extracting a size of a fluid body. Secondly, we calculated a similar length scale in order to evaluate spatial-scale of the bubble swarm and CO₂ concentration transportation.

4. Results and Discussion

4.1 Integral-length-like scale of the liquid-phase motion

Based on the fluctuation characteristics of the void fractions, the flow field in the bubble column was divided into three zones by height (Higuchi and Saito, 2010). Hence, we investigated the integral-length-like scale at three different height ($z=300\text{mm}$, 700mm , 1200mm). Fig.8 (a) shows the cross-correlation coefficient of the liquid-phase motion. The horizontal section) and the mobile point in the radial direction. The results of spatial-scale are summarized in Table 1. Few changes in the integral-length-like scale of the liquid-phase motion were observed against the height. The results indicate the liquid-phase flow has almost the same size body in the whole of the bubble column.

4.2 A similar length scale of the void fraction

Figure 8 (b) shows the results of the void fraction. The similar length scale of the void fraction decreases in the height direction. At the height of $z = 1200\text{mm}$, it was not calculated. In the bottom zone of the bubble column, the bubble swarms which have the similar characteristics of

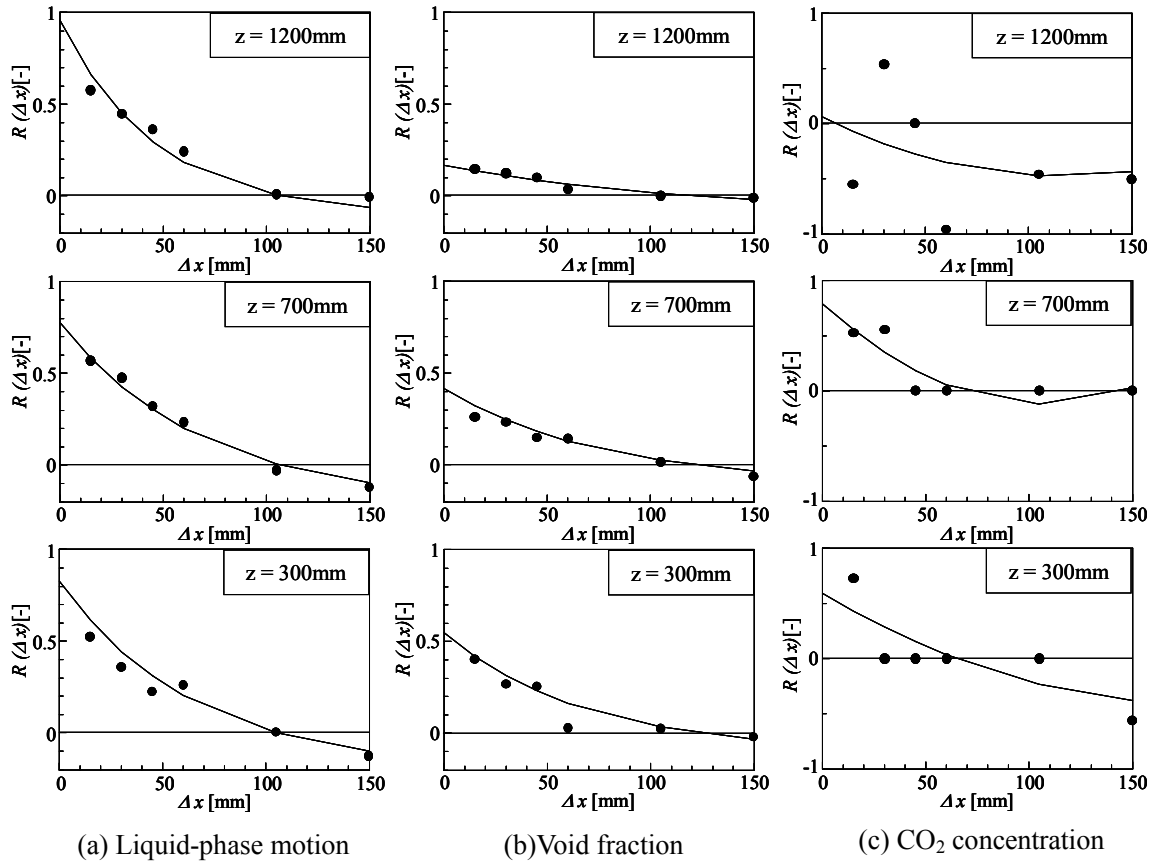


FIGURE 8. Cross-correlation coefficient.

TABLE 1. Integral-length-like scale.

	Liquid-phase motion	Void fraction	CO ₂ concentration
$z=1200\text{mm}$	37.3	23.8	21.5
$z=700\text{mm}$	36.7	7.6	28.8
$z=300\text{mm}$	38.1	-	-

relatively large size are formed. However, the bubble swarms become smaller in the height direction.

4.3 A similar length scale of the CO₂ concentration transportation

Figure 9 (c) shows the results of the CO₂ concentration transportation. The similar length scale was not calculated at $z = 1200\text{mm}$. However, we consider that CO₂ concentration transportation has a relationship with the size of characteristics liquid-phase flow up to the middle zone ($z = 700\text{mm}$).

From these results, in the bottom zone of the bubble column, the bubble swarms which have the similar characteristics are formed, and the bubble swarms are relatively large size. Hence, CO₂ concentration is transported by liquid-phase motion around the bubble swarm. In the middle zone, the bubble swarms become smaller than the bottom zone. However, CO₂ concentration is transported by the characteristics liquid-phase flow. On the other hand, in the upper zone of the bubble column, the bubbles are dispersed. The dissolved CO₂ gas is diffused by liquid-phase motion. However, CO₂ concentration is not transported by the characteristics liquid-phase flow.

5. Conclusions

The relations of spatial-scale of the liquid-phase motion and the void fraction to the CO₂ concentration transportation were discussed. First, the liquid-phase flow has almost the same size body in the whole of the bubble column. Second, the bubble swarms become smaller in the height direction. CO₂ concentration was transported by the characteristics liquid-phase flow up to the middle zone of the bubble column.

6. References

- Higuchi, M. & Saito, T. 2010 Quantitative characterizations of long-period fluctuations in a large-diameter bubble column based on point-wise void fraction measurements, *Chem. Eng. J.*, Vol.160, pp. 284-292.
- Komori, S. et al. 1990 Mass Transfer into a Turbulent Liquid Across the Zero-Shear Gas-Liquid Interface, *AIChE. J.*, Vol. 36, pp. 957-960.
- Mudde, R. F., & Saito, T. 2001 Hydrodynamical similarities between bubble column and bubbly pipe flow, *J. Fluid Mech.*, Vol. 637, pp. 203-228.
- Akita, K., & Yoshida, F. 1973 Gas Holdup and Volumetric Mass Transfer Coefficient in Bubble Column, *Ind. Eng. Process Des. Develop.*, Vol. 12, pp. 76-80.
- Rocio, M. et al. 2008 Effect of bubble contamination on gas-liquid mass transfer coefficient on CO₂ absorption in amine solutions, *Chem. Eng. J.*, Vol. 137, pp. 422-427.
- Hanyu, K., & Saito, T. 2010 Dynamical Mass-Transfer Process of A CO₂ Bubble Measured by Using LIF/HPTS Visualization and Photoelectric Probing, *Can. J. Chem. Eng.*, Vol. 88, pp. 551-560.
- Maceiras, R. et al. 2004 Local mass transfer measurements in a bubble column using an electrochemical technique, *Chem. Eng. Process.*, Vol. 43, pp. 987-995.
- Saito, T. et al. 2009 Measurement of tiny droplets using a newly developed optical fiber probe micro-fabricated by a femtosecond pulse laser, *Meas. Sci. Technol.*, Vol. 20, pp. 1-12.
- Belmabrouk, H., & Michard, M. 1998 Taylor length scale measurement by laser Doppler velocimetry, *Experiments in Fluids*, Vol. 25, pp. 69-76.

Quantification of the measurement accuracy and structure optimization for a Two-Tip Optical fiber Probe in the bubble measurement

Ryosuke Motoyoshi
 Graduate School of Engineering,
 Shizuoka University
 Hamamatsu, Shizuoka, Japan

Takayuki Saito
 Graduate School of Science and technology,
 Shizuoka University
 Hamamatsu, Shizuoka, Japan

Keywords: Two-Tip Optical fiber Probe, bubble measurement, measurement accuracy, bubble deformation

Abstract: An optical fiber probe has been frequently employed to measure bubble diameters and velocities in gas-liquid two-phase systems. One of the common types for the bubble measurement is a Two-Tip Optical fiber Probe (T-TOP). However, due to its intruding, the affected motion of the bubbles inevitably declines the measurement accuracy. The magnitude of the bubble motion considerably depends on the T-TOP structure. Hence, the optimization for the T-TOP structure is needed for an accurate measurement. In this study, we arranged some types of the T-TOP size (L_p and R_p) and demonstrated which T-TOP sizes satisfy the bubble measurement with a high degree of accuracy. First, the bubbles deformation quantified in each condition by using the visualization. Second, we compared results of the visualization to that of the T-TOP for confirming the measurement accuracy of the T-TOP. Finally, optimal the T-TOP structure for the bubble measurement is defined.

1. Introduction

Gas-liquid two-phase flows are frequently encountered in the industrial plants such as electrical generating plants, chemical plants and so on. In order to realize higher efficiency and safer operation of these plants, it is essential to measure the characterization of bubbles accurately. One of the common tools for the gas-liquid two-phase flow measurement is an optical fiber probe (OFP). This method successfully measures the velocity, the chord length of the bubble, and the local void fraction even though in a high density of bubbles; however, due to its intruding, the bubbles largely deform when the OFP touches them. The affected motion of the bubbles inevitably reduces the OFP measurement accuracy. In this study, we improve the measurement accuracy of a Two-Tip Optical fiber Probe (T-TOP) in the bubble measurement. The optimization for the T-TOP structure is conducted. Finally, it is found that the optimized T-TOP structure minimizes the influence of touching the bubble, and measures the bubbles with a high degree of accuracy.

2. T-TOP

A schematic diagram of the T-TOP is shown in Fig. 1. The T-TOP is composed by silica glass (Diameter of a wire: 230 μ m, Diameter of core: 190 μ m, Thickness of clad: 5 μ m, Thickness of Jacket: 15 μ m). The T-TOP consists of two fibers whose tips shape wedge (the wedge angle is 35 degrees), and its structure is controlled by two parameters, R_p and L_p (T-TOP size). We arranged some types of the T-TOP size in terms of L_p , and demonstrated which T-TOP sizes satisfy the bubble measurement.

3. Experimental setup

A schematic diagram of the experimental setup is shown in Fig. 2. The vessel (f) is filled with the ion-exchanged water. Each bubble is injected from the hypodermic needle (g) (equivalent particle diameter = 2.99 mm). The T-TOP (a) is set on the 3-axis unit. The optical signal delivered from the

T-TOP that is obtained by the recorder (p). The interaction of the T-TOP with a bubble rising in the stagnant water is visualized by two high-speed video cameras (d), (e).

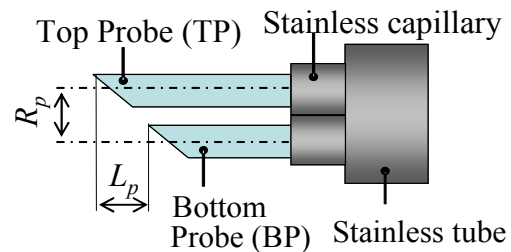
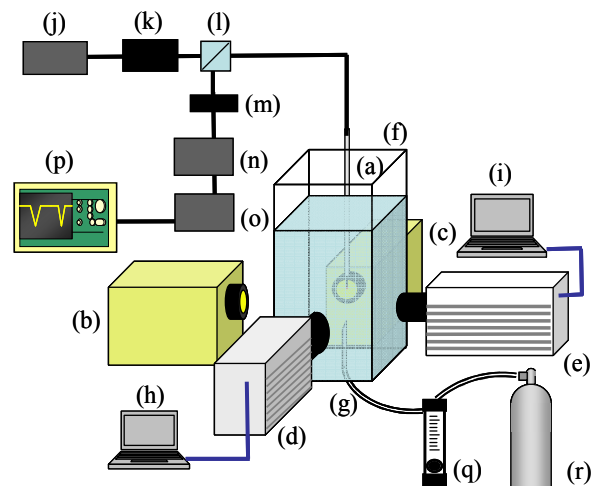


FIGURE 1. Structure of the T-TOP.



(a) T-TOP, (b) Halogen light source 1, (c) Halogen light source 2, (d) High-speed video camera 1, (e) High-speed video camera 2, (f) Acrylic water vessel, (g) Needle, (h) PC 1, (i) PC 2, (j) LD, (k) Objective lens, (l) Beam splitter, (m) Polarizer, (n) Photo multiplier, (o) Amplifier, (p) Recorder, (q) Flow meter, (r) Air tank.

FIGURE 2. Experimental setup.

4. Signal process of the T-TOP

A typical output signal of the T-TOP is illustrated in Fig. 3. When the optical fiber is covered with gas, the propagated beams are reflected and return at the tip, because of the difference for the refractive indices between the fiber and gas; hence, the signal of the TP (BP) increases at t_1 (t_2). On the other hand, when the optical fiber is covered with water, the propagated beams pass through into the water, because the refractive indices of the fiber is nearly equal to that of water; hence, the signal of the TP (BP) decreases at t_3 (t_4). By using the ON/OFF signal, the bubble velocity ($=U_b$) is calculated from the difference between t_2 and t_1 ($\Delta t_1 = t_2 - t_1$), and L_p . Then, the bubble velocity is defined as following equation.

$$U_b = L_p / \Delta t_1 \quad (1)$$

The bubble chord length ($=L_b$) is obtained from the U_b and the residence time of the TP ($\Delta t_2 = t_3 - t_1$). The bubble chord length is calculated,

$$L_b = U_b \cdot \Delta t_2 \quad (2)$$

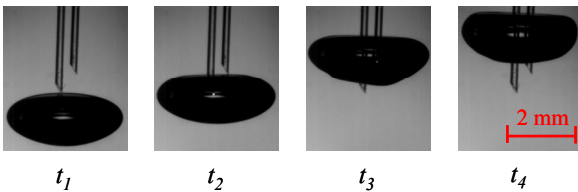
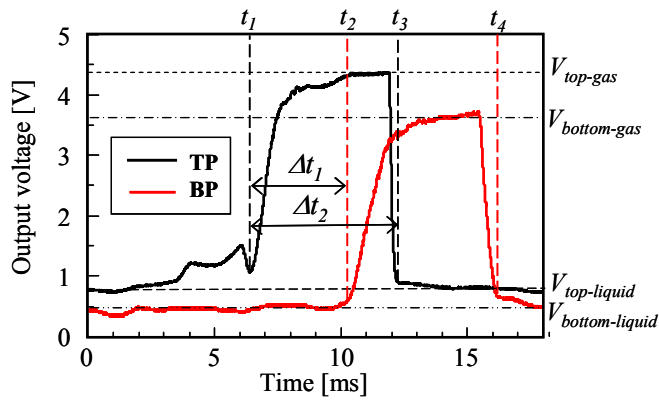


FIGURE .3 Typical signal of the T-TOP.

5. Result and discussion

In this research, four types of the T-TOP were employed for the bubble measurement to quantify the relationship between the T-TOP structure and the measurement accuracy. Note that R_p is constant, 0.5mm. The results of the visualization and T-TOP are presented in Tab. 1 and Tab. 2.

The difference between visualization and T-TOP is larger when " $L_p = 0.18\text{mm}$ ", in comparison to the other conditions. It is due to the effect of the interface deformation of the bubble; just before the BP touches the upper surface, the surface deformation spread around the bubble. This deformation causes the error of the detecting t_2 . Consequently, the calculation of U_b and L_b is largely affected, when " $L_p = 0.18\text{mm}$ ".

The difference is the smallest of all conditions, when " $L_p = 1.03\text{mm}$ ", and the difference is 10% below. From the visualization result, in this case, the surface deformation recovers, when the BP touches the bubble; hence, the U_b is exactly calculated as the gravity-center velocity of the bubble.

If L_p is longer than 1.03mm, the bubble-interface oscillation becomes dominant; hence, the difference of the results between visualization and T-TOP increases when " $L_p = 1.40\text{mm}$ ".

Summarizing these results, we can determine the optimized T-TOP size, that is, " $L_p = 1.03\text{mm}$, $R_p = 0.5\text{mm}$ ". The difference for the results of visualization and T-TOP is 10% below, and this value is a bias error.

TABLE.1 Comparison of velocity from visualization and T-TOP.

L_p	Velocity [mm/s]		Difference [%]
	Visualization	T-TOP	
0.18	299.44	1478.1	397.74
0.67	296.96	243.67	-17.95
1.03	295.25	286.46	-2.98
1.40	277.28	237.68	-14.28

TABLE 2 Comparison of chord length from visualization and T-TOP.

L_p	Chord length [mm]		Difference [%]
	Visualization	T-TOP	
0.18	1.67	8.23	393.57
0.67	1.76	1.49	-15.22
1.03	1.72	1.59	-7.85
1.40	1.92	1.67	-12.85

6. Vision

We confirmed the accuracy and influence for bubble measurements by using four types of the T-TOP and the visualization. The bubble motions are significantly differ in each T-TOP. Especially when " $L_p = 1.03\text{mm}$, $R_p = 0.5\text{mm}$ ", the T-TOP minimizes the influence of touching the bubble, and measures the bubbles with a high degree of accuracy. As a result, we defined this condition as the optimum T-TOP size.

In future study, we focus on the signals from the T-TOP to improve the measurement accuracy.

7. Reference

- Saito, T. & Kazishima, T. 2002 *JSME-B*, Vol. 68, No. 674, pp. 2719-2716.
- Saito, T. & Matsuda, K. & Ozawa, Y. & Oishi, S. & Aoshima, S. 2009 *Measurement of tiny droplets using a newly developed optical fibre probe micro-fabricated by a femtosecond pulse laser*, Measure. Sci. and Tech. Vol. 20, No. 11, pp. 114002.
- Sato, Y. 2010 *Graduation thesis*, Graduate School of Engineering, Shizuoka University, Saito Sanada Laboratory.

Dynamical Mass Transfer Process of a CO₂ Bubble Measured by using LIF/HPTS Visualization and Photoelectric Probing

Masanobu Tsukamoto

Department of Mechanical Engineering
Shizuoka University
Hamamatsu, Shizuoka, Japan

Takayuki Saito

Graduate School of Science and Engineering,
Shizuoka University
Hamamatsu, Shizuoka, Japan

Keywords: CO₂ bubble, mass transfer, LIF, photoelectric optical fiber probe, PIV

Abstract: We directly visualized the dynamical mass transfer process from a zigzagging rising CO₂ bubble to its surrounding liquid by using LIF/HPTS. We measured the surrounding liquid motion induced by bubble buoyancy using PIV. Further, the CO₂ concentration profile inside the bubble wake was measured directly by using a newly developed photoelectric optical fiber probe. Making the best and mutually complementary use of these three measurement techniques, we discuss the relationship between the mass transfer process and the flow structure. We succeeded in clearly visualizing CO₂-rich regions corresponding with the dynamical mass-transfer process from the bubble to the wake and the surrounding liquid. We also obtained a CO₂ concentration profile in the bubble wake. It was found that the CO₂-rich regions were formed into horseshoe-like vortices. In addition, we discuss the performance and characteristics of the newly developed photoelectric optical fiber probe.

1. Introduction

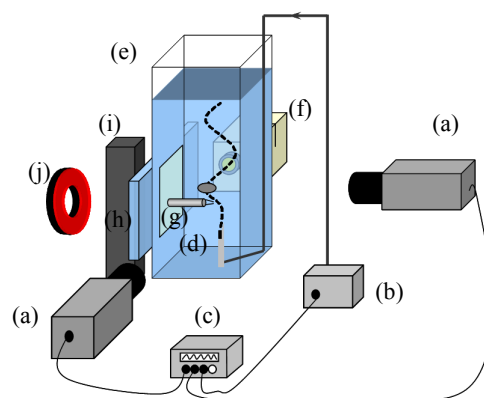
Gas-liquid two-phase flows are widely used in various industrial plants: chemical reactors, bioreactors, heat exchangers, and so on. The high efficiency of the gas absorption and the operation safety has been requested for the purpose of saving the energy and improving the economical performance. Hence, understanding of the relation between the mass transfer mechanism and the structure of the bubbly flow is essential.

In this paper, the first objective is to discuss the dynamical processes of the mass transfer from a zigzagging rising CO₂ bubble of 2.9 mm in equivalent diameter by using three measurement methods (i.e., LIF/HPTS, PIV and a newly developed photoelectric optical fiber probe). The second objective is to consider the characteristics of the new method (photoelectric optical fiber probe: POFP) to measure the point-wise concentration in the bubble wake as well as the bubble diameter and velocity, and to demonstrate its performance.

2. Experiment

2.1 Experimental setup for photoelectric optical fiber probe

The POFP was inserted into the side wall of the water vessel to measure the CO₂ concentration in the bubble wake. Fig. 1 shows a schematic diagram of an experimental setup employed in POFP measurement. An acrylic water vessel (100 mm × 100 mm × 400 mm) was filled with ion-exchanged and degassed tap water (29°C) to a depth of 380 mm. A specific bubble launch device composed of an acrylic chamber, an audio speaker, a precise pressure controller and check valves was used for launching single bubbles under the complete control of diameter, initial orientation, initial shape and launching interval (Sanada et al., 2006). The single bubbles were launched from a hypodermic needle (inner diameter: 0.40) fixed to the acrylic water vessel at the desired time interval. The red LED light and halogen light sources were used as back lights to clearly extract the bubble



(a) High-speed video camera, (b) Bubble generator, (c) Function generator, (d) Needle, (e) Water vessel, (f) Halogen light source, (g) Photoelectric fiber probe, (h) Acrylic plate, (i) 3-axis unit, (j) Continuous red LED

FIGURE 1. Experimental setup of the photoelectric fiber probe measurement.

2.2 Structure of the photoelectric optical fiber probe

A photoelectric optical fiber probe (POFP) was newly developed. The clearance L_P between the probes is 500 μm . The POFP has two functions of the concentration measurement by an electric sensor and the bubble measurement by an optical sensor. The optical sensor of the POFP utilizes the differences in refractive indexes of gas/liquid phases and optical fiber. On the other hand, the measurement of the concentration utilizes the difference of electric conductivity depending on the amount of CO₂ dissolution. To obtain the CO₂ concentration from the output voltage, we preliminarily obtained the calibration curves.

3. RESULTS AND DISCUSSIONS

3.1 Formation of the horseshoe-like vortices

Just after the launch of the bubble from the needle, clear horseshoe-like vortices (in a strict sense, a part of the horseshoe-like vortices) were observed. We visualized vortices simultaneously included both the wake structure and the mass transfer from the bubble to liquid phase across the bubble interface. The high-CO₂-concentration thin layer around the bubble was continuously flushed away and accumulated into the horse-shoe-like vortices. The vortices (i.e., bundles of CO₂-rich solution) were intermittently shed from the bubble in association with both the zigzagging motion and the surface oscillation; in succession the wreckage of the wake (i.e., small bodies of CO₂-rich solution) was transported widely into the surrounding liquid by the buoyancy driven flows. The surface oscillation plays a key role in turbulence characteristics (in a strict sense, velocity fluctuation) of the surrounding liquid

3.2 Flow structure of the CO₂-rich regions

The panels in Fig. 2 show a typical time evolution of the advective liquid-phase flows detected by PIV, and their corresponding dynamical mass transfer process induced by the flows. The measurement cross-sectional areas are indicated in Figure 2. Figure 3 shows the original snapshots of the cross-sectional bubble wake at each measurement time (0 msec: just after the bubble passing; 32 msec later; and 64 msec later). Fig. 4 presents the vorticity contour map obtained from PIV, and Figure 5 the velocity contour map.

In Fig. 2 - (a), a pair of cross-sectional bubble wakes, which are the same size and axisymmetric, is observed. In Fig. 3 - (b), the pair moves upward. Below the pair, a pair of cross-sectional bubble wakes, which are the same size and axisymmetric, is observed. Similarly, a pair of cross-sectional bubble wakes is observed further below. The interval between the pair wakes increases with time. The bubble wakes are diffused. Just before the vortex shedding, it is clearly observed that the pair wakes rotate in the opposite direction (Fig. 3 - (c)).

As shown in Fig. 4 - (a), positive/negative vorticity regions are formed between the pair wakes. The upward flows occur between the pair wakes as shown in Fig. 5 - (a). The CO₂-rich regions (the wreckage of the wake) are transported and spread upward by this strong upward flow (Fig. 5 - (b) & (c)). The velocities of the liquid phase gradually decrease, and the CO₂-rich regions spread slowly. These results indicate that the wreckage of the horseshoe-like vortices is transported over a wide range by this strong upward flow.

TABLE 1. Properties of the bubbles

Equivalent diameter [mm]	2.9
Terminal velocity [m/s]	0.28
Reynolds number [-]	849
Weber number [-]	3.4
Schmidt number [-]	529
Sherwood number [-]	687
Morton number [-]	2.6×10^{-11}

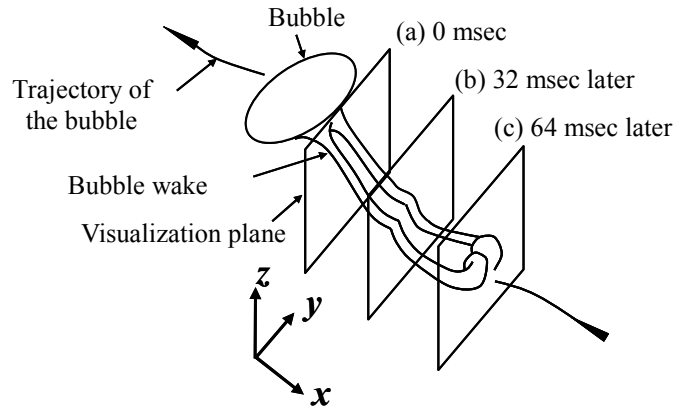


FIGURE 2. Visualization planes of the cross-sectional bubble wake.

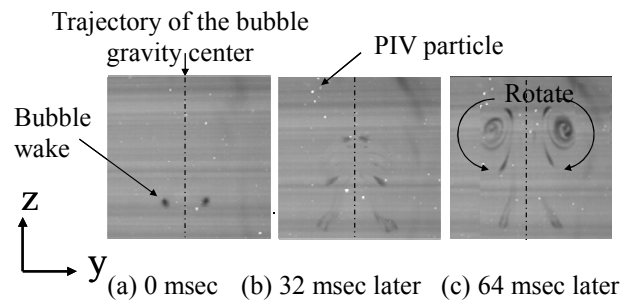


FIGURE 3. Snapshots of the cross-sectional bubble wake at each measurement time

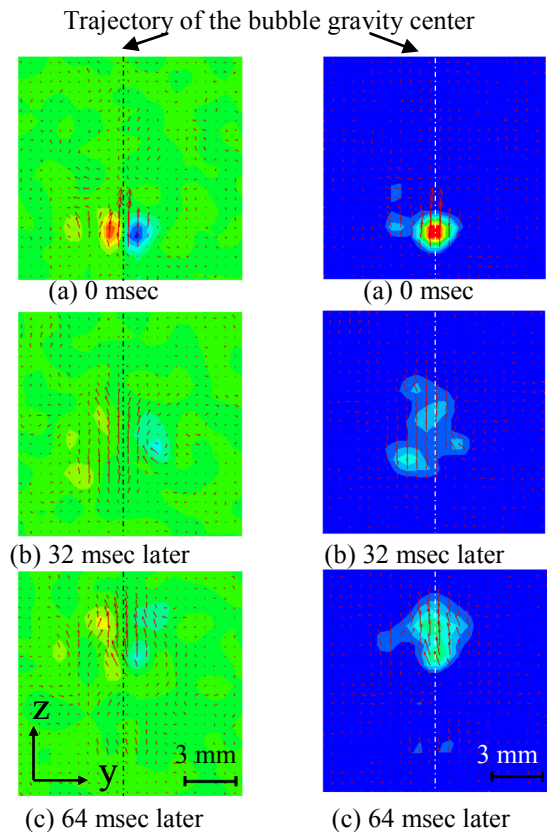


FIGURE 4
The vorticity contour map.

FIGURE 5.
The velocity contour map.

3.3 Results of measurements

3.3.1 CO₂ concentration measurement of the bubble wake via POFP. The lower probe of POFP pierces the bubble, and then it is completely covered with the bubble (gas phase). At this time, the output voltages of both the OFP and electric probe (EP) take the maximum. Next, since the space between two sensors of the EP is filled with the CO₂ solution of the thin concentration layer, the output voltage of the EP decreases.

Fig. 6 shows the profile of the CO₂ concentration measured in the wake near the bubble rear via the POFP. We succeeded in clarifying the profile of the CO₂ concentration inside the bubble wake, which is difficult to obtain from only the LIF/HPTS method. From this result, the CO₂ concentration takes the maximum at the center region of the bubble wake and sharply decreases toward the outer edge of the bubble wake.

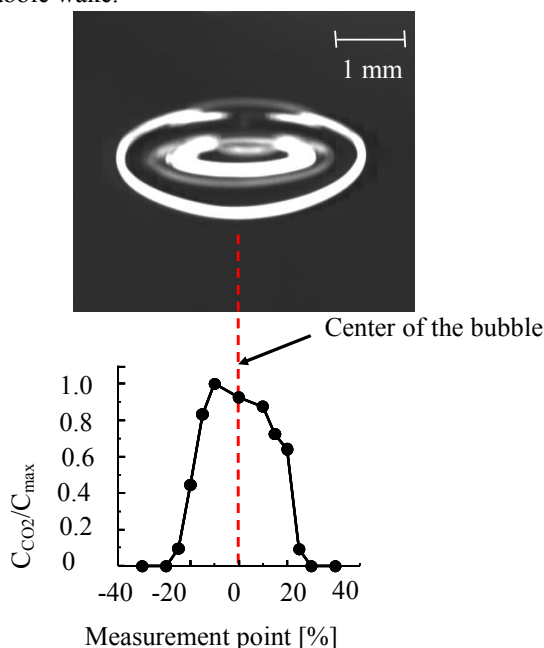


FIGURE 6. Normalized CO₂ concentration of the bubble wake.

3.3.2 Measurement of the bubble diameter and velocity.

The measurement results of the bubble velocity and length via the POFP calculated from data which the POFP contacts the center of the bubble were compared with those of the visualization. Tab. 1 shows the comparison of those measurement results. The difference in the average chord length between the two methods was less than 15%. The results obtained from the POFP were larger than those from the visualization; this was due to the bubble-POFP contact. Hence, the pierced chord length was measured as being longer than the original chord length.

TABLE 2. Difference between the photoelectric fiber probe and visualization result.

	Visualization	Photoelectric fiber probe	Difference [%]
Bubble diameter [mm]	1.65	1.85	12.0
Bubble velocity [mm/s]	248.8	206.8	-16.9

4. CONCLUSIONS

In this research, the dynamical mass transfer process of single bubble and surrounding liquid motion induced by bubble buoyancy were visualized via PIV and LIF/HPTS. In addition, we newly developed a photoelectric optical fiber probe to measure the CO₂ concentration inside the bubble wake directly.

We demonstrated that the mutually-complementary use of three measurement methods (i.e., LIF/HPTS, PIV and a newly developed photoelectric optical fiber probe) is very effective to experimentally examine the dynamical processes of the mass transfer from a zigzag rising CO₂ bubble.

5. REFERENCES

- Saito, T., Sakakibara, K., Miyamoto, Y., Yamada, M. 2010 A study of Surfactant Effects on the Liquid-Phase Motion Around a Zigzag-Ascent Bubble Using A Recursive Cross-Correlation PIV. *Chemical Engineering Journal*, Vol. 158, pp 39-50.
- Sanada, T., Watanabe T. & Fukuno T. 2006 Interaction and Coalescence of Bubbles in-Stagnant-Liquid. *Multi Science Technology*, Vol. 2, pp 155-174.
- Boden, S., M. Bieberla & U. Hampel. 2008 Quantitative Measurement of Gas-Hold-up Distribution in a Stirred Chemical Reactor Using X-Ray Cone-Beam Computed Tomography. *Chemical Engineering Journal*, Vol. 139, pp 351-362.
- Bruker, C. 1999 Structure and Dynamics of the Wake of Bubbles and its Relevance for Bubbles Interaction. *Physics Fluids*, Vol. 11, pp 781 – 1796.
- Clift, R., J. R. Grace & M. E. Weber. 1978 *Bubbles, Drops and Particles*. Academic Press, New York.
- De Vrise, A. W. G., A. Biesheuvel & L. Van Wijngaarden. 2002 Notes on the Path and Wake of a Gas Bubble Rising in Pure Water. *International Journal of Multiphase Flow*, Vol. 28, pp 1823 – 1835.
- Madhavi, T., A. K. Golder, A. N. Samanta & S. Ray. 1996 Studies of Bubble Dynamics With Mass Transfer. *Chemical Engineering Journal*, Vol. 128, pp 95 – 104.
- Motarjemi, M. & G. J. 1978 Mass Transfer From Very Small Bubbles – The Optimum Bubble Size for Aeration. Jamesone, *Chemical Engineering Science*, Vol. 33. pp 1415 – 1423.
- Vlasogiannis, P., G. Karagiannis, P. Argyropoulos & V. 2002 Air-Water Two-Phase Flow and Heat Transfer in a Plate Heat Exchanger. Bontzoglou, *International Journal of Multiphase Flow*, Vol. 28, pp 757 – 772.

Particle motion in a kHz-order-ultrasound-irradiated water (The relation between the particle motion and an acoustic cavitation bubble)

Yuta Nakamura
Faculty of Mechanical Engineering,
Shizuoka University,
Hamamatsu, Shizuoka, Japan

Takayuki Saito
Graduate School of Science and technology,
Shizuoka University,
Hamamatsu, Shizuoka, Japan

Keywords: Cavitation bubble, Particle aggregation, kHz-order ultrasound

Abstract: We investigated a new solid-liquid separation technique using kHz-order ultrasound. This method is able to aggregate particles dispersed in a water by contactless operation. Few studies were reported about the particle-aggregating technique by ultrasound of kHz-order frequency. Moreover the mechanism of the particle aggregation in such a condition is still unclear. In the present study, in order to clarify the mechanism of the particle aggregation in a water irradiated by kHz-order ultrasound, we investigated the relation between the particle motion and the acoustic cavitation bubble motion. We have found out that the acoustic cavitation bubble adhering to the particle contributes significantly to aggregation of the particles. Based on the time-resolved visualization of the bubble motion on the particle and the 3D structure of bubble clouds obtained from sonoluminescence distribution, we discuss the particle aggregation quantitatively.

1. Introduction

The ultrasound techniques are encountered in a lot of industrial apparatuses such as ultrasonic cleaning, particle manipulation and ultrasonic atomization. These techniques have an useful characteristic that non-contact operation is available. The ultrasound techniques are also available for solid-liquid separation. This separation method has almost no environmental load, because this method does not need maintenance, and does not need chemicals such as aggregating agent. We focused attention on solid-liquid separation by using ultrasound of kHz order.

In the past studies, MHz-order ultrasound has been mostly employed in the ultrasound separation techniques. It was reported that the acoustic radiation force dominantly acts on aggregation of particles. This force is caused by pressure gradient generated in liquid phase by the sonic waves. However, the studies on kHz-order ultrasound had almost not been reported before. Therefore, the mechanism of particles aggregation is not clear yet.

We conducted the present study in order to reveal the mechanism of particle aggregation under irradiation of kHz-order ultrasonic in water. We quantitatively discuss the particle motion and the acoustic cavitation bubble motion based on time-resolved visualization. Furthermore we evaluated the acoustic force quantitatively.

2. Experimental setup

The experimental setup consisted of an ultrasound driving system and a camera system. In the former system, a sine wave voltage signal (frequency: 20.3 kHz, output voltage: 1.00 V) was supplied into a BLT transducer through a power amplifier. The ultrasound was irradiated vertically from the bottom of an acrylic water vessel (diameter: 50 mm, height: 110 mm). A standing wave field was formed by the incident waves from the BLT transducer and the reflected waves from the surface of the water. The vessel was filled with two types of 150 ml ultrapure water: ultrapure water degassed and

including air. In the camera system, the conditions of Case 1 and Case 2 are described below in detail.

2.1 Case 1 : Position of the particle aggregation

First, we investigated the particle motion with respect to particle diameters. The examined particles were 300, 400, 600, 1000 μm in diameter. The density of each particle was 1.05 g/cm^3 . The images were captured by CCD camera. In order to capture the whole vessel, the spatial resolution was 1024×1024 pixel² (64.5 $\mu\text{m}/\text{pixel}$), and the frame rate was 30 fps.

2.2 Case 2 : Particle motion and acoustic cavitation bubble motion

Second, we investigated the interaction between the 300- μm -diameter particle and the acoustic cavitation bubble. The images were captured by high speed camera. The spatial resolution was 512×512 pixel² (3.85 $\mu\text{m}/\text{pixel}$), and the frame rate was 20,000 fps. The interrogation area was positioned just under the pressure antinode (height from the bottom of the vessel: approximately 20 mm) in the standing wave.

3. Results

Fig. 1 shows the relation between the particle concentration and the position of the aggregated particles against the particle diameter. The particle aggregations stayed near the pressure node or antinode in the standing wave field, depending on the particle diameter. The acoustic cavitation bubble also gathered near the pressure node and the antinode. Therefore, the particle motion qualitatively conforms to that of the acoustic cavitation bubble. Furthermore, when there was no acoustic cavitation bubbles in the water (degassed ultrapure water), particles did not aggregate. Therefore, the acoustic cavitation bubble significantly contributes to the aggregation of particles.

Fig. 2 shows time-series images of a particle and an acoustic cavitation bubble adhering to the particle surface, and

the definitions of θ_v and θ_b . We successfully captured an acoustic cavitation bubble adhering to the particle, that expanded and contracted in synchronization with the sound pressure. It is confirmed that a particle moved toward upper left of the image and the acoustic cavitation bubble was adhering at the traveling direction of the particle. We defined that θ_v was the angle formed between x axis and particle velocity vector, θ_b was the angle formed between x axis and the adhered bubble position, as shown Fig. 2. Then, θ_d was angular difference between θ_v and θ_b .

Fig. 3 shows the relation between the particle velocity V and θ_d . The particle velocity was constant until 1.5 ms when θ_d was relatively-large. However, the particle velocity increased since 1.5 ms when θ_d was approximately 0. Therefore, we considered that particles were towed by the adhered acoustic cavitation bubbles, then the acoustic cavitation bubble lies between aggregated particles.

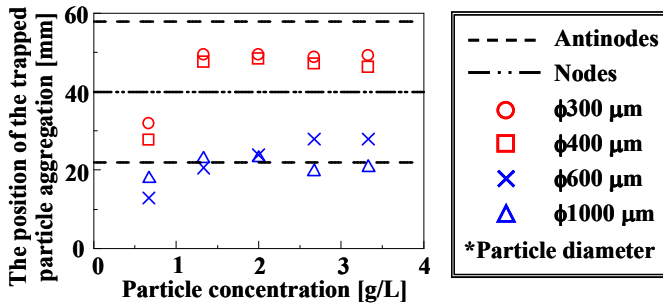


FIGURE. 1 The position of the trapped particle aggregation.

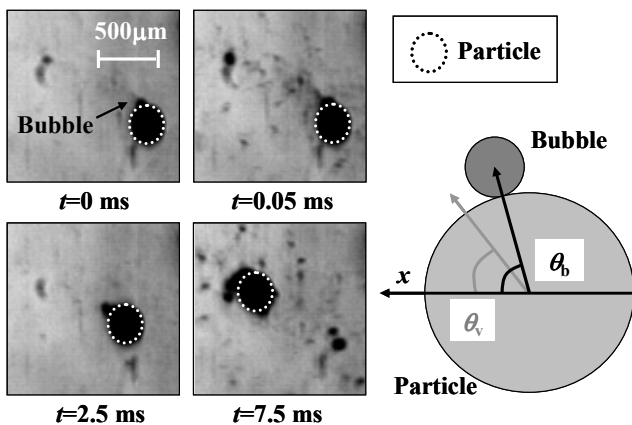


FIGURE. 2 Images of a particle and acoustic cavitation bubbles.

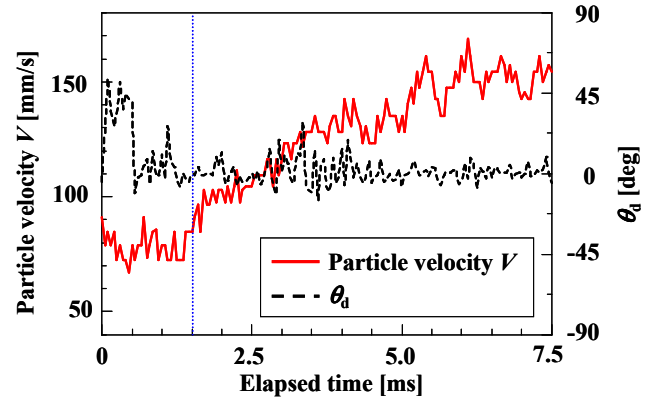


FIGURE. 3 The relation between the particle velocity V and θ_d depending on the elapsed time.

4. Conclusions

In the present study, we have revealed the mechanism of the particle aggregation in water under irradiation of kHz-order ultrasound. The positions of the aggregated particles were discussed by comparing the position that the acoustic cavitation bubble gathered. Furthermore, we evaluated the relation between the particle motion and the acoustic cavitation bubble motion quantitatively. The acoustic cavitation bubble significantly contributes to aggregation of particles. In detail, the acoustic cavitation bubble adhered to the particle surface, then the particle was towed by the acoustic cavitation bubble. In the future study, we will clarify the mechanism that the acoustic cavitation bubble adheres to the particle surface.

5. Nomenclature

t	Elapsed time, ms
V	Particle velocity, mm/s
θ	Angle, deg

Subscripts

b	bubble
v	velocity vector
d	difference

6. References

- Yamakoshi, K. 1996, "Erythrocytes concentrated non-destructively by acoustic radiation force" *Technical report of IEICE*, US96-71
- Steven, M. W. 1997, "Measurement of Ultrasonic force for particle-liquid separation" *AIChE Journal*, Vol. 43, No. 7
- Mitome, H. 2001, "Micro bubble and sonoluminescence" *Jpn. J. Appl. Phys.*, Vol. 40, 3484-3487.

3D Simulations of a Bubble/Droplet Measurement via a Single-Tip Optical fiber Probe

Hajime Furuichi
 Faculty of Mechanical Engineering,
 Hamamatsu, Shizuoka, Japan

Takayuki Saito
 Graduate school of Science and Technology,
 Hamamatsu, Shizuoka, Japan

Keywords: Ray tracing method, Optical fiber probe, bubble/droplet measurement

Abstract: An optical fiber probe (OFP) method is one of very available techniques for gas-liquid two-phase flows, to measure a velocity and size of a bubble/droplet. To improve its measurement accuracy, the output signals from the OFP must be considered deeply. However, previous studies on the OFP seem to lack quantitative analysis of the signals. For the practical purpose to extract meaningful signals, we have developed the numerical simulation code via 3D-ray-tracing method. In this study, firstly, we verified appropriateness and accuracy of the developed code, comparing with some experiments. Second, output signals from the bubble measurement were observed and it was described that some noises occurred. We also clarified the mechanism of the signals from the numerically reconstruction. Furthermore, to extract signal potentials, we focused on that the output value depends on contact conditions between a bubble and the OFP. Finally the measurement accuracy was successfully advanced.

1. Introduction

An optical fiber probe method (Hanyu & Saito, 2010, Sakamoto & Saito 2011) is one of the common techniques employed to the gas-liquid two-phase flows. Recently, one of authors uniquely developed a Single-Tip Optical fiber Probe (S-TOP) (Saito, T. et al, 2009). By using the S-TOP measurement, the ascending velocity and the chord length of a bubble successfully measured only with a wedge-shaped tip of a single probe. However to bring out its hidden potential we have to deeply consider the optical signals from the probe and precisely analyze them. Many past studies on the probing showed successful results, however they seem to lack quantitative analysis of the optical signals. The optical fiber probing utilizes optical interaction between the laser beams emitted from the optical fiber and the bubble/droplet. Although the probing system (an LD, a photo detector and a digital recorder) and measurement principle (detection of change of refraction indexes) are simple, the optical signals are very difficult to analyze due to the complicated interaction between the laser beams and gas-liquid interface. For the practical purpose of extracting the meaningful signals, we have developed the numerical simulation code of 3D-ray-tracing and conducted precise experiments to consider the interaction.

2. Algorithms

A ray tracing method (Koshihara, M. et al., 1992) is appropriate for our purposes. The light waves are assumed to be ray segments and the diffraction is ignorable in this method. These assumptions enable us to determine ray trajectories. Thus, the reflection and refraction of the incident laser beams are numerically calculated in accordance with the Snell's law. Our new code takes each beam 3D trajectory, each beam energy and each beam polarization into account. The reflectivity R and the transmissivity T are defined as follows:

$$R = \frac{\tan^2(\theta_i - \theta_t)}{\tan^2(\theta_i + \theta_t)} \quad T = \frac{\sin 2\theta_i \sin 2\theta_t}{\sin^2(\theta_i + \theta_t) \cos^2(\theta_i - \theta_t)} \quad (1)$$

P Polarization

$$R = \frac{\sin^2(\theta_i - \theta_t)}{\sin^2(\theta_i + \theta_t)} \quad (2)$$

S Polarization

$$T = \frac{\sin 2\theta_i \sin 2\theta_t}{\sin^2(\theta_i + \theta_t)}$$

where θ_i and θ_t are the incidence and refraction angles of rays transmitting a surface, based on the Snell's law. According to the described algorithms, we model the S-TOP measurement (including the S-TOP, lights, and a bubble) in the spatial coordinate, as demonstrated in Fig. 1.

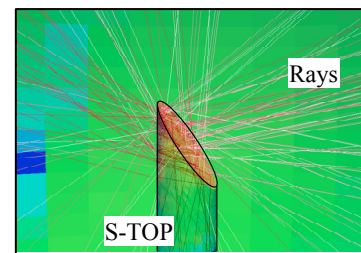


FIGURE 1. A demonstration of the ray-trace simulation.

3. Experiments for the validation

3.1 S-TOP

Fig. 2 shows that a micrograph of the S-TOP employed in this study. The tip is 200 μ m of diameter, and is polishing-processed to 35 degrees of a wedge angle.

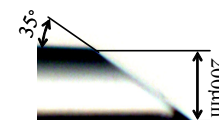


FIGURE 2. A micrograph of the S-TOP.

In practical measurement, the S-TOP has some advantages: simple system and high adaptation for a small bubble/droplet.

In particular, the single tip optical fiber probe with a wedge-shaped tip enables us to simultaneously measure diameters, velocities and number density of bubbles/droplets. The problem is that a position pierced by the S-TOP is not detected. We have found out how to detect the position by using “pre-signal”. The pre-signal was considered to be noise in the past investigations; however it includes very important information. We consider the mechanism of the pre-signal, and the method to detect the pierced position via the pre-signal, numerically and experimentally.

3.2 Results of the validation

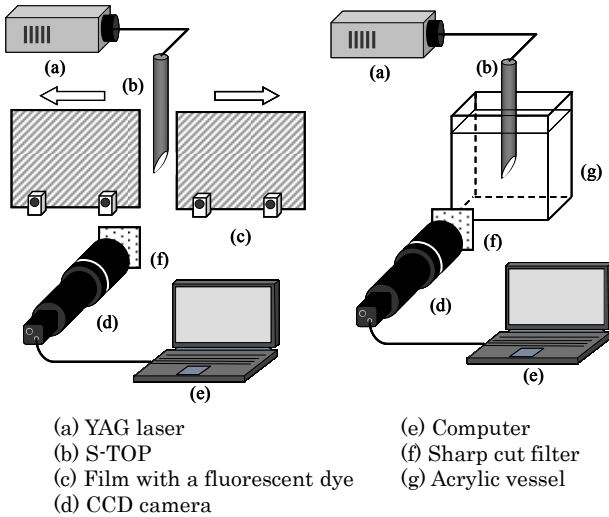


FIGURE 3. Experimental setup.

We verified appropriateness and accuracy of our numerical simulation code by comparison with experimental results. Fig. 3. shows that the experimental setup. The laser beams (wavelength: 570nm) emitted from the probe tip into water were visualized by using a fluorescent dye (Rhodamine B: excitation wavelength of 535nm). The beams emitted from the tip into air were also visualized by using a thin film uniformly interpenetrated by the same dye. Thus, we employed a sharp-cut filter that only passes above 550nm, and YAG-laser as the light source, so then images of the emitted lights were filmed by CCD camera. On the other hands, the developed code constructed the S-TOP and rays transmitting as already shown in the Fig. 1. They were converted to a 3D spatial map of the ray energy, to specifically compare with the experiments.

Fig. 4 shows a comparison between the numerically simulated results of the emitted laser beams from the S-TOP tip and the experiment ones. The beam distributions in the water phase and the gas phase obtained numerically agree well with the experimental ones. The energy density distributions from the numerical simulation also agree with the experimental ones. Therefore, the appropriateness and accuracy of our code are demonstrated.

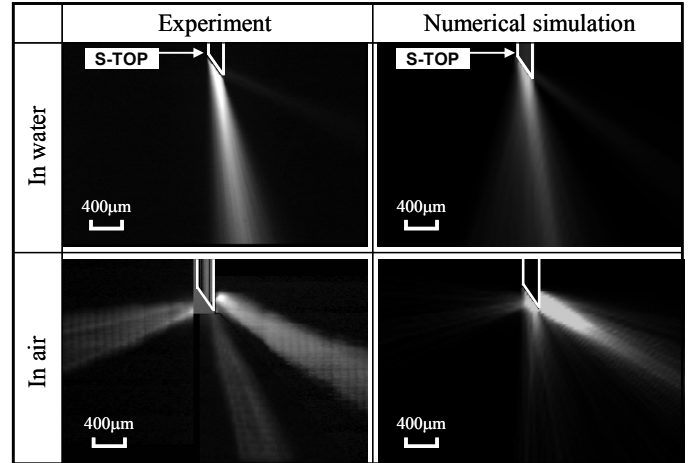


FIGURE 4. A comparison of discharged lights.

4. Output signals in a bubble measurement

4.1 Measurement principle of the S-TOP

A typical output signal of the S-TOP is plotted in Fig. 5. When the wedge-shaped tip of the S-TOP is completely positioned in the water phase (Fig. 5.(1)), the output intensity is low. Just before the tip touches the bubble frontal surface, a sharp peak signal (pre-signal) is observed. The wedge-shaped tip is gradually covered with the gas phase, and the output signal gradually increases. When the tip is completely positioned in the bubble (Fig. 5.(2)), the output signal takes almost a constant value. When the tip goes through the bubble rear surface, the output signal rapidly decreases. An intensive and clear pre-signal occurs only when the tip penetrates a bubble frontal surface at the center region. Using this characteristic of the pre-signal, we are able to detect the position pierced by the S-TOP. In other words, we are able to extract burst signals that the S-TOP pierced bubbles at their center region. As illustrated in Fig. 6., when the S-TOP penetrates a bubble at the center region, correct measurement of the diameter and velocity are achieved.

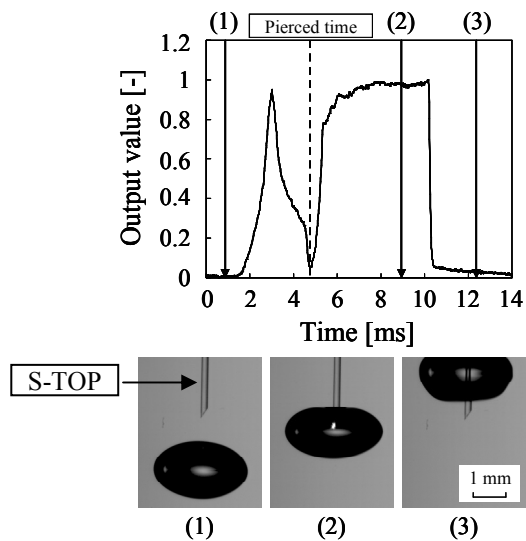


FIGURE 5. An output signal of the bubble measurement.

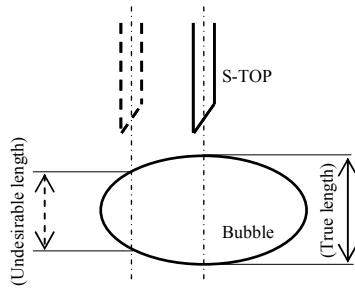


FIGURE 6. Chord length measurement by the S-TOP.

4.2 The numerically analysis

Fig. 7. shows a numerical result. The laser beams emitted from the S-TOP are reflected at the bubble frontal surface, and some of them re-enter into the S-TOP. According to the result, the signal was separated into the three signal patterns. They enable us to discuss the mechanism of the pre-signal in the empirical S-TOP signal. Moreover, such the peak (pre-signal) appears in the specific case as shown in the Fig. 6. Based on this meaningful information, we established a new method to decay the random error in the S-TOP measurement (Pre-signal threshold method (Mizushima & Saito, 2011)), and successfully improved its accuracy.

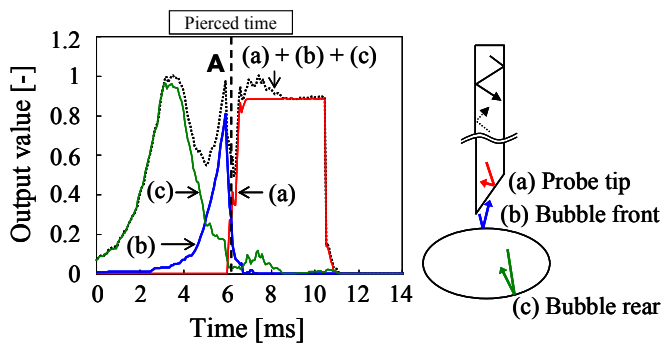


FIGURE 7. An analysis of the signal patterns.

5. Summary

In order to develop a new method to detect a position pierced by the S-TOP, we conducted the numerical simulation of 3D-ray-tracing and considered the mechanism of the pre-signal. As a result from a new signal analysis via the simulation, pre-signal occurred. The intensity of the pre-signal depends on positional relation between the tip and bubble surface. Using the numerical simulation of 3D-ray-tracing, we understood the mechanism of the pre-signal and established Pre-signal threshold method. Further, we improved the accuracy of the S-TOP measurement.

6. References

- Hanyu, K. & Saito, T., 2010 Dynamical Mass Transfer Process of a CO₂ Bubble Measured by using LIF/HPTS Visualization and Photoelectric Probing. *Can. J. Chem. Eng.*, Vol. 88, 551-560.
- Sakamoto, A. & Saito, T., 2011, Robust algorithms for quantifying noisy signals of optical fiber probes employed in industrial-scale practical bubbly flows *International Journal of Multiphase Flow*, Under Review.
- Saito, T. et al, 2009 Measurement of tiny-droplets using a newly developed optical fiber probe microfabricated by femtosecond pulse laser. *Meas. Sci. Technol.*, Vol. 20, 114002.
- Koshiba, M. et al., 1992 Simple scalar finite element approach to optical rib waveguides. *IEE Proc. J.*, Vol. 139, 166-171.
- Mizushima, Y. & Saito, T., 2011 Detection method of piercing positions for the bubble measurement by a Single-Tip Optical fibre Probe. *Meas. Sci. Technol.*, Under Review.

Measurement of ozone bubbles using optical fiber probe in wastewater treatment system

Daisuke Shinohara

Department of Mechanical Engineering,
 Shizuoka University
 3-5-1 Johoku, Nakaku, Hamamatsu,
 Shizuoka, Japan

Takayuki Saito

Graduate School of Science and Technology
 Shizuoka University
 3-5-1 Johoku, Nakaku, Hamamatsu,
 Shizuoka, Japan

Keywords: S-TOP, Ozone bubble, Wastewater treatment

Abstract: Wastewater from a dairy farm, which contains milk fatty acids and proteins, is very difficult to treat by commonplace wastewater processing. Recently, these contaminations and the visual pollution is a major concern for the dairy farmers. In order to overcome these problems, we study the wastewater treatment system with ozone. This system is easy to introduce for small and medium-scale dairy farmer because the structure of the ozone treatment system is compact and simple. However, we have not interpreted the flow regime in the system enough. The purpose of this study is to clarify the flow dynamics of ozone bubbles in the system with a Single-Tip Optical fiber Probe (S-TOP). Using this measurement, we can measure the ozone bubble velocity and the pierced chord length. Based on these feature of ozone bubbles, the flow structure in the wastewater treatment system was discussed. Finally, we clarified what contributes to the effectiveness of the system.

1. Introduction

Wastewater from a dairy farm, which contains milk fatty acids and proteins, is very difficult to treat by commonplace wastewater processing. Recently, these contaminations and the visual pollution is a major concern for the dairy farmers. Wastewater treatment with ozone is the way which resolves organic substances with injecting ozone bubbles into the wastewater. The system is easy to introduce for small and medium-scale dairy farmer because the structure of the ozone treatment system is compact and simple. Saito laboratory and Shizuoka Prefectural Research Institute of Animal Industry research the ozone treatment of the wastewater containing milk to demonstrate and improve the efficiency of the system.

The purpose in this study is to clarify the flow dynamics of ozone bubbles in the system with a Single-Tip Optical Fiber Probe (S-TOP).

2. Measurement method of S-TOP and experimental setup

2.1 The bubble measurement of the S-TOP

Typical output signal of the S-TOP is depicted in Fig. 1. When the S-TOP positions in the water phase, the output voltage is low. On the other hand, when the S-TOP detects bubbles, the output voltage increases. Due to the wedge shape of the S-TOP, The gradient of the steep surge in the signal is proportional to the bubble interface velocity; hence, The bubble velocity U_B is easily obtained from the following equation :

$$U_B = \alpha \times g_{rd} \quad (1)$$

where g_{rd} is the gradient of the steep surge in the output signal and α is a proportional coefficient.

The pierced chord length, L_B is obtained from the following equation:

$$L_B = U_B \times (t_e - t_s) \quad (2)$$

where t_s is start time of touching the bubble and t_e is the time departing from the bubble.

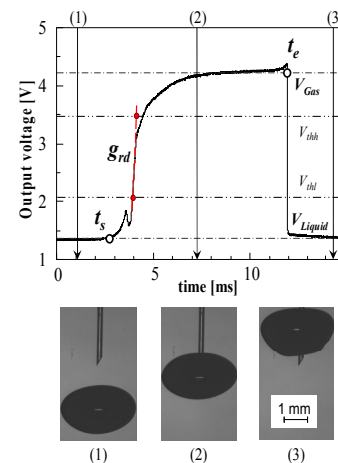


FIGURE 1. Typical output signal of S-TOP

2.2 The experimental setup

Fig. 2 shows an outline of the experimental equipment. A tank (a) (900mm in height and 565mm in diameter) is filled with the water included fatty milk about 160L. The ozone is generated from an ozone generator (e) and injected into the tank through a pipe (f) (267mm in diameter). In order to measure the ozone bubbles, the S-TOP (b) is fixed nearby the pipe exit. The S-TOP signals are obtained with the optical system (c) and the digital oscilloscope (d). The measurement is conducted at 9 points ($H = 209, 329, 449\text{mm}$ and $r = 49, 71, 94\text{mm}$, in Fig. 3). Each measurement time is 3 min. The flow rate of ozone bubble is constantly kept in 9.5 L/min during the measurement.

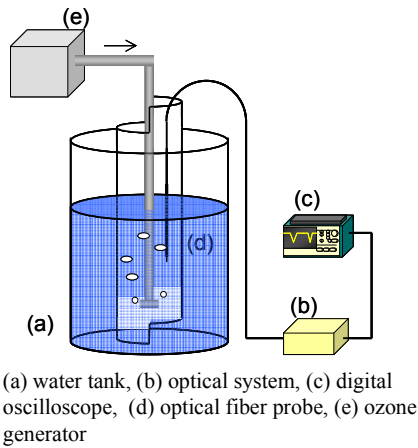


FIGURE 2. Experimental setup

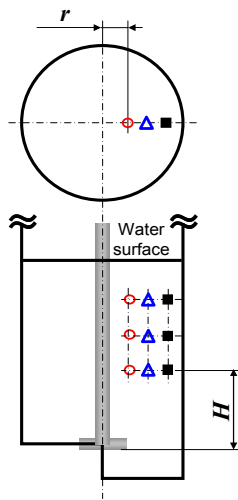


FIGURE 3. Experimental condition

3. Results and discussion

Fig. 3 describes the relationship between the measurement point and the bubble velocity. In Fig. 3, the bubble velocity increases from 209 to 329mm in height (lower region) especially at 49mm in radius. However, all the velocity decreases from 329 to 449mm in height (upper region).

Fig. 4 describes the relationship between the measurement point and the chord length of the bubble. In Fig. 4, the chord length decreases at the lower region, however, it increases at upper region.

We consider these results as follows: depending on the height, the dominant phenomena are different. Namely, at the lower region, the chemical reaction (i.e. ozone dissolving in wastewater) is dominant; hence, the bubble size is small. By contract, at the upper region, the dynamics of fluid is dominant; hence, the coalescence enlarges the bubble sizes, and the descent flow decelerates the bubble ascending. Consequently, the measurement results are different in each height.

4. Conclusion

In this study, we clarify the flow dynamics of ozone bubbles in the wastewater treatment system with the S-TOP.

Consequently, the measurement results are different in each height. We consider that it is caused by the difference of the dominant phenomena in respective heights. The fresh ozone bubbles react to the wastewater at the lower region in the system, however, the descent flow and mixing occur near the water surface.

In future study, we deeply examine the effective flow pattern for the ozonization. We will focus on the initial condition of the ozone bubble, “a measurement at the outlet of the ejector”. Then we will improve the reaction between ozone and wastewater from a flow dynamic and chemical point of view.

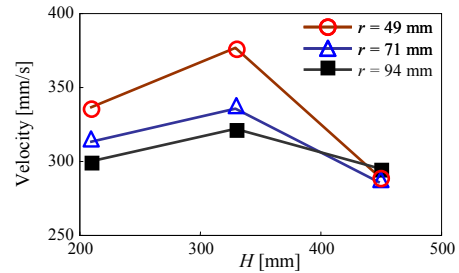


FIGURE 4. Result of bubble velocity

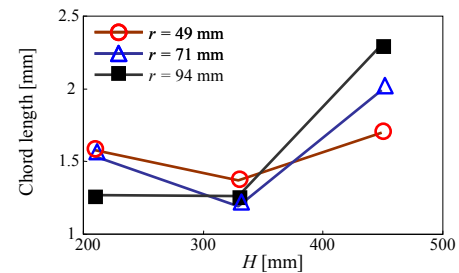


FIGURE 5. Result of bubble chord length

5. References

- Sato, K. & Saito, T. 2011 Capture/separation of fatty acids and proteins from wastewater containing milk by ozone treatment. *The 9th International Conference on Separation Science and Technology*
- Mizushima, Y & Saito, T. 2011 A newly developed technique for detection of a contact position in bubble measurements by a single-tip optical fiber probe. *ASME- JSME- KSME Joint Fluids Engineering Conference 2011*

Elucidation of a large-scale structure of a bubbly flow in a bubble column by using a Four-Tip Optical Fiber Probe

Yuki Masumoto

Department of Mechanical Engineering,
 Shizuoka University
 Hamamatsu, Shizuoka, Japan

Takayuki Saito

Graduate School of Science and Technology,
 Shizuoka University
 Hamamatsu, Shizuoka, Japan

Keywords: Bubbly flow structure, Optical fiber probe, Void fraction

Abstract: The large-scale flow structure in a bubble column has a strong relation to the mass transfer mechanism. Hence, elucidating of the flow structure is important in order to improve the efficiency of the gas absorption. In the present study, the large-diameter bubble column of 380 mm in inner diameter and 1500 mm in height was employed. We measured bubble diameters, velocities and void fraction, by a Four-Tip Optical Fiber Probe (F-TOP). We obtained the histogram of bubble diameters and velocities and the fluctuation of the void fraction. The large-scale fluctuation of the void fractions faded out toward the upper zone of the bubble column. From these results, a flow structure in a bubble column was divided into three zones which are the bottom, middle and upper zone.

1. Introduction

Bubble column reactors are widely used in various industries such as chemical industry because of their simple structure and high-mass-transfer performance. However, it is essential to clarify the details of the flow structure in a bubble column in order to improve the efficiency of chemical reactions and gas absorption.

In the present study, we measure a bubble diameter, velocity and time-series void fractions by using a Four-Tip Optical fiber Probe (F-TOP). From these results, we discuss a large-scale structure of a bubbly flow in the bubble column.

2. Experimental setup and measurement method

2.1 Experimental setup

Fig. 1 shows a schematic diagram of experimental setup. We used an acrylic bubble column of 380 mm in inner diameter and 1500 mm in height and covered with an acrylic water jacket (1605 mm × 440 mm × 440 mm) to reduce a distortion due to the refractive indices. A perforated plate (diameter of pores: 1.0 mm; equilateral triangular pitch: 10 mm; the number of pores: 1240) was installed at the bottom of the bubble column. Tap water (temperature 290.5 – 296 K) is supplied into the bubble column through a water inlet. In addition, compressed air (temperature 295 – 296 K) adjusted to 67 NL/min by using a mass flow controller was pumped into the bubble column.

2.2 Four-Tip Optical fiber Probe (F-TOP)

We used the F-TOP measurement system to measure bubble characteristics. An optical fiber probe is the phase detecting method which utilizes differences in the refractive indices of gas/liquid phase and optical fiber. The system of an optical fiber is shown in Fig. 2. Some of the laser beam from a laser diode reaches the tip of the optical fiber probe. When the tip of the optical fiber is positioned in a gas phase, the laser beam is reflected at the tip surface and returns into the same fiber. The output signal obtained from a photomultiplier is

recorded at a PC via an A/D converter. From the output signal, we calculate bubble diameters/velocities and time-series void fractions in a bubble column.

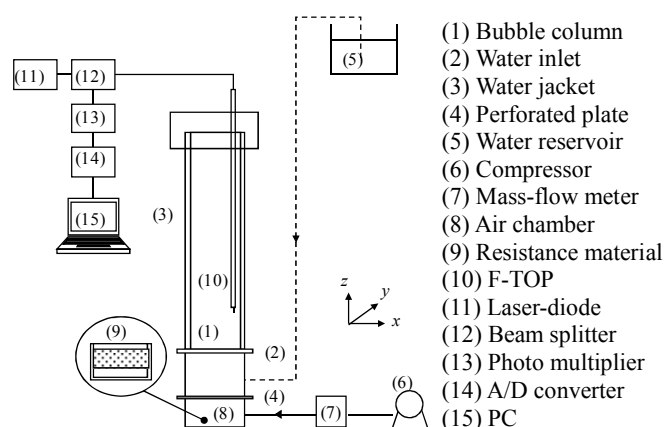


FIGURE 1. Experimental setup of bubble column.

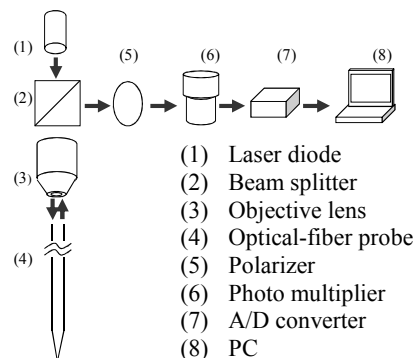


FIGURE 2. F-TOP measurement system.

3. Results and discussion

3.1 Bubble diameter and velocity

Fig. 3 shows histograms of bubble diameters and velocities in a bubble column. The distribution patterns of the bubble diameter at $z = 100$ mm and $z = 700$ mm are almost the same, and the distribution range is 2.0 ~ 9.0 mm. On the other hand, in the case of $z = 1300$ mm, the distribution range changes into 2.0 ~ 7.0 mm. However, the peak-value of bubble diameters shows approximately 4 mm regardless of z which is height from the bottom of the bubble column. The bubble velocities shift to a lower value along with an increase in height from the bottom.

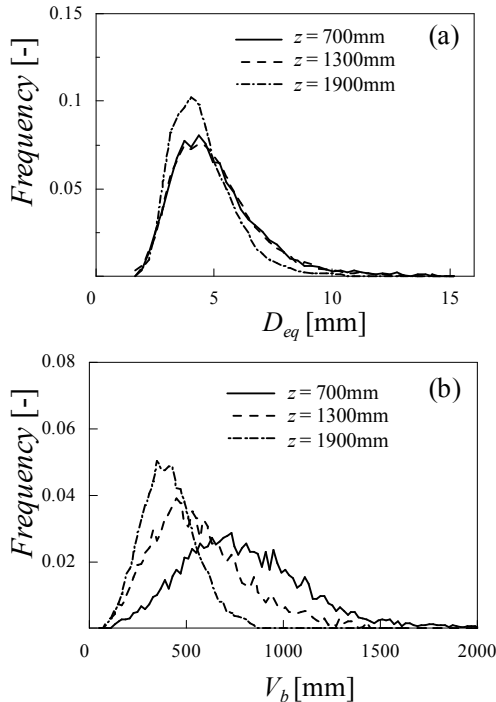


FIGURE 3. Statistical distributions of bubble parameter; (a) Histograms of bubble diameter; (b) Histograms of bubble velocity.

3.2 Time-series void fractions

The time-series void fractions are calculated at four points {P1: $(x, y) = (-95$ mm, -95 mm), P2: $(x, y) = (-95$ mm, 95 mm), P3: $(x, y) = (95$ mm, -95 mm), P4: $(x, y) = (95$ mm, 95 mm)}, and the results at $z = 100$ mm, 700 mm, 1300 mm are shown in Fig. 4. The origin of a coordinate system was placed at the center of a perforated plate. The void fractions at $z = 100$ mm are located eccentrically in space, and the magnitude of fluctuation is large. Furthermore, the region of high void fractions moves to a circumferential direction with time. Although the fluctuation of the void fraction decreases at $z = 700$ mm, there is the spatial variation of the void fraction. However, the spatial variation of void fraction at $z = 1300$ mm almost disappears and magnitude of fluctuation becomes small. Therefore, the large-scale fluctuation of the void fractions fades out toward the upper zone of the bubble column.

From these results, the flow structure in a bubble column is divided into three zones. In the bottom zone ($z = 100$ mm), the void fractions were unevenly distributed in the spatial

region of the cross-section surface. This spatially non-uniform distribution of the void fractions disappeared toward the upper zone ($z = 1300$ mm). The middle zone ($z = 700$ mm) is the transition zone of the flow structures.

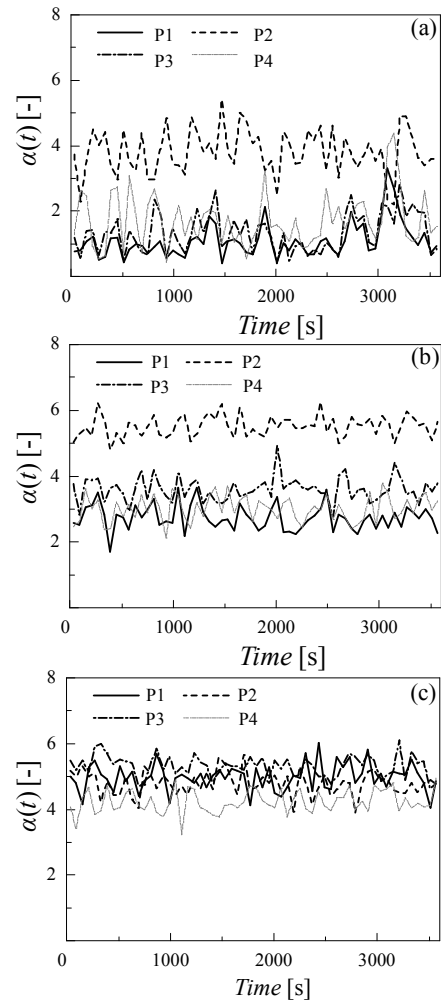


FIGURE 4. Time-series void fraction obtained by four-point simultaneously measurement: (a) $z = 100$ mm, (b) $z = 700$ mm (c) $z = 1300$ mm.

4. Conclusion

In the present study, we discussed a large-scale structure of a bubbly flow in a bubble column. We obtained histograms of bubble diameters/velocities and the fluctuations of the void fraction by the F-TOP measurement method. In conclusion, we demonstrated that the large-scale structure of a bubbly flow in a bubble column is divided into three zones from the distribution of the void fractions. We obtained the helpful results to elucidate a large-scale structure of a bubbly flow. Moreover, we need to elucidate the details of a flow structure due to the measurement of liquid-phase motion.

5. References

Higuchi, M. & Saito, T. 2010 Quantitative characterizations of long-period fluctuations in a large-diameter bubble column on point-wise void fraction measurements, *Chem. Eng. J.*, vol.160, pp.284-292.

7. Proceedings of Korean Students Presentation

Korean students presented three presentations in this program. The information of the presentation was listed as follow.

Presentation 1

Title: Design and Manufacture of High Efficiency Horizontal Wind Turbine Blades

Presenter: Jongmin Kim and Heesung Lee

Presentation 2

Title: Vertical axis type wind turbine Design and manufacturing

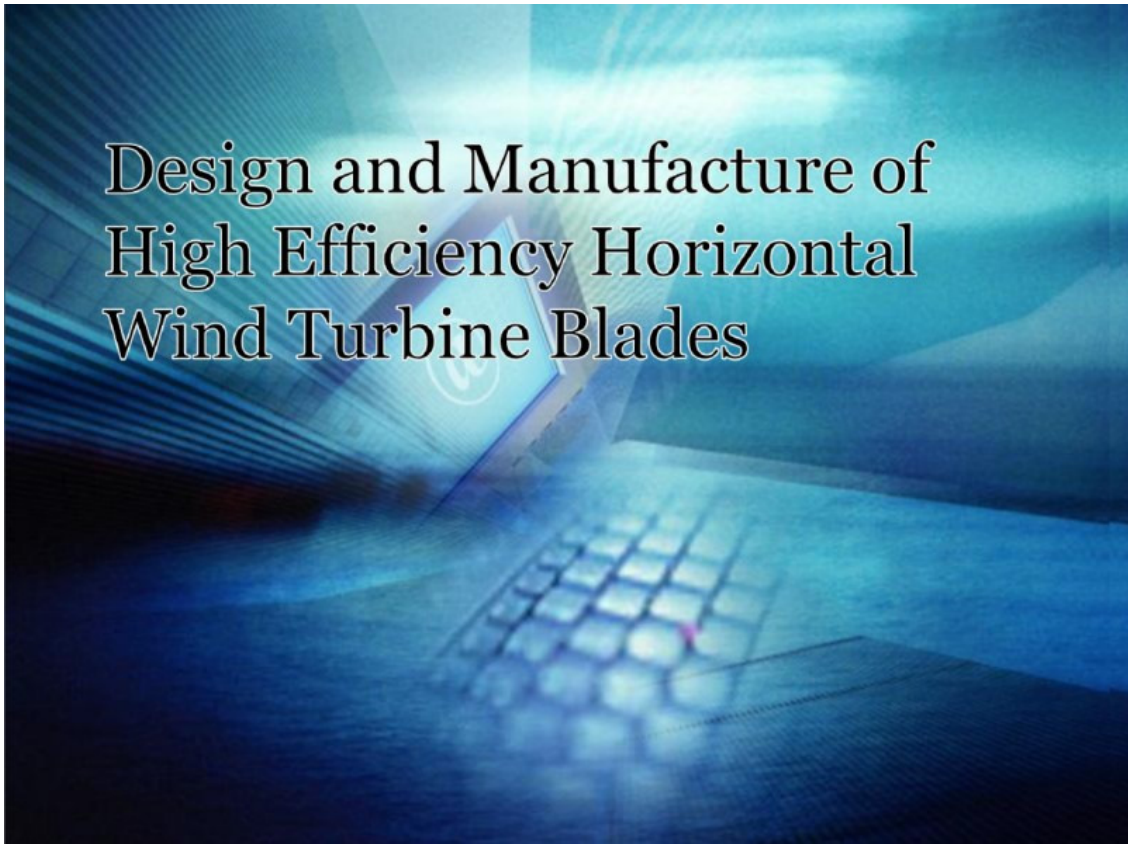
Presenter: Chunggi Moon and Kyeongrock Jang

Presentation 3

Title: Flow analysis using the Magnus effect of circular cylinder

Presenter: Jeonghoon Song

The briefing papers of the presentation are shown from next page.



contents

- I Backgrounds & Objectives
- II Theory
- III Design of blades
 - 1 Blade shape
 - 2 Design and Manufacture
- IV Experimental study
 - 1 Experiments
- V Numerical study
 - 1 CFD analysis
- VI Conclusion

Changwon National University Computational Fluid Engineering Lab.

I. Backgrounds & Objectives



Changwon National University

Computational Fluid Engineering Lab.

III. Theory

Basic Theory

$$P_T = T\omega \quad \text{Turbine shaft power}$$

$$P_w = \frac{1}{2} \rho U^3 A \quad \text{Fluid power}$$

$$C_p = \frac{P_T}{P_w} = \frac{T\omega}{\frac{1}{2} \rho U^3 A} \quad \text{Power coefficient}$$

T = Torque

ω = Angular Velocity

ρ = Air density

A = Area

U = Wind speed

R = Radius

Air density $\rho = 1.2\text{kg/m}^3$

Area $A = 0.0196\text{m}^2$



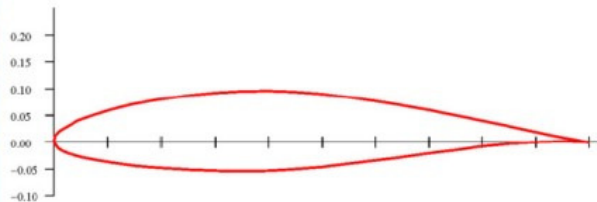
Changwon National University

Computational Fluid Engineering Lab.

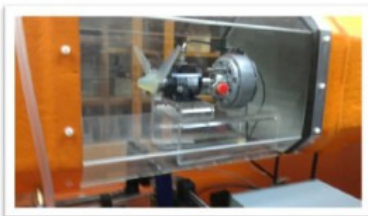
III. Design of blades (1/3)

Blade shape

1) NACA64-415



2) Size



- Area of wind tunnel : 35 x 35 cm
- Length of blade model : 0.15m
- Angle of attack : 10°



Changwon National University

Computational Fluid Engineering Lab.

III. Design of blades (2/3)

Material of blade

3) Material selection

Type	Advantage	Disadvantages
Carbon Fiber Reinforced Plastic (CFRP)	<ul style="list-style-type: none"> · Extremely lightweight, high strength · shape are free to express · There is no change due to weather or the environment. 	<ul style="list-style-type: none"> · The price is expensive · While processing be harmful to health
Timber	<ul style="list-style-type: none"> · Easy to obtain · Processing is very easy · Nature-friendly 	<ul style="list-style-type: none"> · Are heavily influenced by humidity · Strength is weak compared to other materials · Relatively heavy in weight

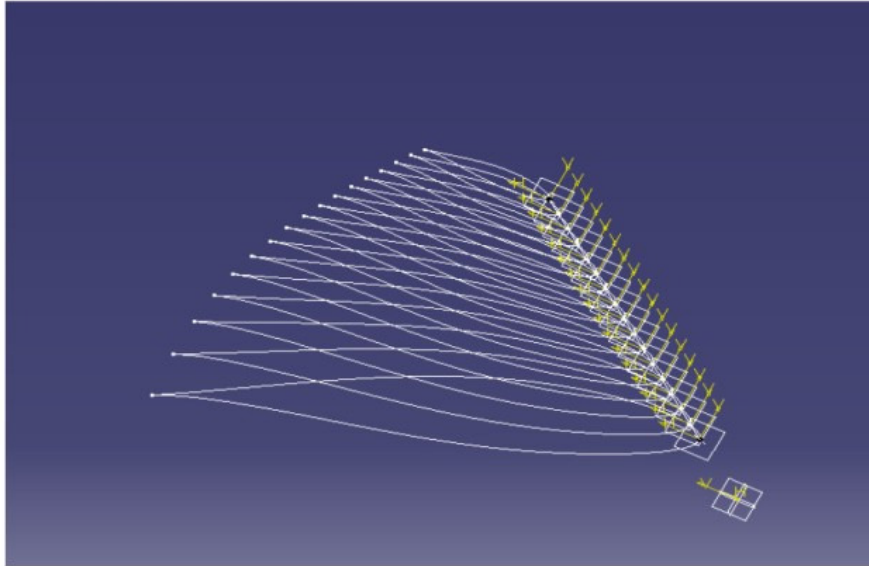


Changwon National University



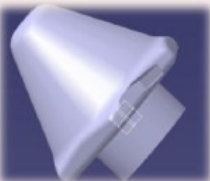


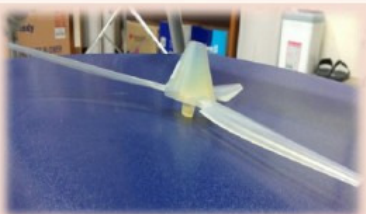
Computational Fluid Engineering Lab.

III. Design of blades (3/3)

◆ Blade Design (by CATIA)

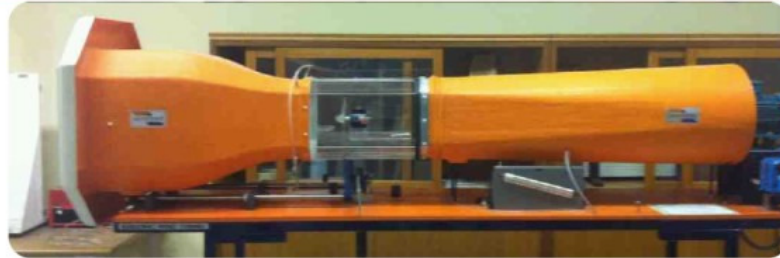


III. Manufacturing

Type	Designed	Manufactured
BLADE		
HUBE		
ASSEMBLY		

IV. Experimental study

1. Wind tunnel test – measuring device.



[wind tunnel]



[tachometer]



[Wind gauge]



[powder braker]



[torque meter]



Changwon National University

Computational Fluid Engineering Lab.

IV. Experimental study

Methods

- 1) Set the wind speed of 10m/s with no load condition. Then, measure rpm and give the input voltage at powder breaker by applying a load to measure torque.
- 2) Measure torque value and rpm by Using the inverter of wind tunnel, increasing wind speed of 0.5m/s, and repeating the above experiment about each wind speed.
- 3) Compare about shaft power P_T and power coefficient C_p by Experiments and calculating with velocities



Changwon National University

Computational Fluid Engineering Lab.

IV. Experiments

Experimental data according to wind velocity

Revolutions (rpm)					
Velocity	10 m/s	10.5 m/s	11 m/s	11.5m/s	12 m/s
rpm	340	498	615	870	1100

Experimental data according to the speed– torque

T (N·m)					
Velocity	10 m/s	10.5 m/s	11 m/s	11.5m/s	12 m/s
rpm	0.069	0.078	0.102	0.113	0.121

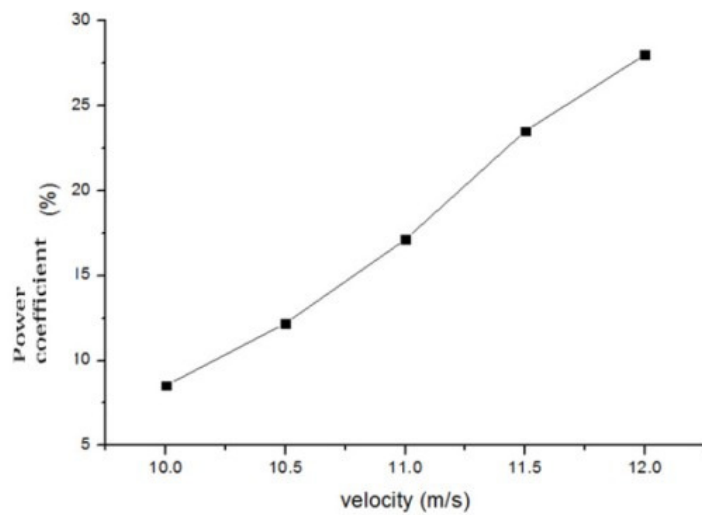
IV. Experimental Results

Turbine power according to Velocity

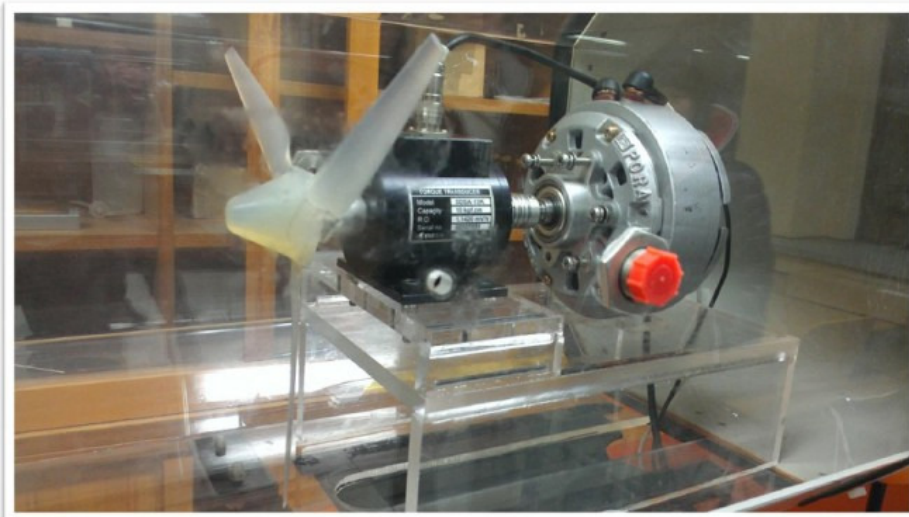
Turbine power					
Wind speed(m/s)	10	10.5	11	11.5	12
P_T	3.615	5.985	9.667	15.149	20.51
P_W	42.411	49.096	56.449	64.502	73.287
Power coefficient (%)	8.52	12.253	17.124	23.489	27.98

IV. Experimental Results

Power coefficient and velocity

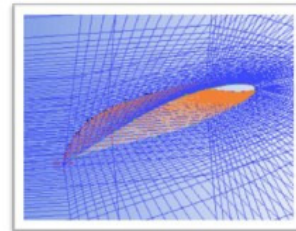
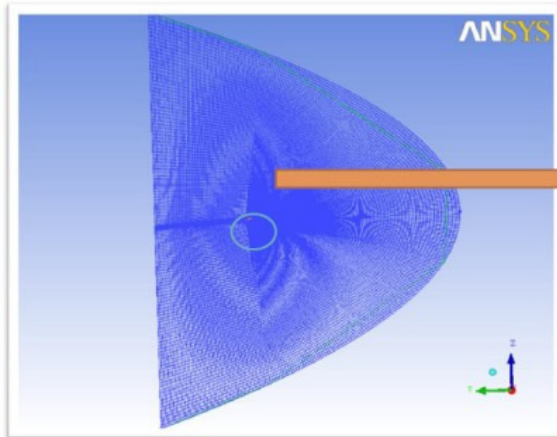


IV. Experiments



V. Numerical Study

Computational analysis by CFD



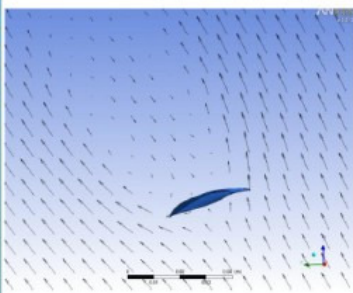
- ◆ Grid = about 945,000
- ◆ Turbine radius = 0,15m
- ◆ Boundary conditions = no slip condition

Inlet	Outlet
Velocity= 10 m/s	Pressure= 1atm

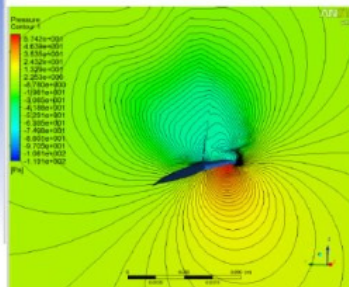
V. Numerical Study

Computational analysis by CFD

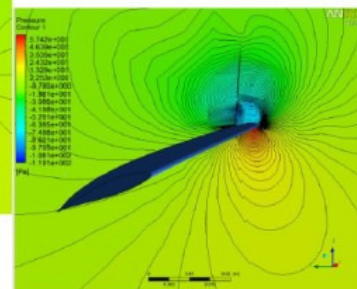
- ◆ Three-dimensional distribution of CFD



Vector distribution



Pressure Distribution



Pressure Distribution

VI. Conclusions

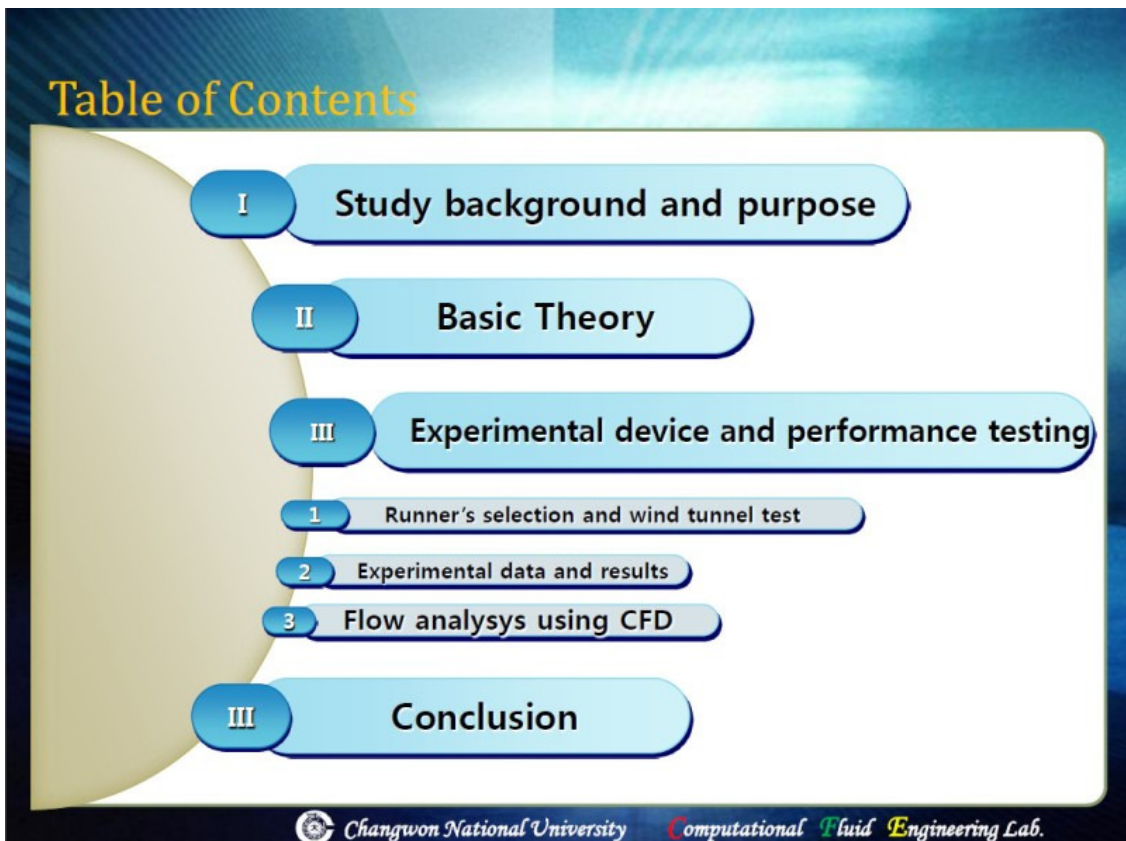
- ◆ As a challenges of engineering design for high efficiency blade, horizontal wind turbine was constructed.
- ◆ The shape of blade was chosen by NACA64-415 according to the investigation of recent researches and related references
- ◆ The materials of blade was also selected by CFRP composite material
- ◆ The size modeled of blade was determined by the law a similarity and it is designed by using CATIA 3-D modeling Tool
- ◆ Experimental test of designed horizontal wind turbine was carried out using wind tunnel and obtained power coefficient of 10~27% which is close to theoretical efficiency of 30%
- ◆ Numerical investigation was performed well simulated
- ◆ Variable device of angle of blade, different shape of blade and their more detailed actual test will be constantly studied to make high efficient wind turbine



Changwon National University

Computational Fluid Engineering Lab.

**Thank you so
much.**



Basic theory

Basic theory of wind turbines

Theory

$$P_T = T\omega \quad : \text{ turbine's power}$$

$$P_W = \frac{1}{2} \rho U^3 A \quad : \text{ wind power}$$

$$\lambda = \frac{V}{U} = \frac{R\omega}{U} \quad : \text{ velocity rate}$$

$$\text{power coefficient} = \frac{P_T}{P_W}$$

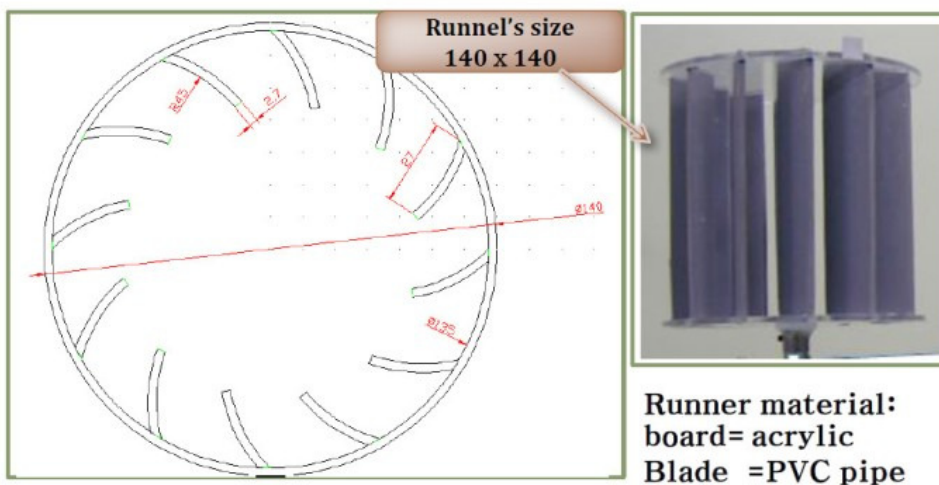
T = torque
 ω = angular velocity
 ρ = air's density
 A = projection area
 U = wind's velocity
 V = velocity
 R = turbine's radius

$$\rho = 1.2 \text{ kg/m}^3$$

$$A = 0.0196 \text{ m}^2$$

Experimental device and performance testing <Runnel's production>

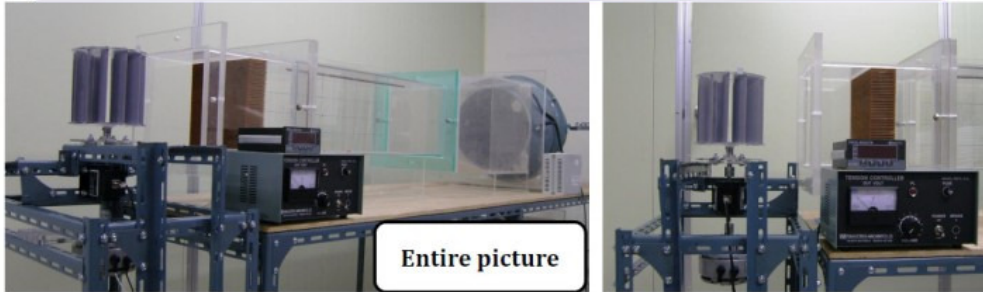
Runnel's design and manufacturing



Experimental device and performance testing

<Wind tunnel and measuring device>

Wind tunnel and measuring device



<tachometer>

<anemometer>

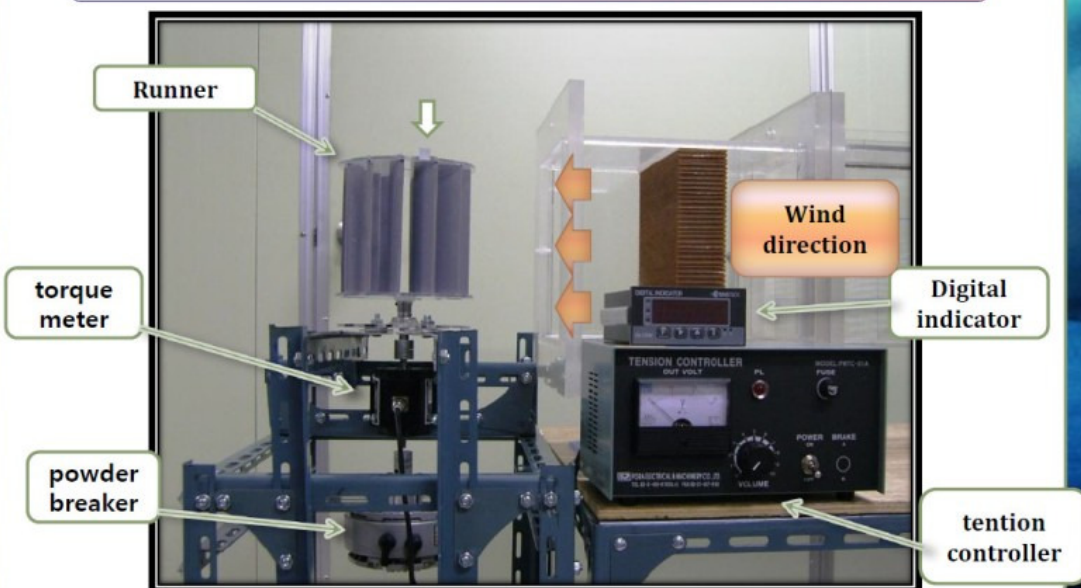
<powder breaker>

<torque meter>

Experimental device and performance testing

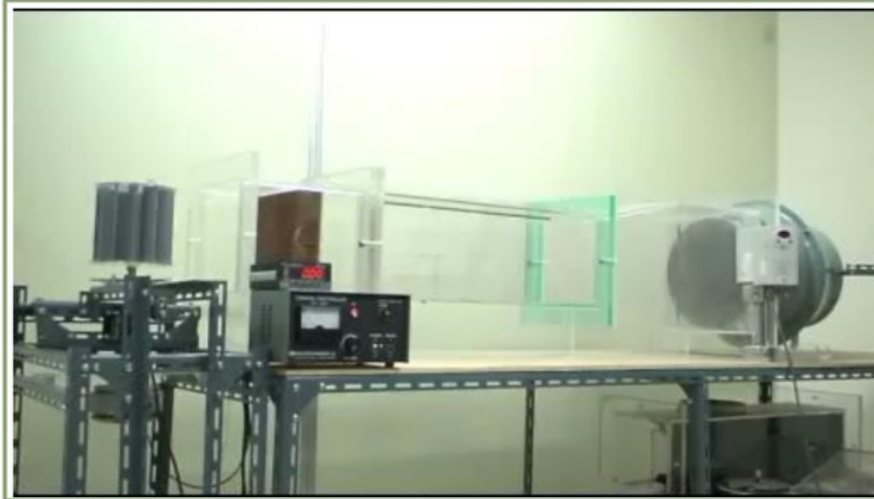
<Wind tunnel and measuring device>

Wind tunnel and measuring device



Experimental device and performance testing <testing>

Wind tunnel experimental video



Changwon National University

Computational Fluid Engineering Lab.

Experimental device and performance testing Experimental methods

Experimental methods

- 6.5m/s is set to wind velocity. Powder breaker will start no load condition. Powder breaker's input voltage control When wingtip velocity rate is 0. Applying a load to the wind turbine as a Measuring torque and angular velocity for wingtip velocity ratio.
- Wind speed of the air blower is adjusted by the inverter.(7.5m/s, 8.5m/s)repeat the above test methods For each wind speed.
- Using based on theory substitute each value. As a result, P_t (Turbine's power) and C_p (power coefficient) is obtained.



Changwon National University

Computational Fluid Engineering Lab.

Experimental device and performance testing <DATA>

Wind velocity according to the experimental data - rpm, Torque

6.5m/s								
ω [rad/s]	2.6	8.7	12.3	14.5	16.2	25.1	26.9	
T [N.m]	0.01176	0.01078	0.01078	0.0098	0.0098	0.00784	0.00686	

7.5m/s								
ω [rad/s]	2.1	18.2	24.8	26.7	27.7	29.2	39.1	
T [N.m]	0.01764	0.01666	0.01568	0.0147	0.0147	0.01372	0.00882	

8.5m/s									
ω [rad/s]	1.9	7.02	16.7	30.9	34.4	35.6	37.3	39.6	52.7
T [N.m]	0.02254	0.02156	0.02058	0.01862	0.01666	0.01506	0.0147	0.01372	0.00882

Experimental device and performance testing <DATA>

Rotation according to the turbine power($P_T = T\omega$)

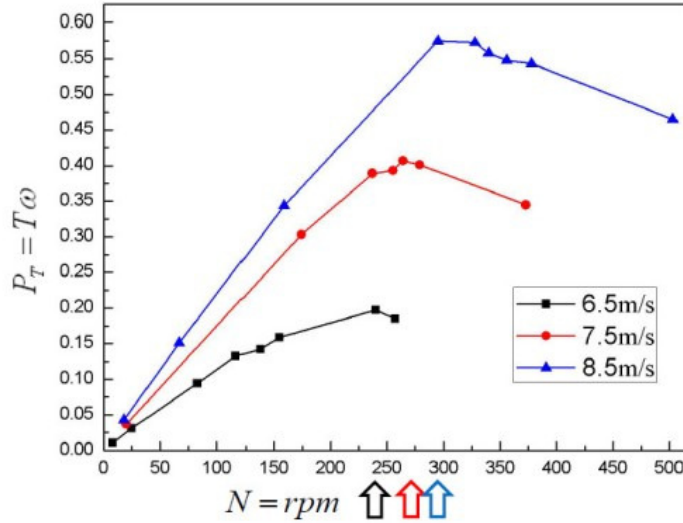
6.5m/s								
RPM (N)	8	25	83	117	138	155	240	257
$P_T = T\omega$	0.011	0.031	0.094	0.133	0.142	0.159	0.197	0.185

7.5m/s							
RPM (N)	20	174	237	255	264	279	373
$P_T = T\omega$	0.037	0.303	0.389	0.393	0.407	0.401	0.345

8.5m/s									
RPM (N)	18	67	159	295	328	340	356	378	503
$P_T = T\omega$	0.043	0.151	0.344	0.575	0.573	0.558	0.548	0.543	0.465

Experimental device and performance testing <Graph of result>

Turbine power and rpm ($P_T = T\omega$)



Experimental device and performance testing <DATA>

Wingtip velocity ratio (λ) and power coefficient

6.5m/s									
λ	0.028	0.094	0.132	0.156	0.174	0.270	0.29		
Power coefficient	0.010	0.029	0.041	0.044	0.049	0.061	0.057		
7.5m/s									
λ	0.02	0.17	0.23	0.25	0.26	0.27	0.37		
Power Coefficient	0.008	0.061	0.078	0.079	0.082	0.081	0.071		
8.5m/s									
λ	0.02	0.06	0.14	0.26	0.28	0.29	0.31	0.33	0.43
Power Coefficient	0.006	0.021	0.048	0.08	0.079	0.077	0.076	0.075	0.064

$$\lambda = \frac{r\omega}{U}$$

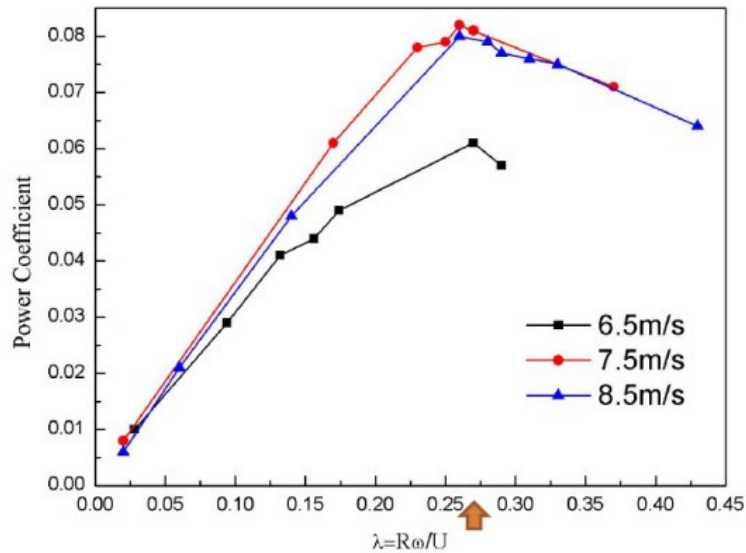
power coefficient t

$$= \frac{T\omega}{\frac{1}{2}\rho U^3 A}$$

$\rho = 1.2 \text{ kg/m}^3$
 $U = \text{wind velocity}$
 $A = 0.0196 \text{ m}^2$

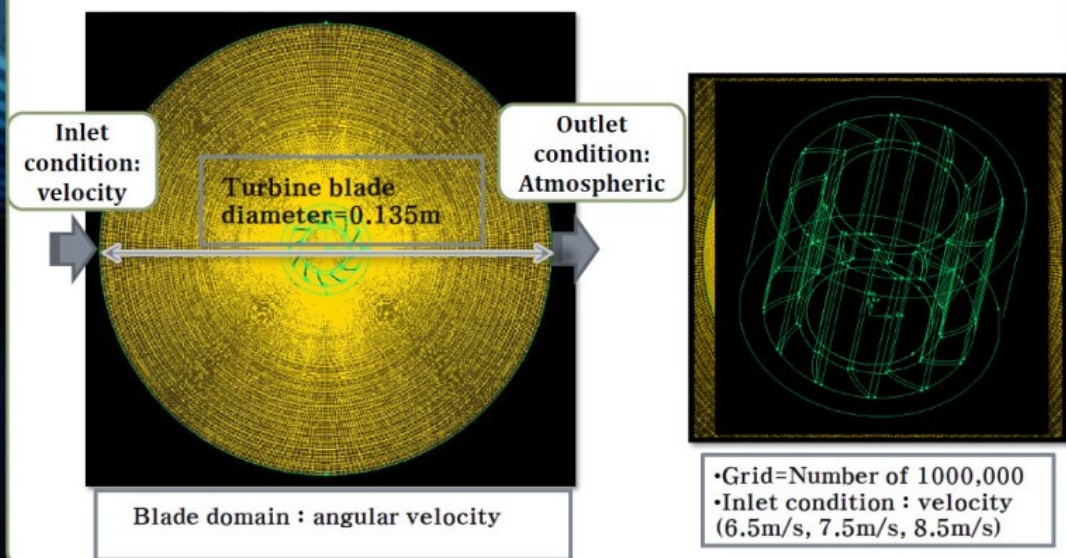
Experimental device and performance testing <Graph of result>

Power coefficient and wingtip velocity ratio



Experimental device and performance testing <Flow analysis using Fluent>

<Flow analysis using Fluent>

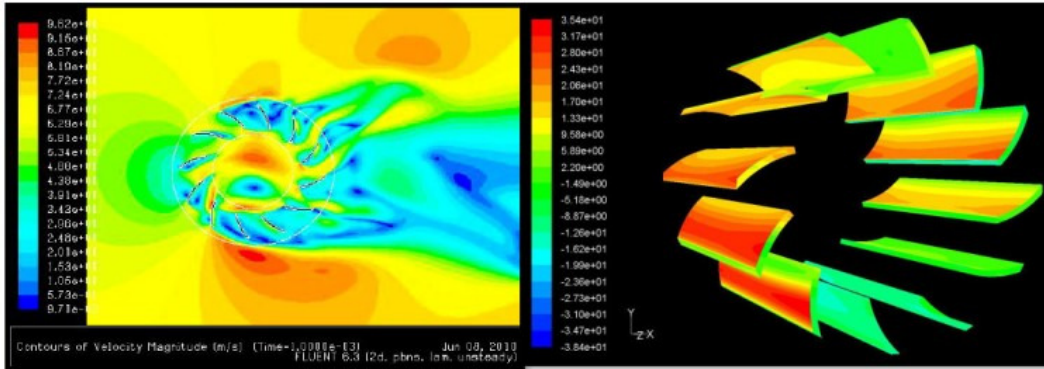


Experimental device and performance testing
 <Flow analysis using Fluent>

<Flow analysis using Fluent>

Velocity distribution

Pressure distribution



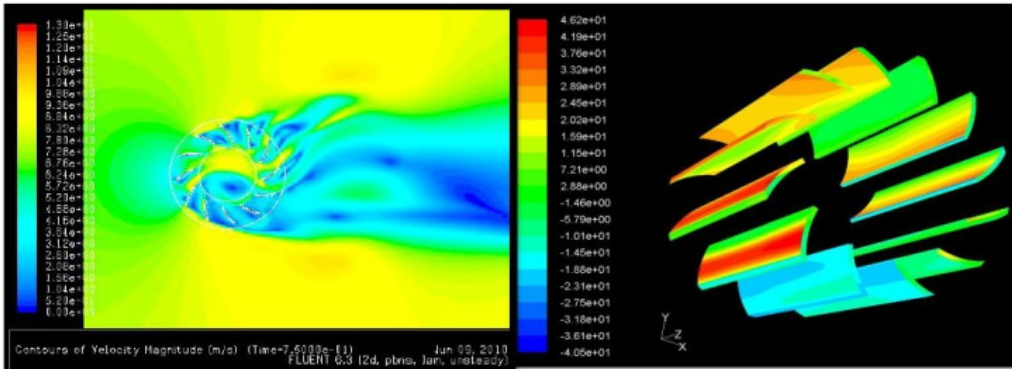
- Wind velocity: 6.5m/s
- Angular velocity : 25.1rad/s

Experimental device and performance testing
 <Flow analysis using Fluent>

<Flow analysis using Fluent>

Velocity distribution

Pressure distribution



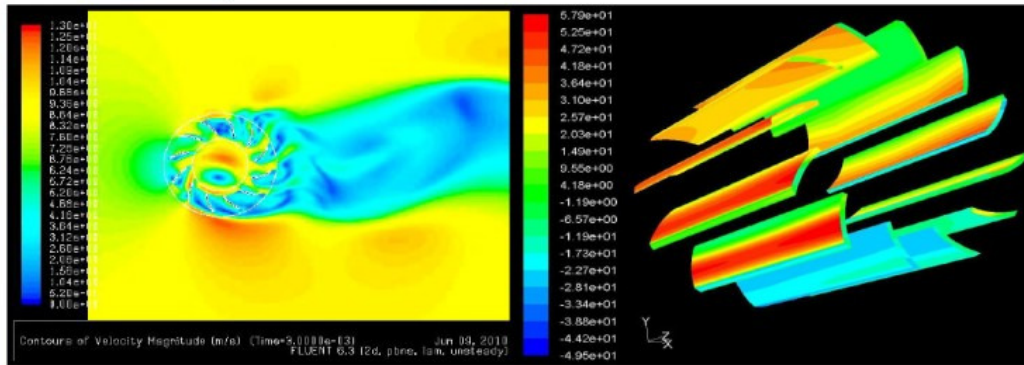
- Wind velocity: 7.5m/s
- Angular velocity : 27.7rad/s

Experimental device and performance testing
 <Flow analysis using Fluent>

<Flow analysis using Fluent>

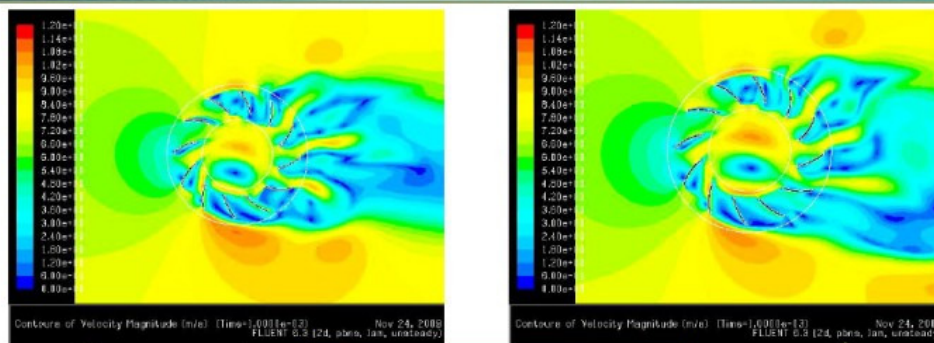
Velocity distribution

Pressure distribution



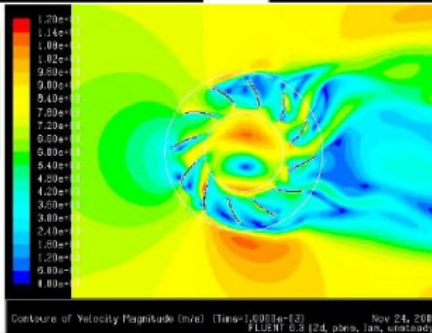
- Wind velocity: 8.5m/s
- Angular velocity : 30.9rad/s

Experimental device and performance testing
 <Flow analysis using Fluent>



- Wind velocity : 7.5m/s
- Angular velocity : 18.2rad/s

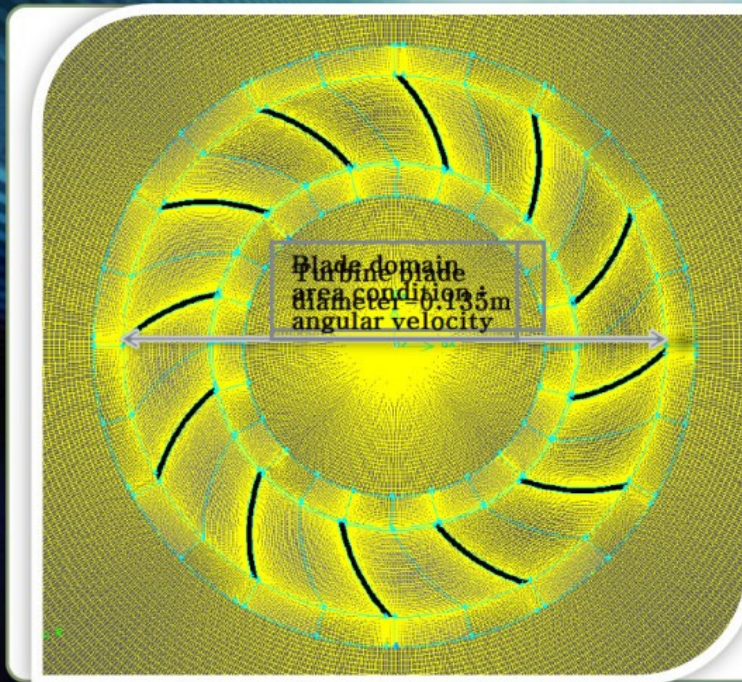
- Wind velocity : 7.5m/s
- Angular velocity : 27.7rad/s



- Wind velocity : 7.5m/s
- Angular velocity : 39.1rad/s

Experimental device and performance testing

<Flow analysis using Fluent>



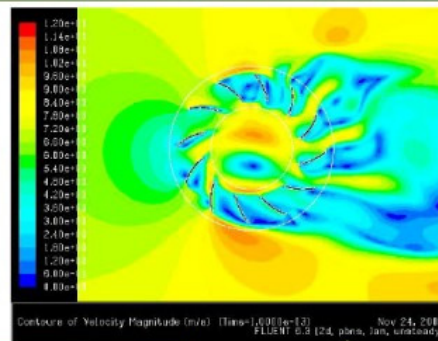
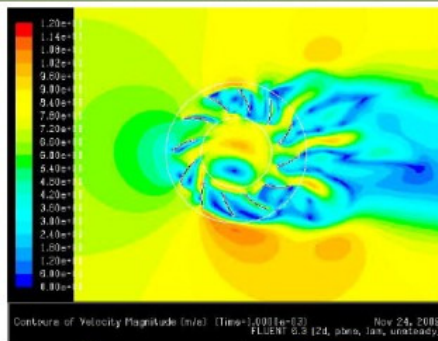
- Grid = number of 160,000
- Inlet condition : velocity (6.5m/s, 7.5m/s, 8.5m/s)

Outlet condition: Atmospheric



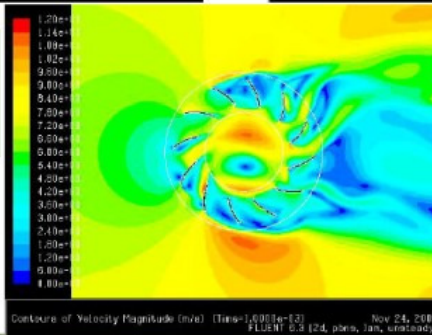
Experimental device and performance testing

<Flow analysis using Fluent>



- Wind velocity : 7.5m/s
- Angular velocity : 18.2rad/s

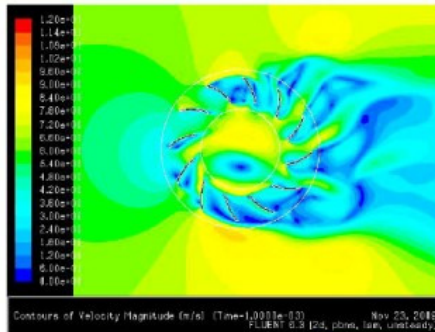
- Wind velocity : 7.5m/s
- Angular velocity : 27.7rad/s



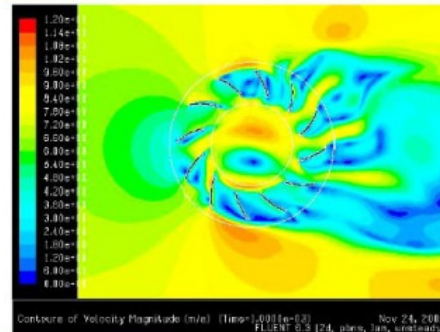
- Wind velocity : 7.5m/s
- Angular velocity : 39.1rad/s

Experimental device and performance testing

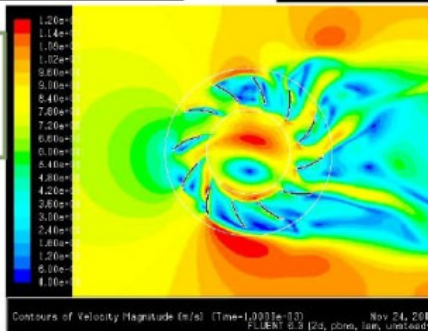
<Flow analysis using Fluent>



•Wind velocity :
6.5m/s
•Angular velocity :
25.1rad/s



•Wind velocity :
7.5m/s
•Angular velocity :
27.7rad/s



•Wind velocity :
8.5m/s
•Angular velocity :
30.9rad/s



Changwon National University

Computational Fluid Engineering Lab.

Conclusion

We built and tested the wind turbines. As a result, we found the possibility of generation by using driving wind.

In each of the wind speed, there are predetermined the number of rotation can get best power depending on the load torque.

In the faster than 7.5m/s wind speed, except for 6.5m/s, wingtip velocity ratio was observed nearly 0.26. Under this wingtip velocity ratio, a dynamometer was 0.08.

This result indicates that in over 7.5m/s wind speed efficiency maintain certainly 8% and go down when wind speed go down.



Changwon National University

Computational Fluid Engineering Lab.



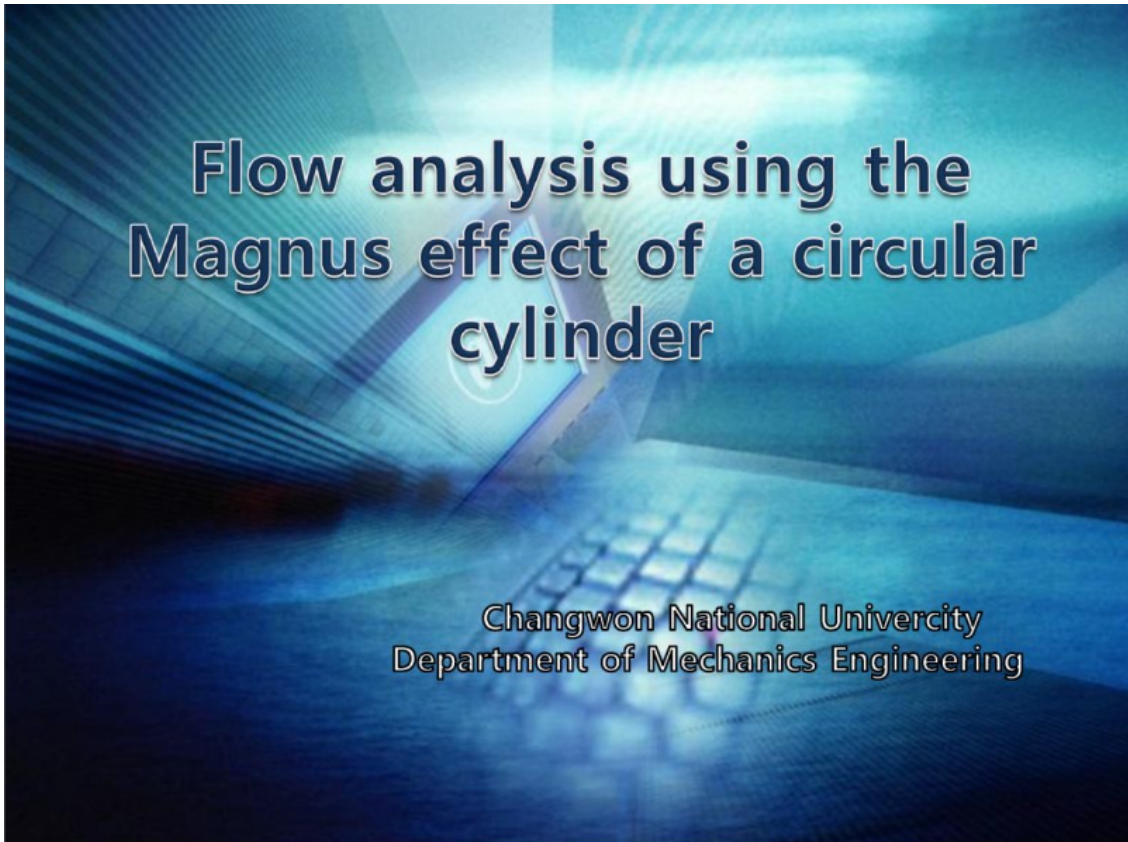


Table of Contents

원형실린더를 이용한
Magnus 효과 추진장치의
유동해석

- I Background and Purpose
- II Theoretical background
- III Numerical analysis and experimental results
 - 1 Flow Visualization and wind tunnel experiments
 - 2 Flow analysis
 - 3 DATA analysis and comparison
- III Conclusion

Changwon National University Computational Fluid Engineering Lab.

The Table of Contents slide has a light green and white background. It lists the main sections of the presentation, with the third section, 'Numerical analysis and experimental results', further divided into three sub-sections. The text is presented in a clean, sans-serif font.

Background and purpose

Magnus Effect

- Amplified interest in developing alternative energy power sources due to a spike in oil prices, Depletion of fossil fuels, Environmental pollution
- Increased interest in the flettner rotor sailboat with Magnus Effect
- The need for research on the effects of magnus effect
- Understanding the basics of Fluid Mechanics, and the use of a commercial analysis program



<Flettner rotor sailboat>



<Spinning Wings>

Based on the Bernoulli Equation circular cylinder flow analysis magnus effect

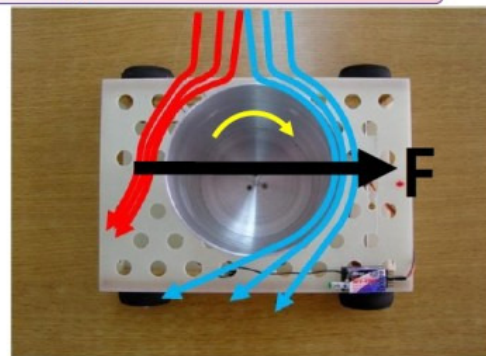



Theoretical background


Bernoulli Theory

$$\frac{P}{\rho g} + \frac{1}{2g} v^2 + z = \text{constant}$$

- Depending on the speed difference of the air flow , pressure has the relative differences.
- Force occurs from high pressure to low pressure



On the same side as the direction of rotation of the air flow is accelerated
 Decrease in pressure

On the opposite side as the direction of rotation of the air flow is decelerated
 Increase in pressure

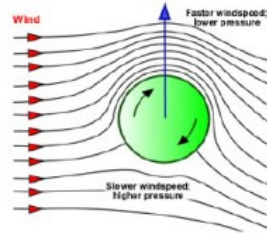


Theoretical background

Kutta-Joukowski theory of lift

$$L = -\frac{1}{2} \rho U_{\infty}^2 \frac{4K}{aU_{\infty}} ba \int_0^{2\pi} \sin^2 \theta d\theta = -\rho U_{\infty} (2\pi K) b$$

$$\frac{L}{b} = -\rho U_{\infty} \Gamma$$



Theory data

lift, drag coefficient by MTGresh's rotating cylinder experiments

$$F = [L^2 + D^2]^{1/2}$$

$$L, D = C_{L,D} \frac{1}{2} \rho U_{\infty}^2 2ba$$

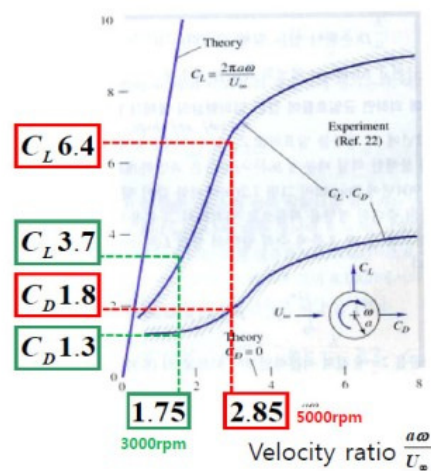
C_L : Lift coefficient

C_D : Drag coefficient

ρ : Density

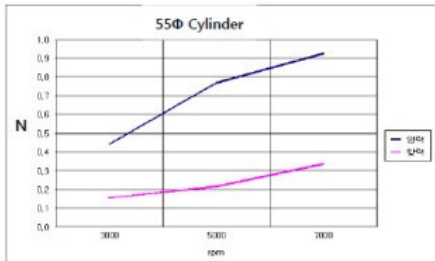
U : A wind tunnel speed

$2ba$: Projection area



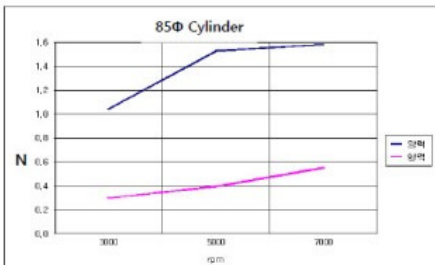
Theory data

Calculated lift and drag (gresh's experimental)



55Φ Cylinder

rpm	3000	5000	7000
Lift-Drag coefficient	3.7, 1.3	6.4, 1.8	7.7, 2.8
Lift force	0.4456N	0.7708N	0.9273N
Drag force	0.1566N	0.2168N	0.3372N



85Φ Cylinder

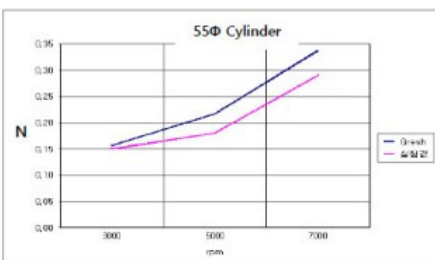
rpm	3000	5000	7000
Lift-Drag coefficient	6.6, 1.6	8.2, 3.2	8.5, 3.5
Lift force	1.0427N	1.5268N	1.6827N
Drag force	0.2980N	0.5958N	0.6517N

$$U_{\infty} = 5m/s$$



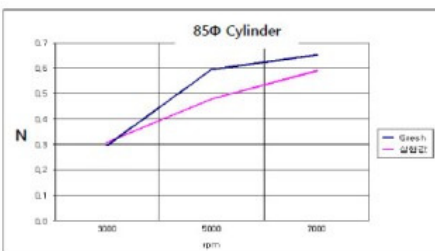
Theory data

Comparison of gresh's value and experimental value



55Φ Cylinder

rpm	3000	5000	7000
Gresh	0.1566N	0.2168N	0.3372N
Experimental value	0.15N	0.18N	0.29N



85Φ Cylinder

rpm	3000	5000	7000
Gresh	0.2980N	0.5958N	0.6517N
Experimental value	0.31N	0.48N	0.59N

$$U_{\infty} = 5m/s$$



Flow Visualization and Wind Tunnel Test

원형실린더를 이용한
Magnus 효과 추진장치의
유동해석

Production flow visualization device



<Smoke devices>



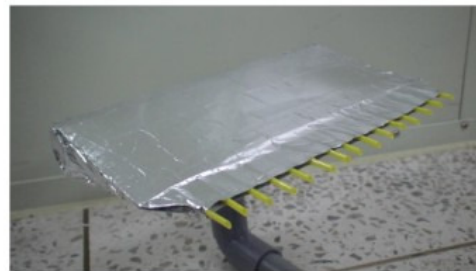
< Plumbing >



<Smoke injection system>



<A wind tunnel>



<Smoke injection system>



Changwon National University

Computational Fluid Engineering Lab.

Flow Visualization and Wind Tunnel Test

원형실린더를 이용한
Magnus 효과 추진장치의
유동해석

No rotation



Cylinder diameter = 55φ

$$\frac{\Omega R}{U} = 0$$

$$U = 5\text{m/s}$$



Changwon National University

Computational Fluid Engineering Lab.

Flow Visualization and Wind Tunnel Test

원형실린더를 이용한
Magnus 효과 추진장치의
유동해석

No rotation



Cylinder diameter = 85φ

$$\frac{\Omega R}{U} = 0$$

$$U = 5\text{m/s}$$

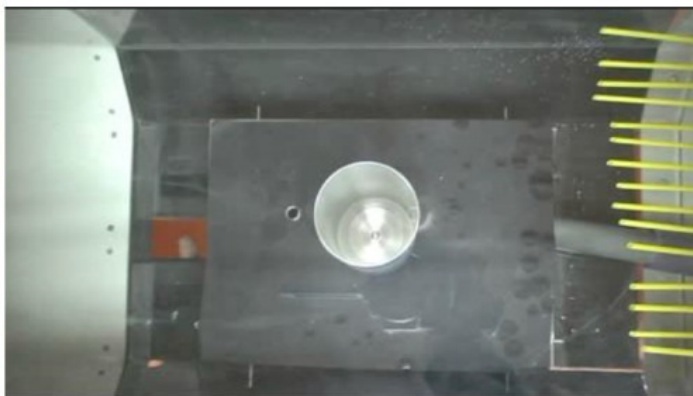


Changwon National University

Computational Fluid Engineering Lab.

Flow Visualization and Wind Tunnel Test

원형실린더를 이용한
Magnus 효과 추진장치의
유동해석



Cylinder diameter = 55φ

$$\frac{\Omega R}{U} = 4$$

$$U = 5\text{m/s}$$

Direction of rotation = CW

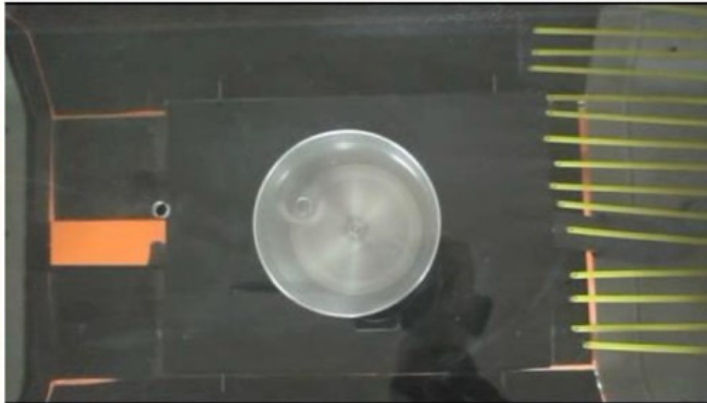


Changwon National University

Computational Fluid Engineering Lab.

Flow Visualization and Wind Tunnel Test

원형실린더를 이용한
Magnus 효과 추진장치의
유동해석



Cylinder diameter = 85φ

$$\frac{\Omega R}{U} = 4$$

U = 5m/s

Direction of rotation = CW



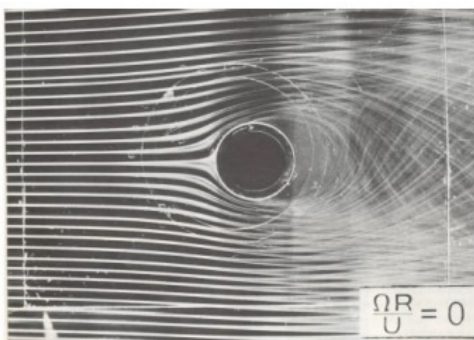
Changwon National University

Computational Fluid Engineering Lab.

Flow Visualization and Wind Tunnel Test

원형실린더를 이용한
Magnus 효과 추진장치의
유동해석

Comparison with experimental streamline



$$\frac{\Omega R}{U} = 0$$

U = 5m/s



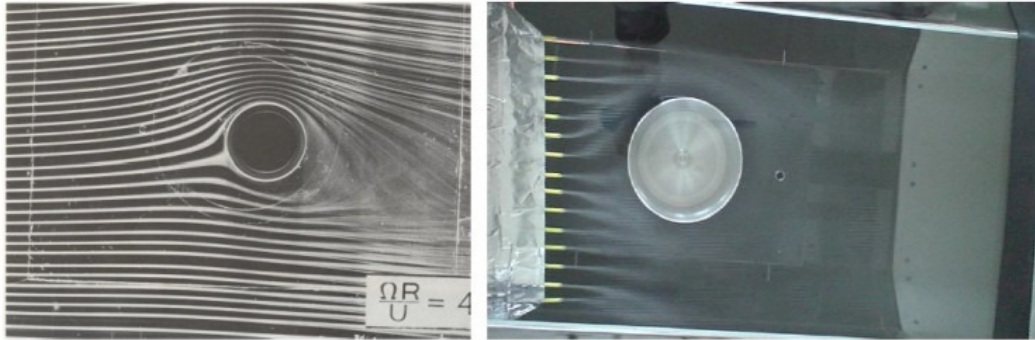
Changwon National University

Computational Fluid Engineering Lab.

Flow Visualization and Wind Tunnel Test

원형실린더를 이용한
Magnus 효과 추진장치의
유동해석

Comparison with experimental streamline



$$\frac{\Omega R}{U} = 4$$

U = 5m/s

Direction of rotation = CW

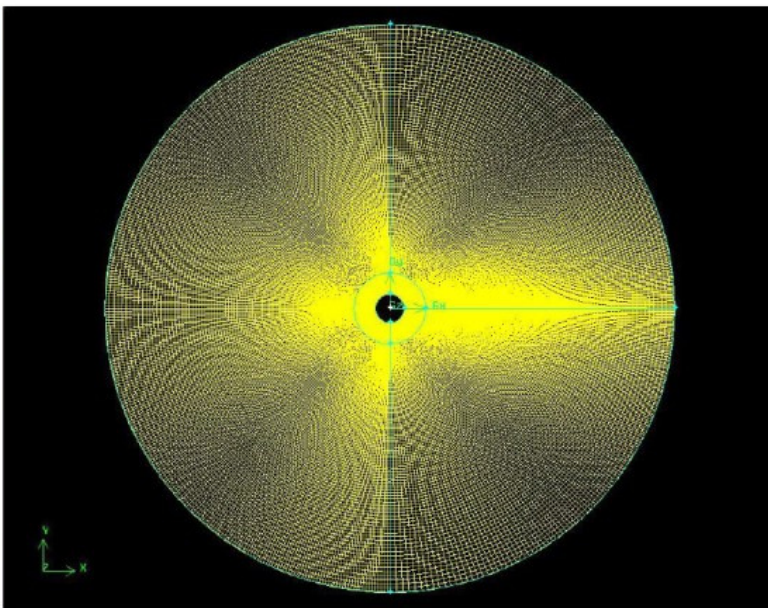


Changwon National University

Computational Fluid Engineering Lab.

Numerical analysis and experimental results

원형실린더를 이용한
Magnus 효과 추진장치의
유동해석



Fluid Field : D=2.75m

Wall : 55mm

Grid : 60,000

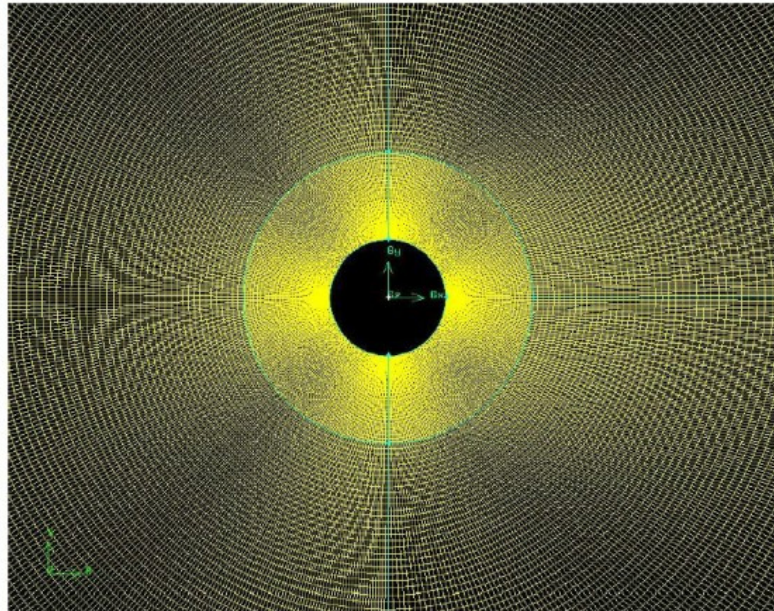


Changwon National University

Computational Fluid Engineering Lab.

Numerical analysis and experimental results

원형실린더를 이용한
Magnus 효과 추진장치의
동해석

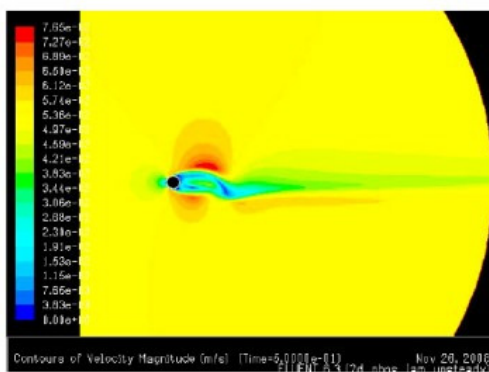


Fluid Field : $D=2.75m$
Wall : 55mm
Grid : 60,000

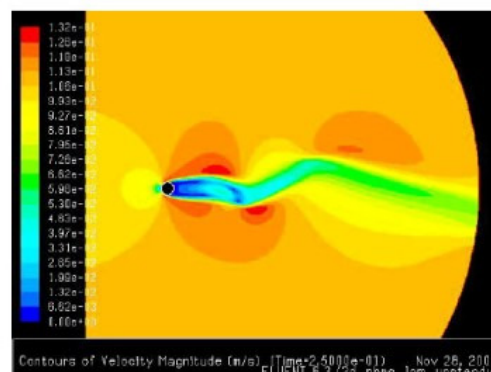
Numerical analysis and experimental results

원형실린더를 이용한
Magnus 효과 추진장치의
동해석

If there is no rotation of the flow



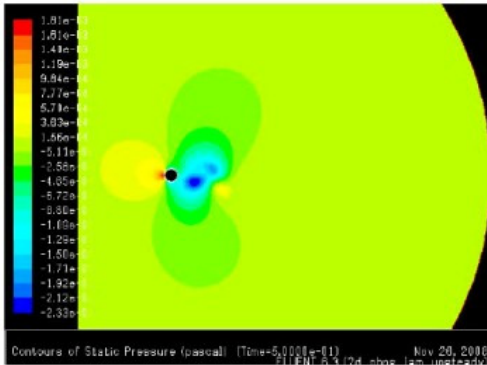
Re=200 velocity



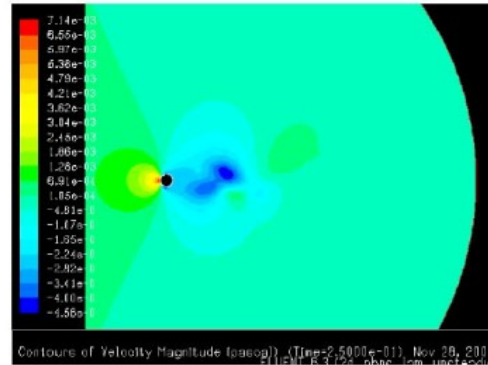
Re=400 velocity

Numerical analysis and experimental results

If there is no rotation of the flow



Re=200 pressure

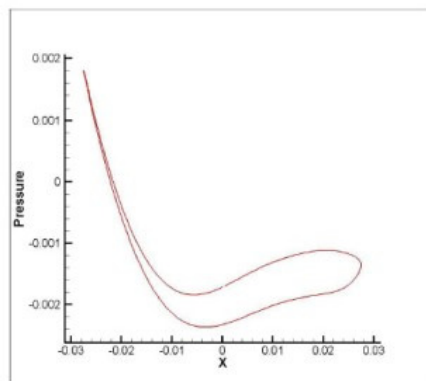


Re=400 pressure

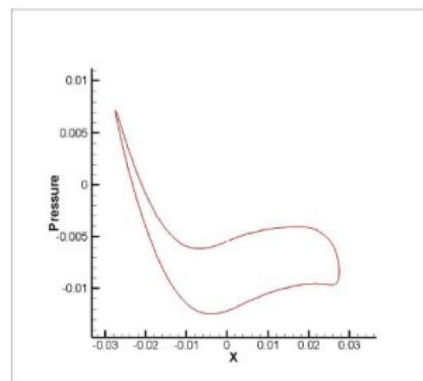


Numerical analysis and experimental results

If there is no rotation of the flow



Re=200 Pressure Distribution



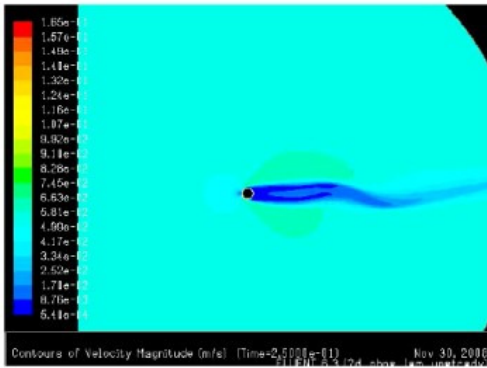
Re=400 Pressure Distribution



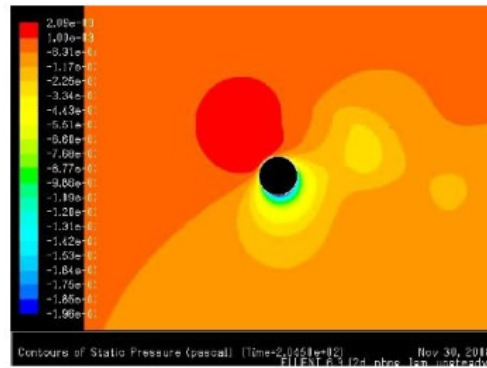
Numerical analysis and experimental results

원형실린더를 이용한
Magnus 효과 추진장치의
동해석

If the rotation of the flow



Re=200 6rad/s velocity

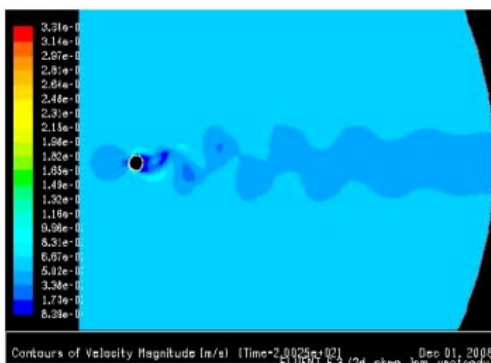


Re=200 6rad/s pressure

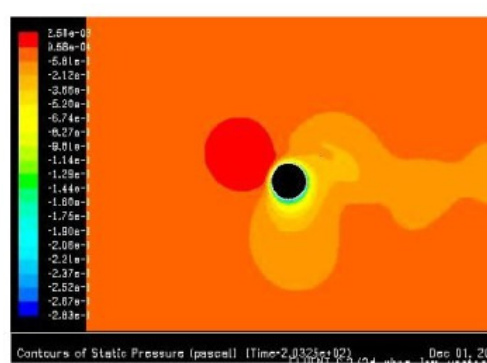
Numerical analysis and experimental results

원형실린더를 이용한
Magnus 효과 추진장치의
동해석

If the rotation of the flow



Re=200 12rad/s velocity

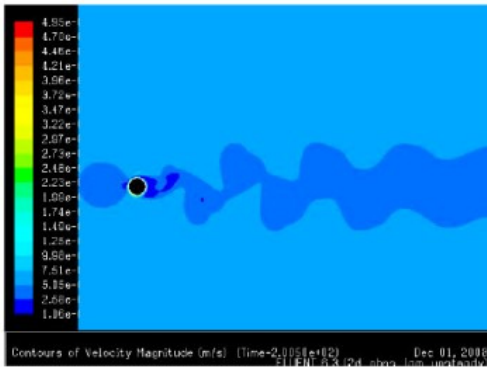


Re=200 12rad/s pressure

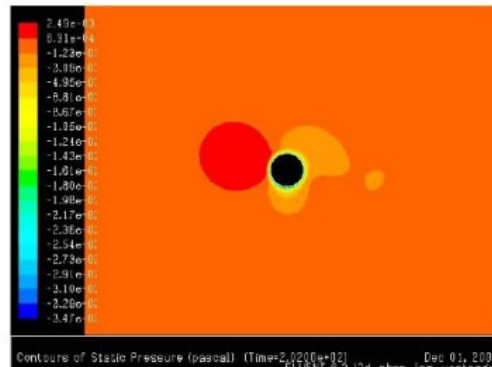
Numerical analysis and experimental results

원형실린더를 이용한
Magnus 효과 추진장치의
동해석

If the rotation of the flow



Re=200 18rad/s velocity

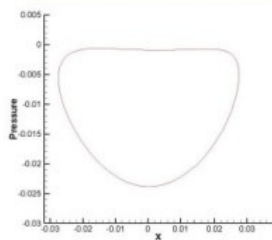


Re=200 18rad/s pressure

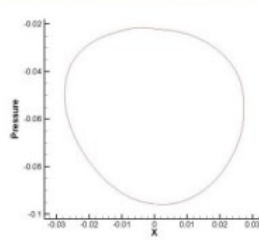
Numerical analysis and experimental results

원형실린더를 이용한
Magnus 효과 추진장치의
동해석

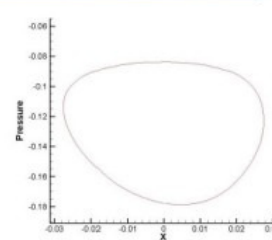
changes in base according to the difference in pressure and rotation speed



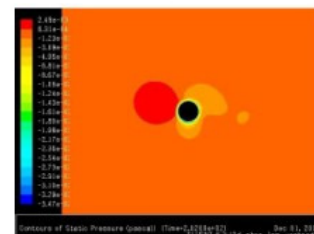
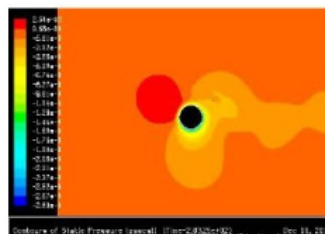
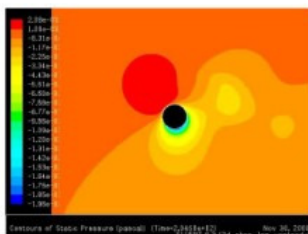
6rad/s pressure



12rad/s pressure



18rad/s pressure



Direction of rotation : CCW

Conclusion

Reynolds number for the same cylinder shape with the higher pressure caused by enlarged showed that an increase in lift. In addition, according to a circular cylinder lift rpm change the size of the higher rotational speed increased.

Smoke on the device design and fabrication, obtained through experiments and numerical knowledge of the Magnus effect has emerged in the future is the basis of zero-emission propulsion system design.

An infinite source of energy by using natural wind to be able to get a lift in the future as renewable energy were not favorably.



Thank you.

8. Acknowledgment

The Short Term-Stay International Exchange Program between Japan and Korea was promoted and financially supported by Japan Student Services Organization (JSSO). We thank JSSO for its help in the financial support.

All of Japanese and Korean students greatly appreciate the chance to participate this program created by Prof. Saito and Prof. Shin.

We also thank Mr. Hiragi (Director of Shizuoka University Motors) for leading us a tour to Shizuoka University Motors's factory. We also thank Mr. Noba (Fukuta Laboratory, Shizuoka University), Mr. Matsushita and Mr. Tanaka (Sanada Laboratory, Shizuoka University) for taking part in the program.